UNIVERSITY OF TROMSØ UIT

FACULTY OF SCIENCE AND TECHNOLOGY
DEPARTMENT OF PHYSICS AND TECHNOLOGY

Synthetic aperture ultrasound imaging with application to interior pipe inspection

Martin Hansen Skjelvareid

A dissertation for the degree of
Philosophiae Doctor

September 2012

The first principle is that you must not fool yourself
— and you are the easiest person to fool.

— *Richard P. Feynman*

Abstract

This thesis is concerned with synthetic aperture focusing of ultrasonic pulse-echo measurements, with application to multilayered media and cylindrical structures. The work is motivated by the need for accurate methods for non-destructive testing of pipelines, particularly water distribution pipelines. By improving the lateral resolution in ultrasonic measurements, the synthetic aperture algorithms presented in the thesis enable accurate detection and sizing of corrosion damage, holes, and other pipe defects.

In ultrasonic inspection of water-filled pipelines, the water and the pipe wall constitute a multilayered structure, and multilayer synthetic aperture algorithms are therefore needed. We present a number of such multilayer algorithms, formulated in both the time and Fourier domains, and show that the Fourier-domain algorithms generally require a significantly lower processing time. An algorithm combining two algorithms used in reflection seismology is shown to require the least processing time for large data sets.

When the synthetic aperture is created by scanning over a straight line or a flat plane, and the propagating medium is homogeneous, the lateral resolution after focusing is approximately half the transducer diameter. We show that this resolution limit also applies in the multilayer case, for both two- and three-dimensional imaging, as long as the transducer beam is relatively narrow.

Ultrasonic measurements for pipe inspection are usually performed over a cylindrical surface. We develop a new synthetic aperture algorithm, termed cylindrical phase shift migration, to focus such scans. The algorithm is applicable to concentrically layered media, and thus enables full volumetric synthetic aperture imaging in pipes and similar structures. It is shown that the lateral resolution along the cylinder axis is approximately half the transducer diameter, and that the angular resolution is approximately $D/(2R)$, where D denotes transducer diameter and R denotes scan radius. The algorithm is also adapted for use with focused transducers, and it is shown that it significantly extends the range within which the transducer yields a high lateral resolution.

Acknowledgments

First and foremost I would like to give my sincere thanks to my advisors: To Yngve Birkelund for teaching me what research is all about, and for answering my questions and e-mails on short notice and at odd times of day; and to Yngvar Larsen for sharing his vast knowledge of synthetic aperture focusing with me, and for his intuitive understanding of those pesky algorithm details.

I am also very grateful to Breivoll Inspection Technologies and the Research Council of Norway, who have financed my Ph.D. project. Simultaneously working towards a Ph.D. and working in a commercial company has not always been easy, but it has given me a valuable lesson on application of research in the "real world", and a sense that what I do can actually make a difference. Special thanks go to Hans Eilif Larsen, who was my advisor at Breivoll for the first three years of the project, and to Lars Brenna, who has given several valuable comments on my manuscripts.

During my work on the Ph.D. project, I spent half a year working at the Signals and Systems group at Uppsala University. My stay there was the starting point for much of the work presented in this thesis, and I am very grateful to Tadeusz Stepinski for inviting me. In Uppsala I also started my collaboration with Tomas Olofsson, who has been an important contributor to my work, and whose dry humor and down-to-earth attitude I truly appreciate. I am also very grateful to all the other Ph.D. students at the Signals and Systems group, who made me feel welcome right away (despite my strange Norwegian language), and whose friendship I hope to keep for many years to come.

A very special thanks goes to Rasmus Ernstsen Prytz, who works at the workshop run by the Department of Physics and Technology in Tromsø. He has helped me immensely with making and modifying experimental equipment – especially the cylindrical scanner. Without his help this thesis would contain nothing but simulations.

I would also like to thank my friends and family, who have helped me remember that there are more important sides to life than work. Thanks for all the good times we spent hiking, skiing, climbing, and even wood chopping – I hope there'll be time for more of that when this is all over. And finally, to my beloved wife Jorunn, whose smiles, encouragements, and endless patience have kept me going through it all: Thank you.

Martin Hansen Skjelvareid
Tromsø, July 2012

Contents

Nomenclature

Coordinate systems

This thesis uses both Cartesian and cylindrical coordinate systems. The three perpendicular axes in the Cartesian coordinate system are labeled x, y and z, and in two-dimensional geometries, only x and z are used. In the cylindrical coordinate system, the cylinder axis is labeled z, and the length and angle of the polar axis is labeled r and ϕ, respectively.

Symbols

c	Wave velocity
$\hat{c}$	Effective wave velocity for exploding reflector model, $\hat{c} = c/2$
c_{rms}	Root-mean-square wave velocity, taken with respect to τ
D	Transducer diameter
D_{vs}	Effective diameter for virtual source
d_l	Thickness of layer l
Δn	Angular wavenumber bandwidth
$\delta\phi$	Resolution along ϕ axis
$\delta\phi_s$	Sampling interval along ϕ axis
δs	Arc length resolution in cylindrical scan, equal to $\delta\phi \cdot r$
Δt	Temporal pulse length
$\Delta\theta$	Transducer beam width
Δx	Beam width along x axis
δx	Resolution along x axis
δx_s	Sampling interval along x axis
δy	Resolution along y axis
Δz	Distance from layer interface to image point
δz	Resolution along z axis
δz_s	Sampling interval along z axis
F	Transducer focal length
f	Frequency
f_c	Transducer center frequency

f_{min}	Lower cut-off frequency of transducer passband
f_{max}	Upper cut-off frequency of transducer passband
f_s	Sampling frequency
G	Extrapolation transfer function in cylindrical coordinates
i	Imaginary unit
i_p	Focused image
γ	Angle relative to transducer normal in cylindrical scan
ω	Angular frequency, $2\pi f$
k	Wavenumber, equal to ω/c
k_x	Wavenumber along x axis
k_y	Wavenumber along y axis
k_z	Wavenumber along z axis
k_r	Wavenumber in radial direction
L	Number of layers in multilayer geometry
λ	Wavelength
M	Number of measurement positions
N	Number of samples along the time or depth axis
n	Order for Bessel and Hankel functions. Corresponds to angular wavenumber.
Q	Volume velocity of acoustic source
R	Scanning radius in cylindrical scan
R_l	Inner radius of layer l (for concentrical layers)
R_{vs}	Effective scanning radius for virtual source
ρ	Density
t	Time
t_{rms}	Approximate time-of-flight in a multilayer geometry, based on RMS wave velocity
τ	Normal incidence travel time
u_0	Amplitude of normal velocity for oscillating acoustic source
$\hat{x}$	Normalized x coordinate used in apodization functions.
Z	z position of transducer measurement surface
Z_l	z position for interface on top of layer l

Functions

$\alpha(\cdot)$	Apodization weight
$J_n(\cdot)$	Bessel function of the first kind, of order n
$\mathrm{jinc}(\cdot)$	Directivity function for circular transducers. $\mathrm{jinc}(x) = 2J_1(x)/x$
$H_n^{(1,2)}(\cdot)$	Hankel function of the first or second kind, of order n
$\mathrm{sgn}(\cdot)$	Sign function

Notation

- The general sound pressure wave field is indicated with a lowercase p, for example $p(t, x, z)$. A Fourier transformation along one or multiple coordinates is denoted with the $\mathcal{F}\{\cdot\}$ operator, and inverse Fourier transformation is denoted $\mathcal{F}^{-1}\{\cdot\}$. The Fourier-domain wave field is denoted with an uppercase P. An example:

$$P(\omega, k_x, z) = \mathcal{F}_{t,x}\{p(t, x, z)\}$$
$$p(t, x, z) = \mathcal{F}_{t,x}^{-1}\{P(\omega, k_x, z)\}$$

- Transducer coordinates are marked with a prime. For example, in a Cartesian coordinate system with coordinates (x, y, z), the transducer position is denoted (x', y', z').
- The asymptotic computational complexity of an algorithm is described with “big O” notation, $O(\cdot)$.

Acronyms

BIT	Breivoll Inspection Technologies
CPSM	Cylindrical Phase Shift Migration
DAS	Delay-And-Sum
FFT	Fast Fourier Transform
FWHM	Full Width at Half Maximum
MLDAS	Multi-Layer Delay-And-Sum
MULOK	MUlti-Layer Omega-K
NDT	Non-Destructive Testing
PSF	Point Spread Function
PSM	Phase Shift Migration
RFEC	Remote Field Eddy Current
RMS	Root-Mean-Square
SAFT	Synthetic Aperture Focusing Technique
SNR	Signal-to-Noise Ratio
ZNCC	Zero-mean Normalized Cross-Correlation

Chapter 1

Introduction

As the Earth's population grows and the global climate is changing, it is becoming ever more important to sustainably manage the fresh water resources. However, many of the water distribution networks in use today are very old, and large quantities of water are lost due to leakages and unexpected breaks. For example, in Norway 25 % of the water distribution network was installed before 1970, and an estimated 31% of the water is lost on its way to the consumer [Statistics Norway, 2010]. Throughout Europe, the amount of water loss varies greatly, from 6-7 % in some countries and up to 40 % in others [EEA, 2009].

Replacing old pipelines is complicated and expensive, and the rate of renewal is therefore relatively low. In Norway, the average yearly rate of renewal in 2008-2011 was 0.71 % [Statistics Norway, 2010]. With limited resources, it is important to monitor the condition of the pipelines, so that necessary repairs can be made without prematurely replacing pipes with a long remaining lifetime.

The Norwegian company Breivoll Inspection Technologies (BIT) performs inspection of water pipelines, supplying the water managers with information on remaining pipe wall thickness, corrosion, and a number of other pipeline features [Kloosterman, 2009]. The inspection is based on ultrasonic measurements, performed with the robot shown in Fig. 1.1.

The research presented in this thesis is the result of a project initiated by BIT, the University of Tromsø, and the Northern Research Institute, called "Innovative use of synthetic aperture sonar for inspection of water distribution networks". Synthetic aperture focusing is a technique which can be applied in post-processing of acoustic and electromagnetic measurements, to increase the lateral resolution and signal-to-noise ratio [Cumming and Wong, 2004]. The main goal of the project is to investigate whether synthetic aperture focusing can be used to improve ultrasonic measurements of topography and wall thickness in pipes. The project was the first to receive support through the Norwegian Research Council's Industrial Ph.D. program [Norwegian Research

Figure 1.1: The inspection robot used by BIT to inspect water distribution networks. 64 ultrasound transducers are to measure the inside topography and the remaining wall thickness of the pipe. Photo: BIT

Council, 2012], which started in 2008.

1.1 Background and motivation

1.1.1 Pipe inspection

Pipe inspection has been an important topic in the field of non-destructive testing (NDT) for several decades [Kriesz, 1979; Roman and Pellegrino, 1993]. Traditionally, the focus has mainly been on pipes in nuclear power plants and oil and gas installations. However, technologies for inspection of other kinds of pipes are now emerging, including sewage pipes [Duran et al., 2002], pipes used in food processing [Lohr et al., 2003], and water pipes [Rajani and Kleiner, 2004].

One of the most widely used methods for pipe inspection is radiography, performed by illuminating the pipe with an x-ray or gamma-ray source on one side, and measuring transmission through the pipe wall by using a film on the opposite side [Raj et al., 2002]. However, due to the risk of exposure to radiation, and the inconvenience of using analog film, alternative methods like ultrasound are becoming increasingly popular [Carvalho et al., 2008]. Also, radiography cannot be used where only one side of the pipe is accessible, for example in inspection of buried pipes.

It is also common to perform inspections of pipelines from the inside using video cameras, often mounted on a remote controlled robot. However, for such inspections to be successful, the pipe must either be empty or filled with a transparent gas or liquid. The images produced by the camera also require careful interpretation by a human operator [Duran et al., 2002].

In ultrasonic inspection of pipelines, one or multiple ultrasonic transducers are used to generate a short ultrasonic pulse and record the reflected echoes from the pipe wall. The time-of-flight for reflections from the inside and outside of the pipe wall are used to estimate the inside topography and pipe wall thickness. Ultrasonic inspection usually requires that the pipe wall is relatively clean and free of corrosion products for the ultrasonic pulse to enter the pipe wall [Rajani and Kleiner, 2004]. Note, however, that the pipe wall thickness can also be estimated from the resonance generated by multiple reflections inside the pipe wall. This approach, which is used in the BIT inspection robot, can be performed using lower transducer frequencies than traditional pulse-echo testing, and is therefore less sensitive to non-ideal surface conditions [Kloosterman, 2009]. Ultrasound is also employed in testing of pipes using *guided waves*, where an external transducer array is used to generate waves which travel along the pipe. Corrosion and other defects can be detected through the reflection of these waves [Lowe et al., 1998]. However, the technique requires access to the pipe from the outside, and the inspection range for pipes buried in soil is limited to 20 meters or less [Demma et al., 2005].

Other common inspection technologies are based on measurements of electromagnetic fields. One technique, called *magnetic flux leakage*, detects corrosion pits and other defects by magnetizing the pipe wall and measuring where the magnetic field leaks out of the wall. Another, called *remote field eddy current* (RFEC), measures the pipe wall thickness through the attenuation and phase shift of a low-frequency electromagnetic signal [Rajani and Kleiner, 2004].

In many cases, manual inspection of the pipeline is not practical, or even possible, and the inspection is automated by using a robot traveling through the pipe. In the petroleum industry, pipes are often inspected using so-called *pigs*, which are pushed through the pipe by the oil or gas itself [Okamoto Jr. et al., 1999; Reber et al., 2002]. In other cases, for example in sewer inspection, the sensors are mounted on a platform with its own means of propulsion [Duran et al., 2002].

Traditionally, automated in-pipeline inspections have not been performed for water pipelines. Leakages in the pipes have been detected using alternative methods, often involving listening devices for detection of leakage noise [Fuchs and Reihle, 1991; Hunaidi, 2012]. However, such devices can not be used to determine the structural condition of the pipes. The lack of commercially available methods for water pipe inspection may be due to some of the particular challenges posed by water pipes. The pipes are often covered with corrosion products, which in oil and gas pipes are removed regularly using cleaning pigs. However, water pipeline managers are reluctant to clean the pipes, since it increases the internal corrosion rate and releases corrosion products into the drinking water [Rajani and Kleiner, 2004]. Without cleaning, technologies like magnetic flux leakage are often not effective, since they require direct contact with the pipe wall. Ultrasonic and RFEC methods do not require close contact with the pipe wall, and therefore do not have the same strict cleaning requirements [Rajani and Kleiner, 2004]. Most water pipelines also have not been designed to facilitate inspection, and inspection units therefore have to be inserted via alternative entry points, e.g. fire hydrants, or by installing a dedicated entry point on the pipeline [Koutsakos et al., 1997; Kloosterman, 2009].

There are advantages and disadvantages to all available pipe inspection technologies, and multiple technologies are often combined on a single inspection unit [Eiswirth et al., 2000; Beuker et al., 2009]. In this thesis we focus on improving ultrasonic methods for pipe inspection.

1.1.2 Synthetic aperture focusing

The synthetic aperture concept is based on performing measurements of a region of interest, in several different positions, and combining the measurements in post-processing to synthesize a large effective aperture. An illustration of the concept is shown in Fig. 1.2. In an unprocessed data set, the lateral resolution decreases as the distance to the sensor increases, due to the divergence of the sensor beam. Synthetic aperture processing yields a much narrower beam and thus a higher lateral resolution, giving rise to the term synthetic aperture *focusing*.

Synthetic aperture focusing is often used in active imaging systems like radar [Tomiyasu, 1978; Cumming and Wong, 2004] and sonar [Hayes and Gough, 2004; Hansen, 2011], in which an antenna or a transducer first emits a wave and then records the backscattered echoes. With synthetic aperture focusing, radar satellites in orbit hundreds of kilometers above Earth can yield images with a lateral resolution on the scale of meters [Cumming and Wong, 2004]. The concept can also be applied in passive systems like radio interferometers, where the Earth's rotation is used to synthesize apertures thousands of kilometers long [Levanda and Leshem, 2010].

Building on previous work within sonar and radar imaging, synthetic aperture focusing was introduced to the field of ultrasonics in the 1970s, and became known as the Synthetic Aperture Focusing Technique (SAFT) [Doctor et al., 1986]. Initially, SAFT was mainly used for non-destructive testing of metal parts [Kino et al., 1980; Doctor et al., 1986; Müller et al., 1991], but variations of the technique have also been introduced for medical imaging [Karaman et al., 1995; Frazier and O'Brien Jr., 1998; Jensen et al., 2006]. There is also a growing interest in similar algorithms for non-destructive testing with

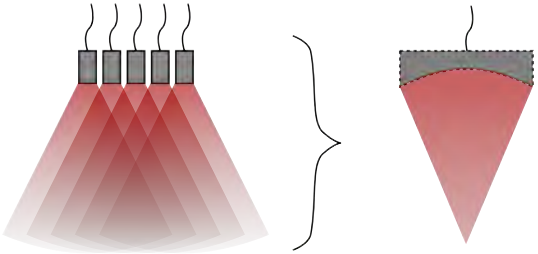

Figure 1.2: Illustration of the synthetic aperture focusing concept. Several overlapping measurements of the same point in space are combined to yield a large synthetic aperture with a narrow beam, yielding high lateral resolution.

ultrasonic transducer arrays [Holmes et al., 2005; Pörtzgen et al., 2007; Hunter et al., 2008].

Synthetic aperture focusing is essentially a correlation of the recorded data with the expected response from each point in the image. The correlation can be performed both in the time domain, using so-called delay-and-sum beamforming, or in the Fourier domain. Fourier domain algorithms generally have a lower computational complexity [Nagai, 1985; Haun et al., 2002], and the Fast Fourier Transform (FFT) algorithm also enables efficient conversion of data between the two domains.

In a routine pipe inspection, BIT collects data from hundreds of meters of pipe in one day. For SAFT to be applied to data sets of this scale, it is crucial that the implementation is efficient, and this has been a priority in the work on this thesis.

1.1.3 Multilayer imaging

Most SAFT algorithms are based on the assumption that the propagating medium is homogeneous, with a constant wave velocity. However, for the main application considered in this thesis, water pipe inspection, the ultrasonic wave propagates through both water and the pipe wall material. Some pipes are also lined with additional corrosion-resistant layers like epoxy or cement mortar. In general, the wave velocity of each layer is different, and this has to be taken into account in the SAFT algorithm. Multilayer SAFT imaging is therefore one of the main research topics in this thesis.

Another important example of multilayer imaging is that of immersion scans, in which an object is immersed in water, and imaging is performed by scanning the transducer in the water layer above the object. The main advantages of immersion scans, as opposed to contact scans, are that the water layer acts as a good and uniform couplant for the acoustic waves, and that there is no friction causing transducer wear. Immersion scans are routinely used for inspection of parts in industry [ASNT, 2007]. An example of immersion scanning is shown in Fig. 1.3.

The crust of the Earth consists of distinct layers, and thus the problem of imaging in multilayered media is well known within the field of seismic exploration. Synthetic aperture algorithms are also employed for processing of seismic data, although in this field they are termed *migration* algorithms. In this thesis we implement a number of such migration algorithms for ultrasonic imaging in multilayered media.

1.1.4 Imaging with cylindrical apertures

In most applications of synthetic aperture ultrasound, the synthetic aperture is created by moving a transducer along a line or over a flat plane. However, for imaging in pipes and similar cylindrical structures, a cylindrical measurement surface is more suitable. In this thesis, we consider the measurement geometry

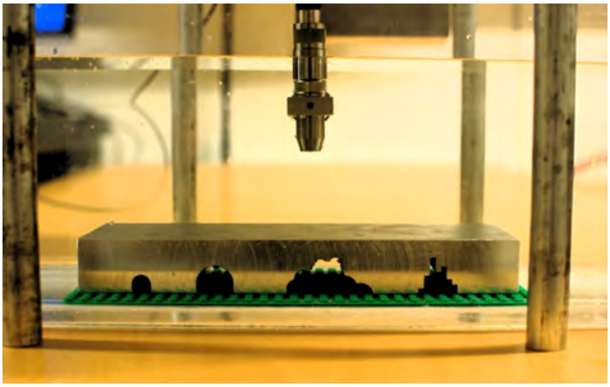

Figure 1.3: Example of immersion scanning. The photo is taken from an experiment on imaging of outside pitting, simulated by profiles machined out of an aluminium plate.

shown in Fig. 1.4(a), where pulse-echo measurements are performed with a transducer on a rotating arm. The arm is mounted on an inspection robot which moves through the pipe, creating a cylindrical measurement surface. Similar configurations have previously been applied for sewer and borehole inspection [Reber et al., 2002; Hayman et al., 1998]. Full angular coverage can also be achieved by using a transducer array [Fleury et al., 2006] or a fixed transducer with a rotating mirror [Birchall et al., 2007], but here we assume that the transducer itself is moved mechanically. Figure 1.4(b) illustrates the cylindrical coordinate system used in the pipe, where the transducer is moved over the surface given by a constant radius R. The resulting data set is three-dimensional, with axes of pulse-echo delay time t, angle ϕ, and distance along the pipe, z.

The distance from the transducer to the pipe surface is given by the pulse-echo delay time and the wave velocity of the liquid or gas in the pipe. Thus, a cylindrical scan yields a map of the interior topography of the pipe, which can be used to detect flaws like holes, pitting, and buildup of corrosion products [Duran et al., 2002]. The pulse can also penetrate the pipe wall and be reflected from the outer surface, enabling estimation of the pipe wall thickness [Reber et al., 2002; Birchall et al., 2007].

The setup in Fig. 1.4 is slightly different from BIT's scanner, shown in Fig. 1.1, which has a number of transducers in fixed angular positions. However, successful synthetic aperture processing requires that the aperture is sampled quite densely [Gough and Hawkins, 1997], and with the setup shown in Fig. 1.4(b), the spatial sampling intervals along both the ϕ and the z axis can be adjusted according to need.

As a research topic, cylindrical synthetic aperture imaging has received relatively little attention, although some contributions have been made [Haun et al., 2002; Andresen et al., 2011]. Development of a Fourier-domain synthetic

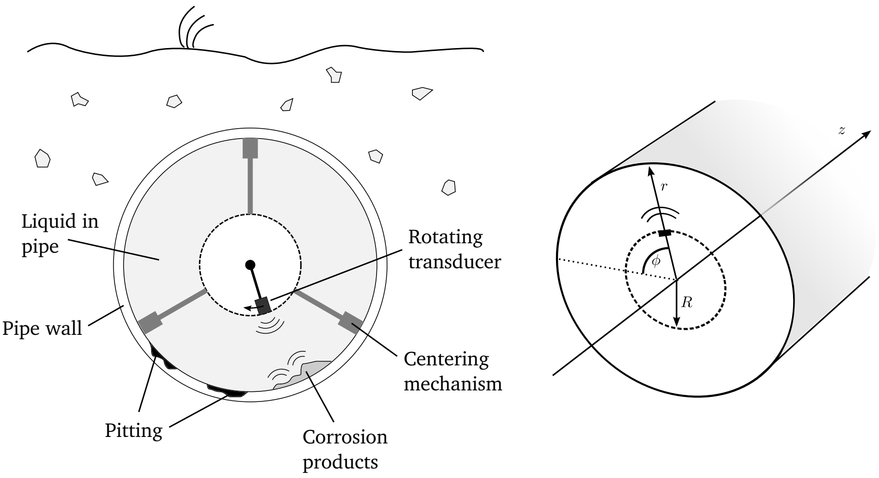

(a) (b)

Figure 1.4: Internal ultrasonic inspection of buried pipes. (a) A transducer is rotated inside the pipe, emitting pulses and receiving the backscattered echoes. Pitting and buildup of corrosion products can be detected through changes in the amplitude and delay time of the echoes. (b) Cylindrical coordinate system.

aperture algorithm for cylindrical apertures is therefore one of the main research topics in this thesis. A theoretical analysis of the attainable lateral resolution is given, and the effect of the angular sampling interval on grating lobes is also studied.

1.1.5 Imaging with focused transducers

Focused transducers are often employed in ultrasonic NDT applications due to their high lateral resolution and signal-to-noise ratio. Usually, such transducers are made using an acoustic lens which focuses the ultrasonic beam at a given distance from the transducer face, as shown in Fig. 1.5. Outside the focal zone, the ultrasonic beam is divergent, and the lateral resolution quickly decreases as the range to the target increases.

The pipe inspection geometry in Fig. 1.4 is well suited for a focused transducer, since the distance from the transducer to the pipe wall is constant and can be adjusted to fit the focal length. However, if the distance to the pipe changes, for example due to de-centering of the inspection robot or a change in the pipe diameter, the lateral resolution will decrease significantly. In this thesis, we show that by combining focused transducers with SAFT, a high lateral resolution can be obtained within a much wider range.

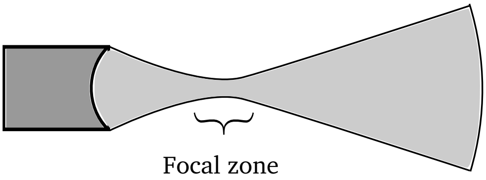

Figure 1.5: Illustration of focused transducer. The ultrasonic beam is narrow in the focal zone, but widens as the distance from the transducer increases.

1.2 List of publications

In the process of writing this thesis, I have been the first author on three peer-review journal articles. One of these has been published, one has been accepted for publication, and one is currently in review:

- Skjelvareid, M. H., Olofsson, T., Birkelund, Y., and Larsen, Y. (2011c). Synthetic aperture focusing of ultrasonic data from multilayered media using an omega-k algorithm. *IEEE Trans. Ultrason., Ferroelectr., Freq. Control*, *58*(5), 1037–1048

- Skjelvareid, M. H., Birkelund, Y., and Larsen, Y. (2012b). Synthetic aperture focusing of outwardly directed cylindrical ultrasound scans. Submitted to *IEEE Trans. Ultrason., Ferroelectr., Freq. Control* January 2012, accepted for publication July 2012.

- Skjelvareid, M. H., Birkelund, Y., and Larsen, Y. (2012a). Internal pipeline inspection using virtual source synthetic aperture ultrasound imaging. Submitted to *NDT&E International* May 2012, currently in review.

I have also contributed to four conference articles, being the first author and presenter on three:

- Olofsson, T., Skjelvareid, M. H., and Barkefors, A. (2010). Ultrasonic imaging of immersed objects using migration techniques. In *European Conference on Synthetic Aperture Radar (EUSAR)*, (pp. 442–445)

- Skjelvareid, M. H., and Birkelund, Y. (2010). Ultrasound imaging using multilayer synthetic aperture focusing. In *ASME 2010 Pressure Vessels and Piping Conference*, vol. 5, (pp. 379–387)

- Skjelvareid, M. H., Olofsson, T., and Birkelund, Y. (2011b). Three-dimensional ultrasonic imaging in multilayered media. In *International Congress on Ultrasonics 2011, AIP Conference Proceedings*, vol. 1433, (pp. 169–172)

- Skjelvareid, M. H., Birkelund, Y., Olofsson, T., and Larsen, Y. (2011a). Ultrasonic imaging of pitting using multilayer synthetic aperture focusing. In *2011 IEEE Ultrasonics Symposium. Proceedings.*, (pp. 2042–2024)

1.3 Outline

The remaining chapters of this thesis can be divided into three main parts: Chapters 2 and 3 give an introduction to ultrasonic imaging and synthetic aperture processing, Chapters 4 and 5 present methods for imaging in multilayered media, and Chapters 6-8 describe methods for imaging in cylindrical geometries, with application to pipeline inspection. Finally, the thesis conclusions are given in Chapter 9, with suggestions for future work.

Chapter 2 describes the constituent elements of an ultrasonic imaging system, and the signals transmitted to and received from an ultrasonic transducer. The transducer directivity strongly affects the lateral resolution of an ultrasonic image, both before and after synthetic aperture processing, and is therefore discussed in some depth. The chapter also gives a short overview of different visualization techniques used to display ultrasonic data.

Chapter 3 introduces the concept of aperture synthesis. It is shown that monostatic pulse-echo measurements can be treated as array measurements of the wave field produced by exploding reflectors, and time- and Fourier-domain synthetic aperture algorithms are derived following the concept of wave field back-propagation. An analysis of the attainable lateral resolution is given, and the effects of synthetic aperture focusing are demonstrated on a point scatterer data set.

Chapter 4 expands the synthetic aperture algorithms in Chapter 3 to the case of multilayered media. The root-mean-square velocity is introduced as a means of calculating the pulse-echo delay times for time-domain multilayer imaging, and an efficient Fourier-domain algorithm is derived through a combination of the phase shift migration and the Stolt migration algorithms. The algorithms are compared in terms of both computational efficiency and imaging performance. The chapter is based on [Skjelvareid and Birkelund, 2010] and [Skjelvareid et al., 2011c].

Chapter 5 expands multilayer synthetic aperture imaging to three dimensions, and demonstrates its use in experiments on point-like scatterers and a plate with artificial corrosion pits. A comparison of 2D and 3D focusing for 3D data sets is also made. The chapter is based on [Skjelvareid et al., 2011b] and [Skjelvareid et al., 2011a].

Chapter 6 describes a Fourier-domain algorithm for synthetic aperture focusing of measurements performed over a cylindrical surface. A theoretical expression for the lateral resolution is derived, and the expression is verified through simulations and experiments. The effect of the angular sampling interval on grating lobe levels is also studied. The chapter is based on [Skjelvareid et al., 2012b].

Chapter 7 describes how the algorithm in Chapter 6 can be adapted for use with focused transducers, and demonstrates the modified algorithm in a realistic pipe inspection experiment. Synthetic aperture focusing is shown to significantly increase the lateral resolution in cases where the pipe wall is outside the transducer focal zone. The chapter is based on [Skjelvareid et al., 2012a].

Chapter 8 expands the algorithm described in Chapter 6 to multilayered media, and presents simulations and an experiment demonstrating its use. The research presented in this chapter has not yet been submitted to a journal. However, it is included to complete the treatment of multilayer imaging in the thesis.

Chapter 2

Ultrasonic imaging

Ultrasound is generally defined as all sound with a frequency above the threshold of human hearing. Ultrasonic transmitters and receivers are used in a large number of applications, for example medical imaging and treatment, non-destructive testing in industry, sonar imaging, and general range finding [Ensminger and Bond, 2012]. Ultrasonic waves are reflected or scattered by objects which have a higher or lower acoustic impedance than the surrounding medium. If multiple ultrasonic measurements are performed in a number of different positions, the resulting data set can be displayed as an image of acoustic reflectivity.

In this chapter, we present some of the basics of ultrasonic imaging, including the equipment used to generate and record ultrasonic waves. Special attention is given to the radiation patterns of ultrasonic transducers, and how these in turn affect the lateral resolution in ultrasonic imaging. At the end of the chapter, various visualization modes for one-, two- and three-dimensional ultrasonic data are discussed.

2.1 Ultrasonic transducers

An ultrasonic transducer is a device which is used to convert electrical signals to acoustic waves, and vice versa. Transducers are manufactured in a variety of ways, according to their application, but piezoelectric transducers are the most common. An illustration of a piezoelectric transducer is shown in Fig. 2.1.

The active element in the transducer is made of a piezoelectric material, which changes shape when it is subject to change in the electric field. The element can be made to expand or contract by applying a voltage across its electrodes, which in turn generates an acoustic wave. Similarly, the electric field in a piezoelectric material changes when it is subject to mechanical stress.

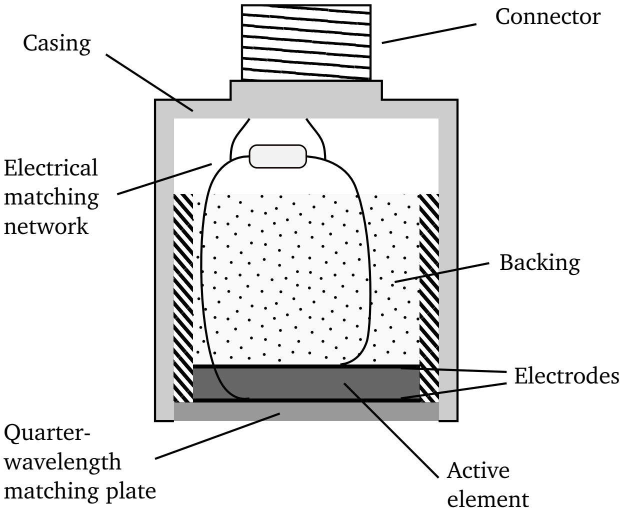

Figure 2.1: Constituent elements of an ultrasonic transducer for immersion testing.

When the pressure of a reflected acoustic wave makes the active element expand or contract, it generates a voltage across the electrodes, which can be read out and stored for further analysis [Ensminger and Bond, 2012].

The active element is attached to a backing material with high acoustic impedance and high acoustic attenuation, for example epoxy with tungsten particles. Without the backing material, the element would reverberate strongly at its resonance frequency, resulting in a long, resonant impulse and poor temporal resolution. For transducers made for radiation into water, so-called immersion transducers, an impedance matching layer is often applied to the front of the active element, to optimize the energy transfer into the outside medium. The thickness of the matching layer corresponds to a quarter of the wavelength at the transducer's center frequency [Olympus Corp., 2012].

2.2 Ultrasonic signal processing

This thesis is concerned with ultrasound systems in which the same transducer is used in both transmission and reception, so-called monostatic systems. A combined pulser/receiver is often used to generate the electrical excitation pulse, and to amplify and digitize the signal generated by the reflected echoes. A schematic of the elements in a pulser-receiver system is shown in Fig. 2.2.

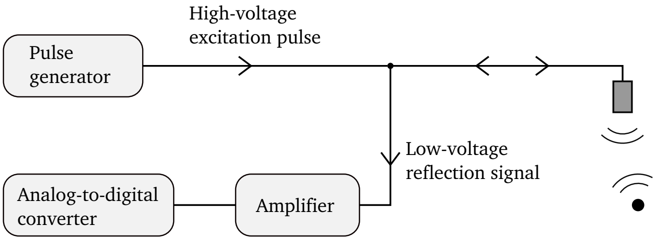

Figure 2.2: Schematic of elements in a pulser-receiver system. A pulse generator creates a high-voltage pulse which is transmitted to the transducer. Low-voltage signals created by backscattered echoes are first amplified and then digitized.

2.2.1 Excitation signals

The amplitude and shape of the transmitted pulse is determined by the excitation signal applied to the transducer. To obtain a sufficient signal-to-noise level, excitation signals are often several hundred volts in amplitude. The most common excitation signals for ultrasonic imaging are spike and square pulses, which can be generated with a simple RC circuit and a transistor switch [ASNT, 2007].

In radar and sonar imaging applications it is common to use long frequency modulated signals, known as *chirps*, as excitation signals [Hayes and Gough, 1992; Cumming and Wong, 2004]. Compared to pulse excitation signals, chirps increase the total transmitted energy without increasing the signal amplitude or decreasing the signal bandwidth. This in turn increases the signal-to-noise ratio of the measurement. The received signal is crosscorrelated with the emitted signal to increase the temporal resolution, a process termed *pulse compression*. A recent study by Misaridis and Jensen [2005] indicates that modulated excitation signals can also be used to improve the signal-to-noise ratio in ultrasonic imaging. Modulated excitation signals may thus become more common as the hardware cababilities of ultrasonic systems improve. However, in this thesis simple square excitation pulses have been used in all experiments.

2.2.2 Received signals

Figure 2.3 shows an example of a short square excitation pulse, the received signal from the transducer, and the frequency spectrum of the received signal. The received signal was produced by a reflection from an aluminium plate immersed in water. The pulse-echo response is a short wavelet, oscillating at a resonant frequency given by the thickness of the active element in the transducer. This frequency, often called the transducer *center frequency*, can be determined from the frequency spectrum of the pulse, shown in Fig. 2.3(c). For this transducer, the center frequency is approximately 1650 kHz. The

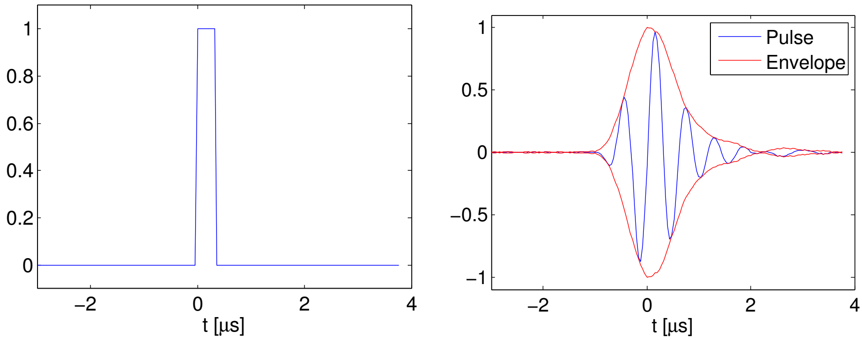

(a) Square pulse excitation signal

(b) Pulse-echo response

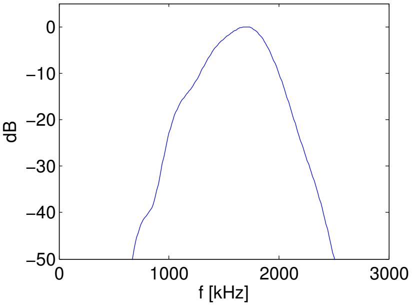

(c) Pulse frequency spectrum

Figure 2.3: Examples of excitation signal, pulse-echo response and pulse spectrum, obtained using an aluminium plate immersed in water. The time axis in Fig. 2.3(b) has been shifted so that the envelope peak occurs at $t = 0$, and the maximum amplitude has been normalized to 1 for all plots.

frequency spectrum also indicates the band-limited nature of the transducer.

In most applications, time delay and amplitude are the most important features of the received ultrasonic signal. These features are more easily extracted from the *envelope* of the wavelet than from the wavelet itself. In the example in Fig. 2.3(b), the envelope is shown as a red line. In many ultrasound systems, the envelope is estimated by simply rectifying the wave form, sometimes combined with low-pass filtering [Gammell, 1981]. However, this approach leaves ripples in the envelope, and low-pass filtering also reduces the temporal resolution. An alternative method is to calculate the analytic equivalent of the received signal, using the Hilbert transform, and to calculate the envelope by taking the absolute value of the analytic signal. This approach is superior to rectification and filtering, since it creates a smooth envelope with no reduction of temporal resolution [Gammell, 1981]. The envelope shown in Fig. 2.3(b) was calculated using this approach, and the same method is used consistently throughout the thesis. In practice, the analytic signal is calculated by taking the Fourier transform of the signal, setting negative frequency components to zero, multiplying the positive frequency components by two, and inverse Fourier transforming the resulting one-sided spectrum [Gammell, 1981].

2.3 Modes of wave propagation

In this thesis we only consider *bulk waves*, which are waves that can propagate through the volume of its medium, and not just along the surface. In liquid or gaseous media, the only type of bulk wave which can propagate is called a *longitudinal wave*, in which the particles of the medium move parallel to the direction of wave propagation. Solid media can support an additional type of bulk wave called *shear wave*, in which the particles move perpendicularly to the direction of the wave. Longitudinal and shear waves usually propagate at different velocities through the medium [Ensminger and Bond, 2012].

Wave energy can be converted between these two propagation modes when impinging on a defect or an interface between two layers. However, in the measurements we consider in this thesis, the waves emitted by the transducer are longitudinal, and impinge on layer interfaces with a normal or near-normal incidence. In this case the effect of mode conversion at interfaces is negligible [Ensminger and Bond, 2012, Sec. 4.2], and we will therefore assume that only longitudinal waves are present in the insonified region. When the term wave velocity is used, it refers to the velocity of longitudinal waves in the medium.

2.4 Transducer directivity

Most ultrasonic transducers are directive in nature, meaning that in transmission, acoustic waves are radiated within a limited beam. The shape of the beam determines the lateral resolution of the imaging system. To analyze the wave field generated by different transducer shapes, we assume that the sources are driven at a single angular frequency ω, and that the wave field is in a steady state. Thus, at an arbitrary observation point $\vec{r}$ in space, the sound pressure is given by

$$p(t, \vec{r}) = A(\omega, \vec{r}) \cdot e^{i\omega t}, \tag{2.1}$$

where $A(\omega, \vec{r})$ denotes the complex amplitude of the wave field. The physically observed wave field is obtained by taking the real part of $p(t, \vec{r})$. For broadband excitation signals, like a short pulse, the wave field is given by a combination of all single-frequency solutions,

$$p(t, \vec{r}) = \int_{-\infty}^{\infty} A(\omega, \vec{r}) e^{i\omega t} \mathrm{d}\omega \ , \tag{2.2}$$

that is, the inverse Fourier transform of the frequency-domain solution. To simplify notation, the $e^{i\omega t}$ term is omitted from the following discussion.

2.4.1 Boundary conditions

To derive analytical solutions for the emitted wave field of acoustic sources, we assume the following simplifying boundary conditions [Kinsler et al., 1999; Williams, 1999]:

- **Piston source:** The amplitude and phase of the normal velocity is uniform across the source. This model has proven to be valid for many commercial transducers [Schmerr and Song, 2007, Ch. 8].
- **Rigid baffle:** The source is mounted in an infinite baffle, a boundary flush with the surface of the source. The baffle is completely rigid, i.e., the normal velocity of the baffle is zero at all times. In practice, the infinite baffle model is also a good approximation for ultrasound transducers without a baffle, as long as the transducer diameter is significantly larger than the wave length [Schmerr and Song, 2007, Ch. 8].

2.4.2 Point source

For a simple baffled point source with volume velocity Q^1, located at the origin of the coordinate system, the sound field at an arbitrary observation point $\vec{r}$ is given by [Kinsler et al., 1999]

$$p(\vec{r}) = \underbrace{\frac{i\rho c Q}{\lambda}}_{A_P} \cdot \underbrace{\frac{e^{ikr}}{r}}_{H(r)} , \tag{2.3}$$

where ρ and c denotes the density and wave velocity of the propagating medium, λ denotes wave length, and $k = \omega/c$. The length of $\vec{r}$ is denoted simply as r. The wave field is given by a constant factor, denoted A_P, and a second factor, denoted $H(r)$, whose phase and amplitude changes with the distance to the source. The physical explanation for the amplitude decreasing with distance is that the wave energy is spread out over a spherical wave front, whose surface increases with distance. This effect is termed *geometrical spreading*, and is also observed for finite-sized sources [Kinsler et al., 1999].

2.4.3 Circular source

The geometry of a flat, circular source is illustrated in Fig. 2.4. Because of the circular geometry, the wave field is symmetric about the z axis, and we can assume that the observation point is in the x–z plane without loss of generality. The angle between the $\vec{r}$ and the z axis is denoted θ.

Close to the source, the wave field produced by the source is quite complex, with several local minima and maxima. However, in the *far field* of the source, where $r \gg D$, the wave field takes on a simpler form which can be described

---

[1] $Q = \frac{\mathrm{d}V}{\mathrm{d}t}$. where V denotes the source volume

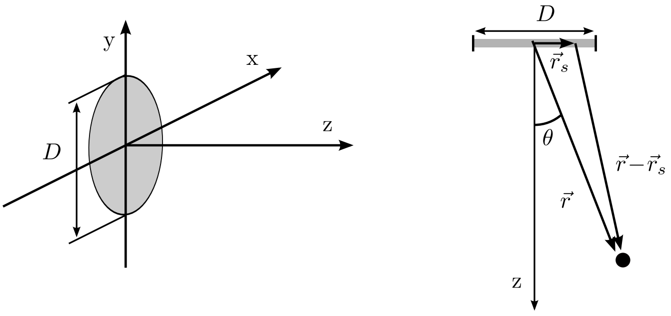

Figure 2.4: Circular source in baffle. Left: 3D source geometry. Right: Source geometry in plane intersecting with z axis.

with approximate analytical expressions. The end of the near field is usually defined as $N = D^2/(4\lambda)$, and for $r > 3N$, far field approximations are very accurate [Schmerr and Song, 2007, Ch. 8].

It can be shown [Williams, 1999, Eq. 2.106] that under far field conditions, the wave field from a circular source with uniform velocity amplitude u_0 is given by

$$p(r,\theta) \approx \underbrace{\frac{i\pi\rho c D^2 u_0}{4\lambda}}_{A_C} \cdot \underbrace{\frac{e^{ikr}}{r}}_{H(r)} \cdot \underbrace{\frac{2J_1\left(\pi\frac{D}{\lambda}\sin\theta\right)}{\pi\frac{D}{\lambda}\sin\theta}}_{D_C(\theta)} , \tag{2.4}$$

where J_1 is a Bessel function of the first kind, of order 1. Thus, the wave field in the observation point (r, θ) is given by three terms, denoted A_L, $H(r)$ and $D_C(\theta)$. Noting that the volume velocity of the source is given by $Q = \pi u_0 D^2/4$, we see that the A_C and $H(r)$ terms correspond to the wave field produced by a point source. The additional $D_C(\theta)$ term, called the *directivity function* of the source, represents an angle-dependent scaling of the wave field amplitude.

The directivity function is on the form $J_1(x)/x$ and is similar in shape to the *sinc* function. Because of this similarity it is referred to as the *jinc* function [Goodman, 1996]:

$$\mathrm{jinc}(x) = 2 \cdot \frac{J_1(x)}{x} . \tag{2.5}$$

The factor 2 is included in the definition to make $\lim_{x\to 0} \mathrm{jinc}(x) = 1$. Using the jinc function, we rewrite the directivity function in (2.4) as

$$D_C(\theta) = \mathrm{jinc}\left(\pi\frac{D}{\lambda}\sin\theta\right) . \tag{2.6}$$

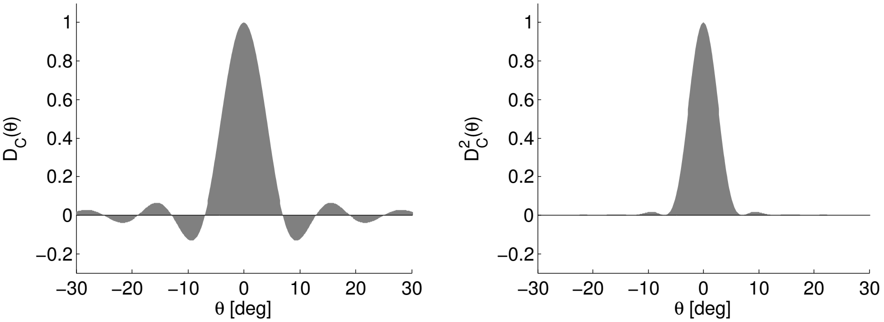

(a) Transmission directivity, linear (b) Pulse-echo directivity, linear

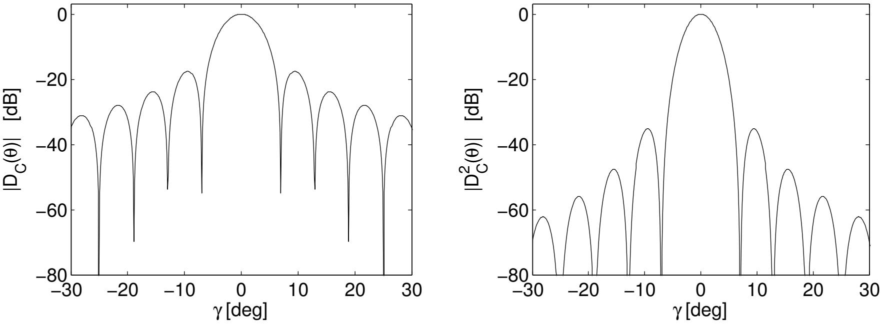

(c) Transmission directivity, logarithmic (d) Pulse-echo directivity, logarithmic

Figure 2.5: Directivity functions for a circular source with $D/\lambda = 10$, for transmission (Fig. (a) and (c)) and combined transmission and reception (Fig. (b) and (d)).

2.4.4 Pulse-echo directivity

In this thesis we are mainly concerned with pulse-echo applications, in which the same transducer is used for both transmission and reception. Because of acoustic reciprocity, the directivity function is identical in transmission and reception, and the combined pulse-echo directivity function is given by squaring the transmission directivity function [Kinsler et al., 1999, Sec. 7.7].

$$D_{C,PE}(\theta) = D_C^2(\theta) = \mathrm{jinc}^2\left(\pi \frac{D}{\lambda} \sin\theta\right). \tag{2.7}$$

A comparison of the transmission and pulse-echo directivity functions for a circular source with $D/\lambda = 10$ is shown in Fig. 2.5. Even though the zero crossings are the same for both cases, the pulse-echo directivity has a sharper main lobe and significantly lower sidelobes.

We will use the Full Width at Half Maximum (FWHM), also known as the

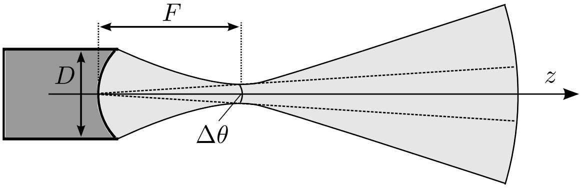

Figure 2.6: Illustration of focused transducer, with indication of focal length, F, and angular beamwidth at the focal point, $\Delta\theta$.

-6 dB width[2], as a practical measure of the pulse-echo beamwidth. The squared jinc function in (2.7) drops to half its maximum value when

$$\sin\theta = \pm 0.515\frac{\lambda}{D} \ . \tag{2.8}$$

When $D \gg \lambda$, which is the case for most ultrasound transducers, the main lobe is relatively narrow, and the small terms approximation $\sin\theta \approx \theta$ can be applied. Rounding off 0.515 to 0.5, we obtain a simple, approximate expression for the -6 dB beamwidth:

$$\Delta\theta \approx \frac{\lambda}{D} \ . \tag{2.9}$$

2.4.5 Focused source

For a circular, focused source with uniform velocity, the directivity function at the focal point is approximately given by a jinc function [O'Neil, 1949],

$$D_{C,F}(\theta)|_{z=F} = \text{jinc}\left(\pi\frac{D}{\lambda}\sin\theta\right) , \tag{2.10}$$

where $z = F$ is the focal length, as indicated in Fig. 2.6. Comparing (2.10) with (2.6), we see that at the focal point, the directivity function for the focused transducer has the same form as for the plane, unfocused transducer. However, while plane transducers are usually operated in far field conditions, the focal point of a focused transducer is usually within the near field [Schmerr and Song, 2007]. A focused transducer can therefore yield a higher lateral resolution than a plane transducer of the same size. Note that beyond the focal point the beam is strongly divergent, and the beamwidth is larger than that given by (2.10).

2.5 Axial and lateral resolution

The resolution of an ultrasonic imaging system is determined through its point spread function (PSF), the response produced by an infinitely small scatterer.

---

[2] The dB scale is described in Section 2.6.1

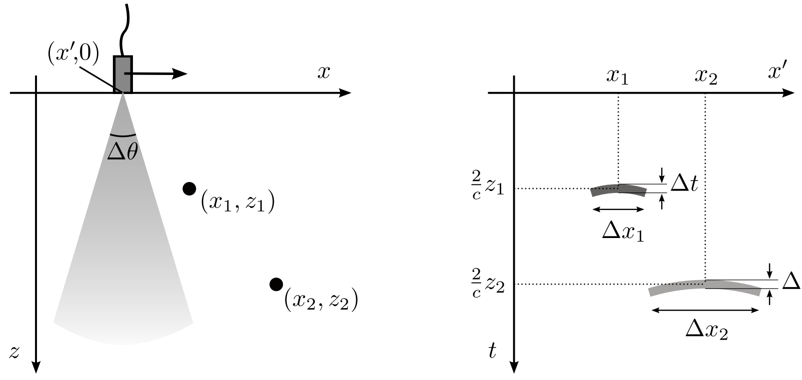

(a) (b)

Figure 2.7: Illustration of linear scan of two point scatterers. (a) Measurement geometry. (b) Pulse-echo response.

In practice, the PSF is measured using very small scatterers, for example thin steel wires.

Figure 2.7(a) illustrates an ultrasonic scan of two point scatterers, where the transducer is scanned along the x axis, continuously emitting pulses. When one or both of the point scatterers are within the transducer beam, given by the beamwidth $\Delta\theta$, the pulses are reflected back towards the transducer. The pulse-echo response of the scan is shown in Fig. 2.7(b), plotted as a 2D image with two-way delay time on the vertical axis and transducer position on the horizontal axis. This presentation mode is called a *B-scan*[3].

The scatterers yield two slightly curved responses, whose widths are given by the width of the transducer beam. The responses are curved because the transducer-scatterer distance varies within the beam. For scatterer coordinates (x_i, z_i) the distance is given by the hyperbola $r_i = \sqrt{(x_i - x')^2 + z_i^2}$. The thickness of each response is given by the pulse duration Δt, which yields a resolution along the z axis approximately equal to

$$\Delta z \approx \Delta t \cdot \frac{c}{2} \ . \tag{2.11}$$

Since the transducer beam expands in the x direction as z increases, the response from the second scatterer is wider that that of the first scatterer. The width of the transducer beam along the x axis is given by

$$\Delta x(z) = 2z \cdot \sin\left(\frac{\Delta\theta}{2}\right) \approx z\Delta\theta \ . \tag{2.12}$$

Δz and Δx determine the *axial* and *lateral* resolution of the ultrasonic image, respectively. Whereas Δz does not change significantly with depth, Δx

---

[3] Different modes of presentation are discussed further in Section 2.6.

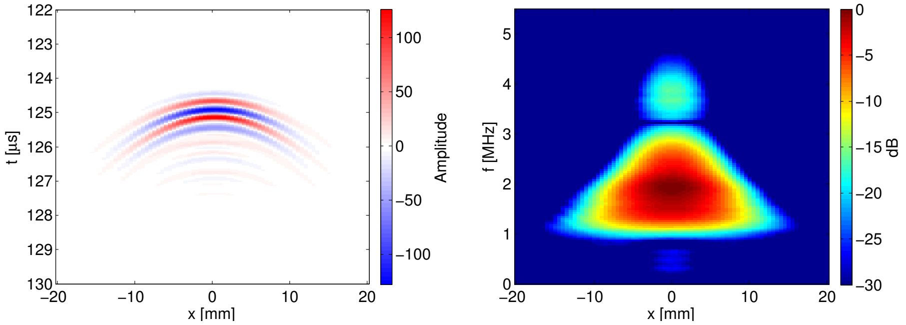

(a) Point scatterer B-scan (b) Frequency spectrum

Figure 2.8: Point scatterer response from lateral ultrasound scan, with corresponding frequency spectrum.

increases linearly with depth. At large depths, this effect causes a significant lateral smearing of the ultrasonic image, limiting the usable range of the imaging system.

An example of a B-scan for a real point-like scatterer is shown in Fig. 2.8(a). The B-scan was produced with a plane, circular transducer, with 2.25 MHz center frequency and 6 mm diameter, scanning a 1.5 mm thick steel wire at a distance of 93 mm. The B-scan illustrates that the beam profile varies smoothly with lateral offset, and that it does not have sharply defined side edges, as suggested by the drawing in Fig. 2.7.

In the discussion on directivity functions in Section 2.4, it was assumed that the sources were driven at a single angular frequency, ω. However, most transducers used in ultrasonic imaging are made to have a short pulse length Δt, and thus also a relatively wide frequency range. The beamwidth, given by $\Delta\theta \approx \lambda/D$, can therefore vary significantly within the transducer passband. This is illustrated in Fig. 2.8(b), which shows the frequency spectrum of the point scatterer response in Fig. 2.8(a). The triangular shape of the spectrum shows that the transducer beam is broad at low frequencies and narrower at high frequencies.

2.6 Displaying ultrasonic data

2.6.1 Decibel

The decibel (dB) is often used to indicate the ratio between two measurements of power or intensity. If for example the acoustic intensity in a reference point is denoted by I_0, and the acoustic intensity in another point is denoted with I, the ratio between the two can be expressed as

$$L_{dB} = 10 \log_{10}(I/I_0) \ . \tag{2.13}$$

For harmonic waves in free space, the acoustic intensity is proportional to the square of the acoustic pressure amplitude, $I \propto p^2$. Thus, the dB level in (2.13) can also be expressed in terms of the acoustic pressure [Kinsler et al., 1999, Sec. 5.12],

$$L_{dB} = 10\log_{10}(I/I_0) = 10\log_{10}(p^2/p_0^2) = 20\log_{10}(p/p_0)\ . \tag{2.14}$$

This has led to the convention that when the ratio of two sound pressure amplitudes is expressed in dB, the logarithm of the ratio is multiplied by 20 rather than 10. In this thesis, all measured ultrasonic signals are amplitude values, and whenever the decibel is applied, a multiplication factor of 20 is used.

The features of an ultrasonic image are usually observed as variations in the backscattered amplitude, and the absolute amplitude values are often not relevant. It is then convenient to use the maximum amplitude as the reference for the dB level. For example, if $e(t)$ represents the envelope of an ultrasonic pulse, the time-continuous envelope dB level is calculated as

$$e_{dB}(t) = 20\log_{10}\left(\frac{e(t)}{\max\{e(t)\}}\right), \tag{2.15}$$

so that $\max\{e_{dB}(t)\} = 0$. In this thesis, such normalization with the maximum value is applied consistently whenever dB values are plotted. For 2D and 3D data sets the global maximum is used.

2.6.2 A-scan

The term A-scan is used to describe the plot of a single ultrasonic measurement, with time on the horizontal axis and amplitude on the vertical axis. The A-scan

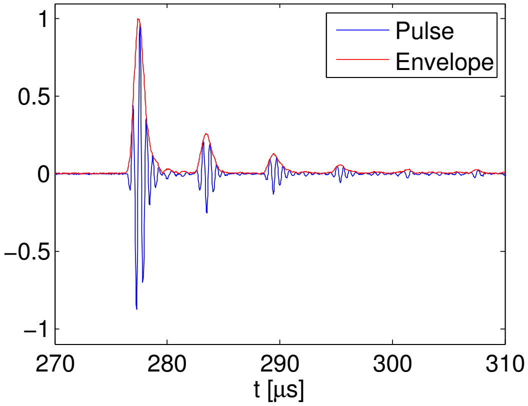

Figure 2.9: Example of A-scan, obtained by pulse-echo measurement of immersed aluminium plate.

display is used for studying the exact shape of the ultrasonic signal, and for determining the amplitude and time delay of different reflections.

An example A-scan, obtained by pulse-echo measurement of an aluminium plate immersed in water, is shown in Fig. 2.9. The low-amplitude wavelets following the main reflection are caused by internal reflections within the plate, and the time delay between the wavelets can be used to estimate the plate thickness.

2.6.3 B-scan

An ultrasonic B-scan is a presentation of multiple ultrasonic waveforms, acquired at different spatial positions, typically along a straight line. The ultrasonic data is displayed as an image, with pulse-echo delay time on one axis and spatial displacement on the other.

A B-scan can be displayed in several different ways, depending on the application. Figure 2.10 shows an example of the same B-scan plotted in four different versions. The B-scan is part of the experiment described in Section 4.5, and was made by scanning an acrylic glass block with four side-drilled holes.

In Fig. 2.10(a), the amplitude of the raw waveform is displayed, with positive values shown as light and negative values shown as dark. The corresponding B-scan envelope is shown in Fig. 2.10(b), plotted on a linear scale. It is very common for ultrasonic data to have a high dynamic range, and in many cases it is better to display the envelope on a logarithmic scale. Two examples of this are shown in Figs. 2.10(c) and 2.10(d), with dynamic ranges of 30 and 60 dB, respectively. When a large dynamic range is used, more low-amplitude details are shown in the image, including background noise.

Envelope images are often shown using a continuous gray scale. However, in some cases the image can be made less cluttered by displaying it as a contour plot, where a number of threshold values are traced out with a contour line, and values between the threshold values are given a single color. In Fig. 2.11, one of the reflections shown in 2.10 is shown both as a continuous grayscale image and as a contour plot. The latter enables us to easily determine the width of the response at different contour values.

2.6.4 C-scan

The term C-scan is used to describe an image where both the horizontal and vertical axis represent spatial coordinates, and the color or gray level of the image represents some feature of the ultrasonic signal. The amplitude and time-of-flight of the backscattered ultrasonic pulse are the two most commonly used features, extracted by detecting the maximum envelope value at each measurement position. The time-of-flight is used to indicate the distance to a scatterer, and time gating can be applied to study reflections from within a limited distance interval. Figure 2.12 illustrates how two-dimensional images

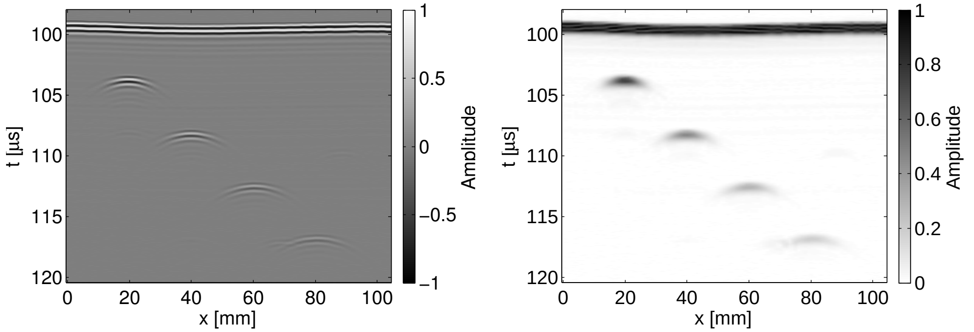

(a) Ultrasonic wave form (b) Envelope, linear gray scale

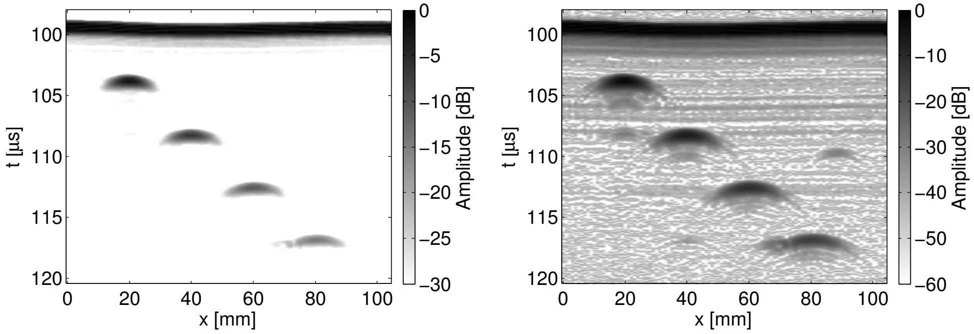

(c) Envelope, logarithmic scale, 30 dB range (d) Envelope, logarithmic scale, 60 dB range

Figure 2.10: B-scan of side-drilled holes in acrylic glass block, displayed in four different ways.

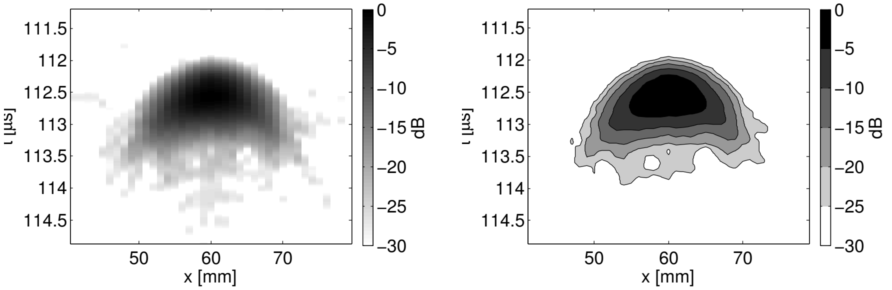

(a) Continuous grayscale (b) Contour plot

Figure 2.11: Comparison of continuous grayscale plot and contour plot.

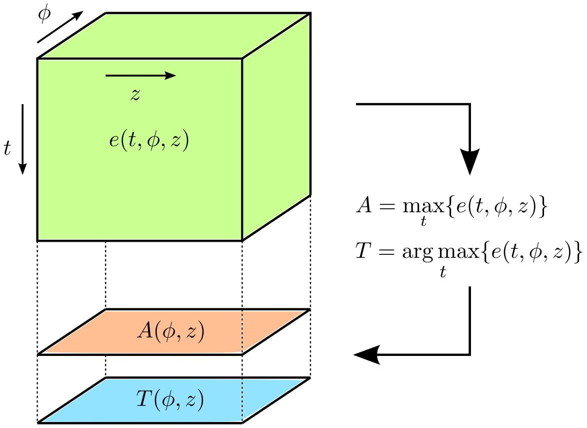

Figure 2.12: Creating amplitude and time-of-flight C-scans from 3D ultrasonic data. A search for the maximum is performed along the t axis of the 3D envelope data set $e(t, \phi, z)$, and the amplitudes and positions of the detected maxima are shown as 2D images $A(\phi, z)$ and $T(\phi, z)$.

of amplitude and time-of-flight, termed $A(\phi, z)$ and $T(\phi, z)$, are extracted from a three-dimensional envelope data set, with time on one axis and cylindrical coordinates ϕ and z other.

An example of the use of C-scans is given in Fig. 2.13. Four metal objects were placed inside a pipe, as shown in Fig. 2.13(a), and a transducer was scanned over a cylindrical measurement surface centered inside the pipe. C-scans of amplitude and distance were extracted, and the results are shown in Figure 2.13(b) and 2.13(c). The example is taken from the experiment described in Section 7.A.

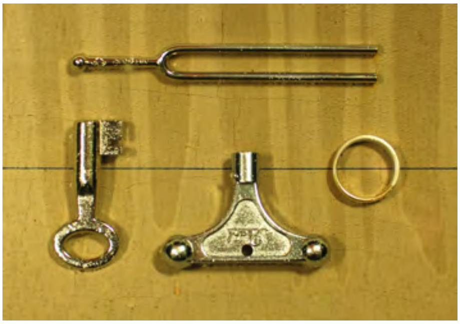

(a) Photography

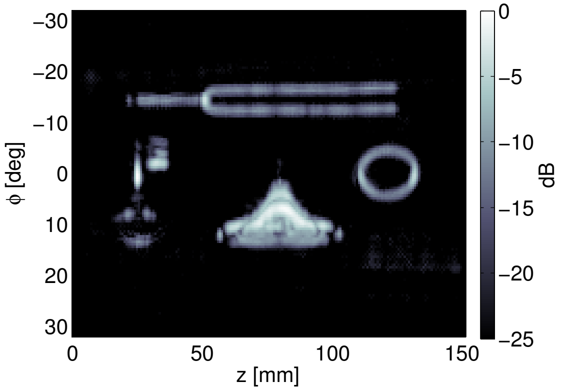

(b) Amplitude C-scan

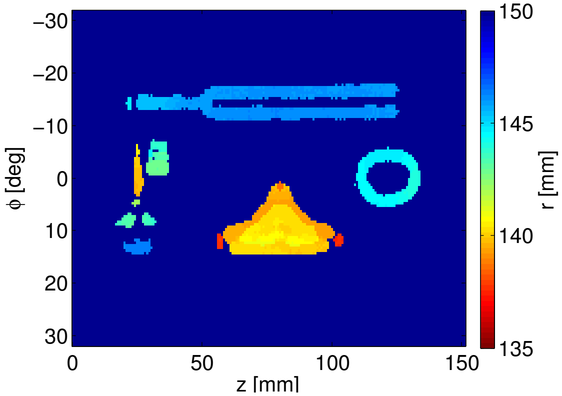

(c) Distance C-scan

Figure 2.13: Example C-scans of objects in pipe, taken from the experiment described in Section 7.A.

Chapter 3

Synthetic aperture imaging

In the previous chapter, we saw that the divergence of the ultrasonic beam causes the lateral resolution in ultrasound images to decrease with increasing range. However, the lateral resolution can be significantly increased by applying synthetic aperture focusing in post-processing. In this chapter, we introduce the synthetic aperture concept, and describe the algorithms which form the basis for Chapters 4 and 5.

The first algorithms for synthetic aperture ultrasound imaging were based on delay-and-sum beamforming in the time domain [Doctor et al., 1986; Kino et al., 1980; Burch and Burton, 1984], and time domain methods are still actively researched [Jensen et al., 2006; Lingvall and Olofsson, 2007; Andresen et al., 2011]. However, several Fourier-domain algorithms have also been introduced, enabling more efficient algorithm execution [Nagai, 1985; Langenberg et al., 1986; Mayer et al., 1990; Busse, 1992; Ylitalo and Ermert, 1994; Stepinski, 2007]. In this chapter we present three synthetic aperture algorithms; the delay-and-sum (DAS) algorithm, the phase shift migration algorithm [Gazdag, 1978], and the Stolt migration algorithm [Stolt, 1978]. The two latter were initially introduced for processing of seismic data, but have been used in both radar, sonar and ultrasound applications [Gough and Hawkins, 1998; Cumming and Wong, 2004; Stepinski, 2007; Olofsson, 2010]. The Stolt migration algorithm is also known as $\omega-k$ migration [Cafforio et al., 1991], $f-k$ migration [Margrave, 2003], and the wavenumber algorithm [Gough and Hawkins, 1998].

Even though many ultrasound imaging applications are three-dimensional in nature, we describe the algorithms in this chapter assuming a two-dimensional geometry. This simplifies the discussion of synthetic aperture concepts, and enables easy comparison with the two-dimensional algorithms used in synthetic aperture radar and sonar. Full three-dimensional imaging is discussed in later chapters.

Towards the end of the chapter, we discuss the theoretical lateral resolution attainable with synthetic aperture focusing, and how this relates to the spatial sampling interval. Finally, the effect of synthetic aperture focusing is demonstrated on a scan of a point-like scatterer.

3.1 Aperture synthesis

The term *synthetic aperture* is used as an analogy with traditional imaging systems, where the physical size of the aperture determines the attainable resolution. Consider for example the two focused transducers shown in Fig. 3.1. Both transducers have the same size L, but they are focused at different depths, z_1 and z_2, where $z_2 > z_1$. We know from (2.9) and Section 2.4.5 that the -6 dB width of the beam at the focal depth z_i is approximately

$$\Delta x \approx \frac{\lambda}{L} \cdot z_i. \tag{3.1}$$

Thus, since $z_2 > z_1$, the beamwidth at the focal point is larger for transducer 2 than for transducer 1. To make the beamwidth of transducer 2 similar to transducer 1, and obtain the same lateral resolution, we would have to increase the size of transducer 2 [1].

Now consider the synthetic aperture measurement geometry shown in Fig. 3.2. An unfocused transducer with beamwidth $\Delta\theta$ is scanned along the x axis, performing pulse-echo measurements in a large number of positions. These individual measurements can be used to synthesize a focused aperture. At any

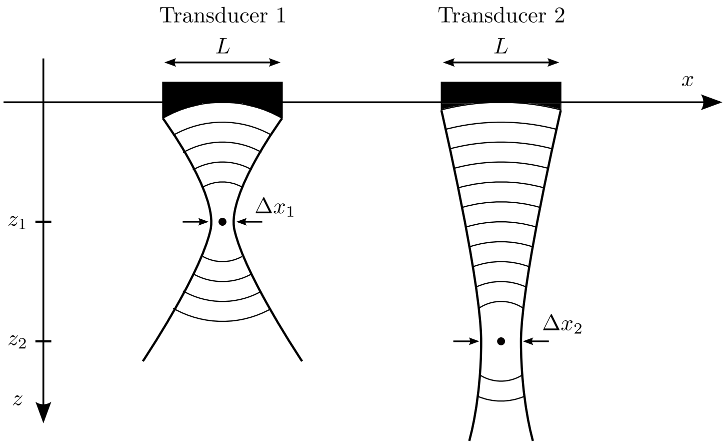

Figure 3.1: Transducers focused at two different depths.

---

[1] Alternatively, we could increase resolution by decreasing the wave length λ, but we will assume here that λ is constant.

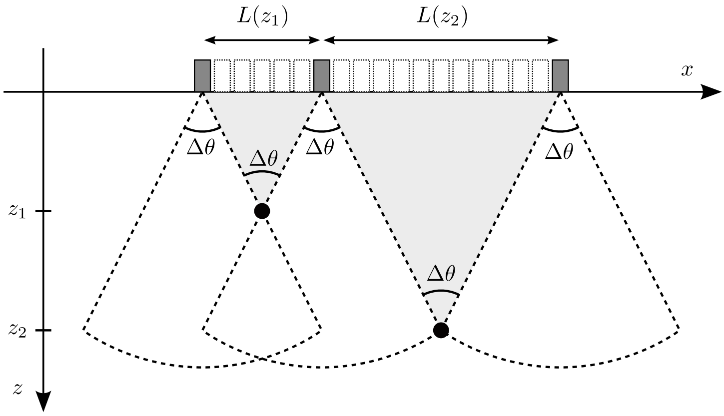

Figure 3.2: Synthetic aperture measurement geometry. The effective aperture size grows as the distance to the target increases.

depth z, a point is insonified by the transducer from the same range of angles, $\Delta\theta$. The effective size of the synthetic aperture, $L(z)$, grows as z increases,

$$L(z) = 2z \tan \frac{\Delta\theta}{2} \approx z \cdot \Delta\theta. \tag{3.2}$$

This effect is illustrated in Fig. 3.2, where $L(z_2) > L(z_1)$. Because the aperture grows proportionally to the depth, the lateral resolution after synthetic aperture processing is the same in the entire imaged region. For a plane transducer of length L, the lateral resolution is [Gough and Hawkins, 1998]

$$\Delta x_{\text{synth. ap.}} \approx \frac{L}{2}. \tag{3.3}$$

A detailed derivation of this relation is given in Section 3.6.1. Thus, while the resolution of a physically focused transducer depends on transducer size, wave length and focal depth, the lateral resolution after synthetic aperture focusing depends purely on the transducer size. The resolution is also high in the entire imaged region, and not only in a limited focal zone. These properties make synthetic aperture systems very flexible, and enable high-resolution imaging at large distances.

3.2 Exploding reflector model

In this thesis we are mainly concerned with measurements in which a single transducer transmits a pulse and records the backscattered echoes, for a number of different measurement positions. An illustration of such pulse-echo measurements of a single scatterer is shown in Fig. 3.3(a). In the

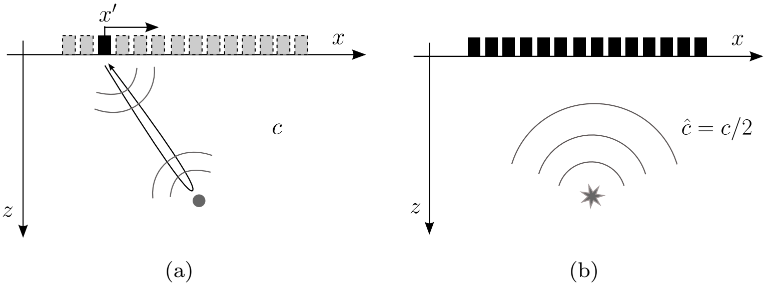

Figure 3.3: Exploding reflector model. A number of pulse-echo measurements of a point scatterer, shown in (a), can be modeled as an array measurement of an exploding reflector, as shown in (b). The effective wave velocity is then half the actual wave velocity.

resulting ultrasonic data set, the response from the point scatterer is given by a hyperbolic curve, $t = 2r/c$, where t denotes pulse-echo delay and r denotes the transducer-scatterer distance.

To simplify the derivation of synthetic aperture algorithms, these pulse-echo measurements can be interpreted as an array measurement of a single acoustic event, as shown in Fig. 3.3(b). If we assume that the scatterer acts like a source, emitting a pulse at $t = 0$, and that the effective wave velocity is half the actual velocity, $\hat{c} = c/2$, the wave field recorded by the transducer array has the same hyperbolic shape as for the pulse-echo case. The same interpretation can be applied for scatterers of finite size.

This interpretation, which is often referred to as the *exploding reflector model*, is commonly used in processing of seismic data [Claerbout, 1985; Margrave, 2003]. It is valid for both homogeneous and layered media, and we will apply it consistently throughout this thesis. The application of the model is identified in equations and figures by the use of the effective wave velocity, $\hat{c}$. In the derivations presented in this chapter, the exploding reflector model enables us to consider point sources rather than point scatterers.

3.3 Backpropagation concept

Consider a point source emitting a spherical wave, as shown in Fig. 3.4. If the wave field is recorded by an array, reversed in time, and re-emitted, it will create a new wave field which converges on the point source. The same will occur for any source, independent of shape. This self-focusing effect is sometimes termed *time reversal*, and it is possible due to the symmetry of the wave equation with regard to time [Fink, 1997].

The wave field from the source is maximally concentrated at the time instant when the pulse is emitted, which we define as $t = 0$, without loss of generality. This is true both for the initial transmission of the pulse, and for

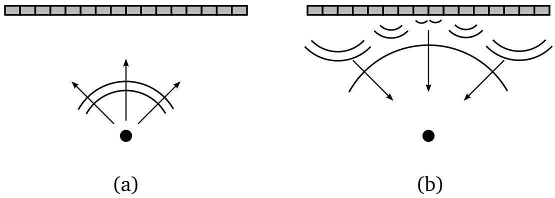

Figure 3.4: (a) Array measurement of point source wave field. (b) Backpropagation of wave field by time reversal.

the time-reversed, backpropagated wave field. Thus, at $t = 0$ the wave field represents a focused image of the source. This is the basis for imaging through backpropagation [Margrave, 2003]:

- Record the wave field using a transducer array
- Emulate the backpropagation of the wave field in software.
- Evaluate the wave field at $t=0$ to create a focused image

Note that accurate backpropagation requires that the wave velocity in the insonified region is known. The concept is valid for complex source geometries as well as simple point sources, but only for waves which follow a direct path from the source to the transducer array.

3.4 Time-domain backpropagation

3.4.1 Algorithm formulation

Consider the geometry shown in Fig. 3.5. A point source is located in (x, z), and emits a short pulse at $t = 0$, denoted $s_0(t)$. The wave field is then recorded along a the x-axis at depth Z. For the single layer case described here, Z is often set equal to zero, but we will use Z to be consistent with the notation in subsequent chapters. The signal recorded at (x', Z) is scaled and time delayed according to the distance r to the source [Kinsler et al., 1999],

$$s(t, x') = \frac{s_0(t - r/\hat{c})}{r}, \tag{3.4}$$

where $r = \sqrt{(x - x')^2 + (z - Z)^2}$. Assume now that at every measurement position x', the signals are time-reversed and emitted back into the propagating medium. We denote the time-reversed signals $s^*(t, x')$. At (x, z) the wave field is given by the superposition of the waves emitted from all points along the measurement line,

$$p(t, x, z) = \int \frac{s^*(t - \frac{r}{\hat{c}},\ x')}{r}\, \mathrm{d}x' = \int \frac{s(\frac{r}{\hat{c}} - t,\ x')}{r}\, \mathrm{d}x', \tag{3.5}$$

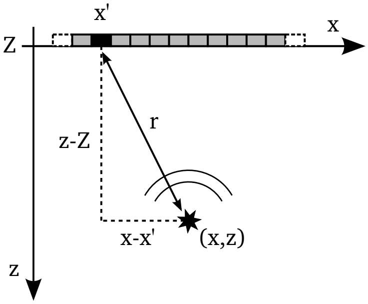

Figure 3.5: Point source geometry.

where the relation $s^*(t) = s(-t)$ is used in the last transition. Applying the imaging condition $t = 0$, as discussed in Section 3.3, and replacing the $1/r$ scale factor with a general apodization weight $\alpha(x)$, the focused image pixel value at (x_0, z_0) is given by [Langenberg et al., 1986]

$$i_p(x, z) = \int \alpha(x) \cdot s(r/\hat{c}, x') \; \mathrm{d}x'. \tag{3.6}$$

Thus, the formation of a single pixel corresponds to an integration along the hyperbola $t = r/\hat{c}$ in the $t - x'$ domain, weighted with apodization factors α. With a finite number of measurement positions, the integration corresponds to a summation of recorded signals with different time delays applied, and the approach is therefore often called *delay-and-sum* (DAS). We will use this term throughout the thesis.

In practice, the shape and location of the source(s) generating the wave field is not known, and the imaging procedure given by (3.6) must be repeated for all points of interest. This is essentially a two-dimensional correlation between the recorded data and the hyperbolic shape of the point source response, as shown in Fig. 3.6. A flow-chart summarizing the delay-and-sum algorithm is shown in Fig. 3.7.

3.4.2 Apodization

Apodization is often applied in time-domain synthetic aperture focusing to reduce the effect of sidelobe artifacts in the focused image [Frazier and O'Brien Jr., 1998; Martinez et al., 1999]. The synthetic aperture is usually weighted with a function approaching zero at the edges.

Since the size of the synthetic aperture increases with the distance from the transducer, as shown in Fig. 3.2, the width of the apodization function should be adjusted accordingly. An example for scatterers at two different depths is shown in Fig. 3.8. The width of the synthetic aperture at z is given by $\Delta x(z) = 2z \tan(\Delta\theta/2)$, where $\Delta\theta$ denotes the angular beamwidth of the

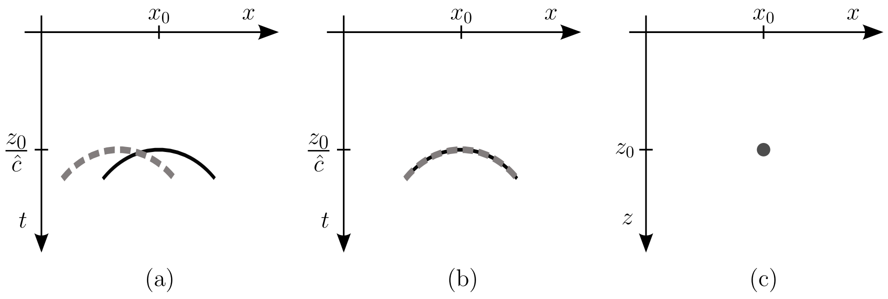

Figure 3.6: Time-domain backpropagation shown as 2D correlation with the point spread function in the $t - x$ domain. The solid black line is the response from a point source at (x_0, z_0), and the gray dashed line is the imaging integration path. (a) Mismatch between integration path and point spread function. (b) Integration path and point spread function perfectly overlapping. (c) Final image. Only the source position indicates strong correlation.

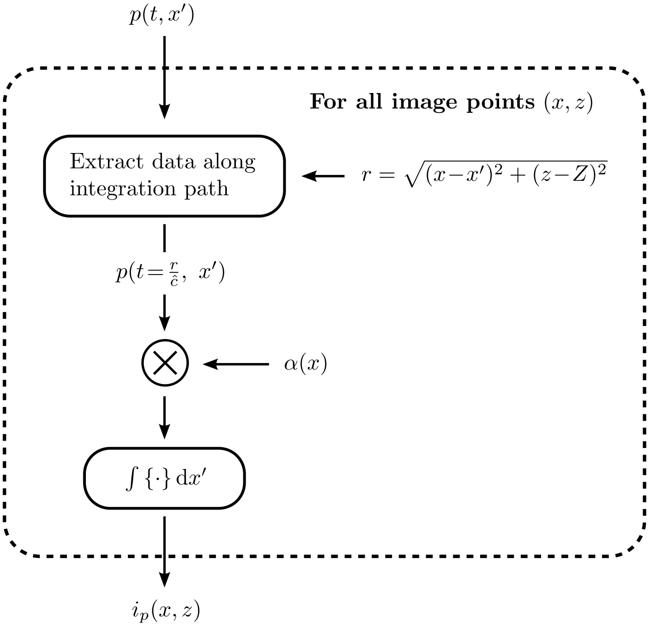

Figure 3.7: Algorithm flowchart for time-domain backpropagation. For every pixel position (x, z), a one-dimensional vector corresponding to $t = r/\hat{c}$ is extracted from the two-dimensional data set. The vector is multiplied with apodization weights α and summed, producing the image pixel $i_p(x, z)$.

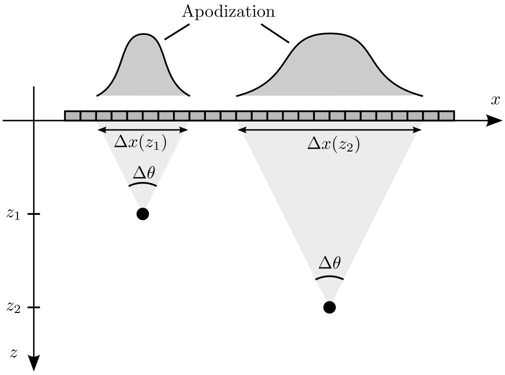

Figure 3.8: Illustration of synthetic aperture apodization for scatterers at different depths z. The size of the synthetic aperture grows with increasing distance, and the width of the apodization function must be adjusted accordingly.

transducer. The apodization function can be adjusted to the synthetic aperture by using normalized x coordinates,

$$\hat{x} = \frac{x - x'}{\Delta x(z)}. \tag{3.7}$$

In Section 3.7, imaging is performed with two different apodization functions; the rectangular function (uniform apodization) and the Hann function. The apodization coefficients for these can be expressed as

$$\alpha(\hat{x})_{\text{rect}} = \begin{cases} 1, & |\hat{x}| < 1/2, \\ 0, & \text{otherwise}, \end{cases} \tag{3.8}$$

and

$$\alpha(\hat{x})_{\text{Hann}} = \begin{cases} \frac{1}{2}\left[1 + \cos(2\pi\hat{x})\right], & |\hat{x}| < 1/2, \\ 0, & \text{otherwise}. \end{cases} \tag{3.9}$$

Note that the width of the apodization function depends on the value used for the beamwidth $\Delta\theta$. The beamwidth is frequency-dependent, as shown in Section 2.5, and the width of the apodization function can not match the beamwidth for all frequencies within the transducer passband. To include the complete synthetic aperture, the apodization function must be adjusted to the beamwidth at the lower edge frequency of the passband. The effect of apodization function width on the focused point spread function is discussed in Section 3.7.

3.4.3 Time-domain interpolation

The imaging integral given by (3.6) requires a summation of the recorded data, $p(t, x')$ along the hyperbola

$$t_{\text{das}} = \frac{1}{\hat{c}} \cdot \sqrt{(x - x')^2 + (z - Z)^2}. \tag{3.10}$$

In practice, the wave field is recorded at discrete time instants,

$$t = [0, 1, 2, \ldots, (N_t - 1)]/f_s + t_0, \tag{3.11}$$

where N_t denotes the number of samples, f_s denotes the sampling frequency, and t_0 denotes the time at which recording starts. However, t_{das} can take on any value, and thus may not coincide with any of the discrete time instants. An approximate value for $p(t_{\text{das}}, x')$ can be obtained by picking the closest data point, often called *nearest-neighbour interpolation.* If the sampling frequency is much higher than the transducer center frequency, $f_s \gg f_c$, the average error introduced by nearest-neighbour interpolation is relatively small. With lower sampling frequencies, more sophisticated interpolation methods are necessary. Alternatively, the wave field can be resampled to a higher sampling frequency, followed by nearest-neighbour interpolation [Lingvall et al., 2003].

3.5 Fourier-domain backpropagation

3.5.1 Fourier transforms

In a 2D geometry, solutions to the scalar wave equation are in the form of plane waves,

$$p(t, x, z) \propto e^{i(k_x x + k_z z - \omega t)}, \tag{3.12}$$

where k_x and k_z are the wavenumbers in the x and z direction, respectively. The relationship between k_x, k_z and ω is given by the dispersion relation

$$\frac{\omega^2}{\hat{c}^2} = k_x^2 + k_z^2, \tag{3.13}$$

and thus only two of the three variables are independent. In this thesis we choose k_z as the dependent variable. The most general solution to the wave equation is a combination of all possible solutions,

$$p(t, x, z) = \iint\limits_{-\infty}^{\infty} A(\omega, k_x) e^{i(k_x x + k_z z - \omega t)} \, \mathrm{d}k_x \, \mathrm{d}\omega, \tag{3.14}$$

where $A(\omega, k_x)$ denotes the complex amplitude for every (ω, k_x) combination. If we group the $A(\omega, k_x)$ and $e^{ik_z z}$ terms into a single term, denoted $P(\omega, k_x, z)$, we see that (3.14) corresponds to a two-dimensional inverse Fourier transform:

$$p(t,x,z) = \iint_{-\infty}^{\infty} \underbrace{A(\omega,k_x)e^{ik_z z}}_{P(\omega,k_x,z)} \; e^{ik_x x}e^{-i\omega t} \; \mathrm{d}k_x \; \mathrm{d}\omega. \tag{3.15}$$

Thus, $P(\omega,k_x,z)$ is the Fourier-domain equivalent to $p(t,x,z)$. Note the negative sign in the ω exponential in (3.15), which is usually positive in definitions of the inverse Fourier transform. However, when the Fourier transform is applied to 2D or 3D wave phenomena, it is common to use opposite signs for the wavenumber and frequency exponents [Claerbout, 1985]. With this convention, positive values for ω, k_x and k_z correspond to a wave which moves in the positive direction along the spatial axes. The forward Fourier transform is given by

$$P(\omega,k_x,z) = \frac{1}{4\pi^2}\iint_{-\infty}^{\infty} p(t,x,z) \; e^{-ik_x x}e^{i\omega t} \; \mathrm{d}x \; \mathrm{d}t, \tag{3.16}$$

where $\frac{1}{4\pi^2}$ is included in the definition as a normalization factor.

3.5.2 Wave field extrapolation

We assume that all sources are confined to the half-space $z > Z$, and that the wave field is recorded along the line $z = Z$, so that $P(\omega,k_x,Z)$ is known. Inserting this into (3.15), we can solve for $A(\omega,k_x)$, and obtain the expression

$$P(\omega,k_x,z) = P(\omega,k_x,Z)\cdot e^{ik_z(z-Z)}. \tag{3.17}$$

Thus, the Fourier domain wave field can be extrapolated from Z to z by multiplication with the phase term $e^{ik_z(z-Z)}$. This is known as extrapolation of the *angular spectrum* [Ratcliffe, 1956; Goodman, 1996; Williams, 1999]. We obtain an expression for k_z by rearranging (3.13), yielding

$$k_z = \pm\sqrt{\frac{\omega^2}{\hat{c}^2} - k_x^2}\;. \tag{3.18}$$

There are two possible solutions for k_z, with opposite signs. However, since all sources are located in the half-space $z > Z$, all recorded waves are moving in the negative z direction. With the sign convention established in Section 3.5.1, this corresponds to ω and k_z having opposite signs, and thus the solution for k_z is given by

$$k_z(\omega,k_x) = -\mathrm{sgn}(\omega)\cdot\sqrt{\frac{\omega^2}{\hat{c}^2} - k_x^2}\;. \tag{3.19}$$

Note that if all sources are *not* confined to a half-space on one side of the measurement surface, it is necessary to measure both the sound pressure p and its normal derivative $\frac{\partial p}{\partial z}$ to perform wave field extrapolation [Margrave, 2003]. Both solutions for k_z in (3.18) are then used.

3.5.3 Phase shift migration

We obtain an expression for the extrapolated wave field in time-space coordinates by inserting (3.17) into (3.15):

$$p(t, x, z) = \iint_{-\infty}^{\infty} P(\omega, k_x, Z) \cdot e^{ik_z(z-Z)} \cdot e^{ik_x x} e^{-i\omega t} \, \mathrm{d}k_x \, \mathrm{d}\omega. \tag{3.20}$$

As in Section 3.4 we apply the imaging condition $t = 0$ to obtain a focused image $i_p(x, z)$ from the extrapolated wave field. Since $e^{-i\omega \cdot 0} = 1$, the inverse Fourier transform from ω to t is reduced to a simple integration over ω:

$$i_p(x, z) = \iint_{-\infty}^{\infty} P(\omega, k_x, Z) \cdot e^{ik_z(z-Z)} \cdot e^{ik_x x} \, \mathrm{d}k_x \, \mathrm{d}\omega. \tag{3.21}$$

Equation 3.21 produces a focused image line corresponding to the depth z. A focused 2D image can be made by applying (3.21) for every depth of interest.

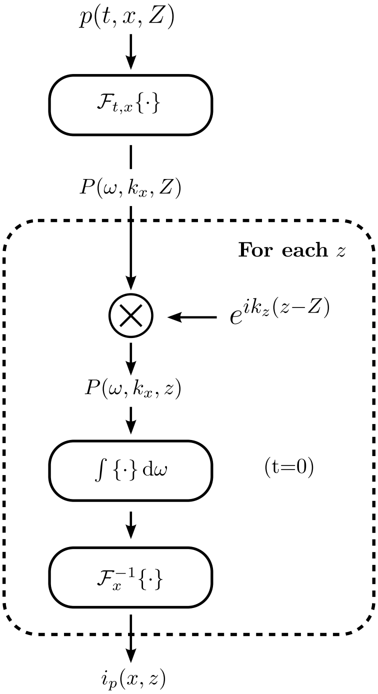

Figure 3.9: Flowchart for PSM algorithm. The recorded wave field is first Fourier transformed, and for every depth z of interest, the wave field is extrapolated to z, integrated over ω, and inverse Fourier transformed, producing a focused image line $i_p(x, z)$.

This approach, termed Phase Shift Migration (PSM), was first introduced by J. Gazdag in 1978 [Gazdag, 1978], for focusing of seismic data. A flowchart for the PSM algorithm is shown in Fig. 3.9.

Note that in practical implementation, calculation of the complex exponential $e^{ik_z(z-Z)}$ for every z value can be very time consuming. A more efficient approach is to calculate the exponential for a small shift in z, and apply it recursively to extrapolate the wave field step by step. In this way, only one complex exponential has to be calculated. The approach is further described in [Olofsson et al., 2010], and is applied in the PSM algorithm implementations used in this thesis.

3.5.4 Stolt migration

Equation 3.21 is very similar to an inverse Fourier transform of $P(\omega, k_x, Z)$, but it has an $e^{ik_z(z-Z)}$ kernel rather than an $e^{-i\omega t}$ kernel. The integral can be recast into a proper inverse Fourier transform by a change of integration variable from ω to k_z [Stolt, 1978].

We obtain an expression for ω by using the relation given in (3.13), and assuming, as in Section 3.5.2, that ω and k_z have opposite signs, so that

$$\omega(k_z, k_x) = -\mathrm{sgn}(k_z) \cdot \hat{c} \cdot \sqrt{k_x^2 + k_z^2}. \tag{3.22}$$

By substituting (3.22) into (3.21), and setting $z = Z + \Delta z$, we get

$$i_p(x, Z+\Delta z) = \iint_{-\infty}^{\infty} P(k_z, k_x, Z)\ e^{ik_z \Delta z} e^{ik_x x}\ dk_x dk_z, \tag{3.23}$$

where

$$P(k_z, k_x, Z) = A(k_z, k_x) \cdot P\big(\omega(k_x, k_z), k_x, Z\big), \tag{3.24}$$

and

$$A(k_z, k_x) = \frac{\partial \omega(k_z, k_x)}{\partial k_z} = \frac{\hat{c}}{\sqrt{1 + \frac{k_x^2}{k_z^2}}}. \tag{3.25}$$

The right side of (3.23) is in the form of a regular inverse Fourier transform. Thus, a complete two-dimensional focused image $i_p(z, Z+\Delta z)$ can be obtained in a single operation, through inverse Fourier transform of the wave field $P(k_z, k_x, Z)$. From (3.24), we see that relative to the original wave field $P(\omega, k_x, Z)$, the substitution of variables leads to a multiplication with an amplitude factor $A(k_z, k_x)$ and a remapping to new ω coordinates. Note that the substitution requires that the effective wave velocity $\hat{c}$ is constant.

In practice, the $P(\omega, k_x, Z)$ wave field is discretely sampled in both time and space, and the new ω coordinates given by (3.22) may not match the equispaced grid of original sampled ω coordinates, as shown in Fig. 3.10. Thus, Stolt migration requires a resampling of the complex Fourier domain wave field. The accuracy of the interpolation method used for this resampling determines

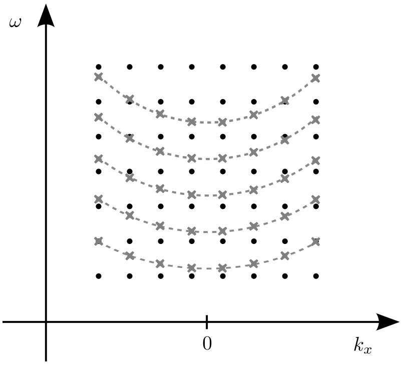

Figure 3.10: Resampling of $(\omega - k_x)$ spectrum for Stolt migration. Original $\omega - k_x$ coordinates shown as black dots, new coordinates shown as gray crosses.

the quality of the focused image, since interpolation errors introduce artifacts in the image. If some low-amplitude artifacts can be tolerated, Stolt migration is generally very efficient [Margrave, 2003]. A flow chart showing the individual steps of the Stolt migration algorithm is given in Fig. 3.11.

3.6 Lateral resolution and spatial sampling criteria

3.6.1 Lateral resolution

Consider the measurement geometry shown in Fig. 3.12. A transducer located in (x', Z) emits a wave which is backscatterered by a reflector in (x, z). The distance between the two is given by $r = \sqrt{(x - x')^2 + (z - Z)^2}$, and thus the phase of the backscattered signal is given by

$$\begin{aligned} \xi(x', x, z) &= \omega \cdot 2r/c \\ &= \frac{4\pi}{\lambda}\sqrt{(x - x')^2 + (z - Z)^2} \ , \end{aligned} \tag{3.26}$$

where in the last transition we have used that $\omega/c = 2\pi/\lambda$. Note that we use the real wave velocity c here, and not the effective velocity $\hat{c}$. The k_x wavenumber is found by calculating the derivative of the phase with regard to

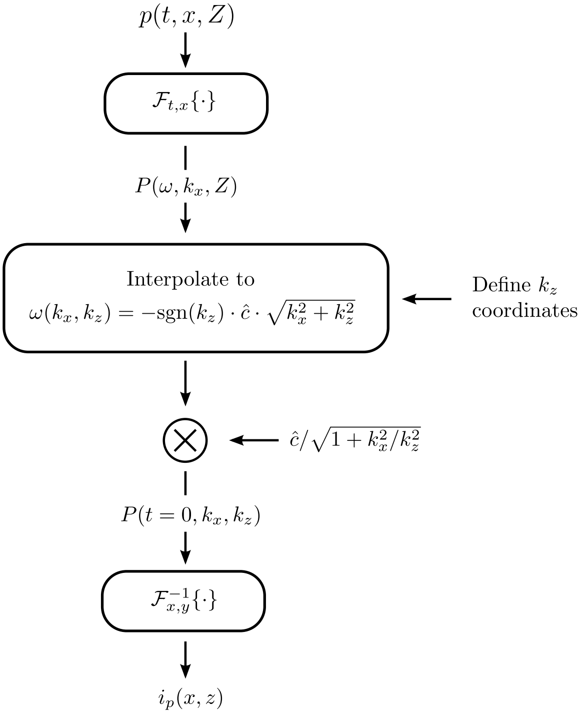

Figure 3.11: Flowchart for the Stolt migration algorithm. The recorded wave field is first Fourier transformed, and then resampled to a new set of ω coordinates, given by the k_z coordinates defined for the image. The resampled wave field is multiplied with an amplitude factor and inverse Fourier transformed, yielding a focused 2D image $i_p(x, z)$.

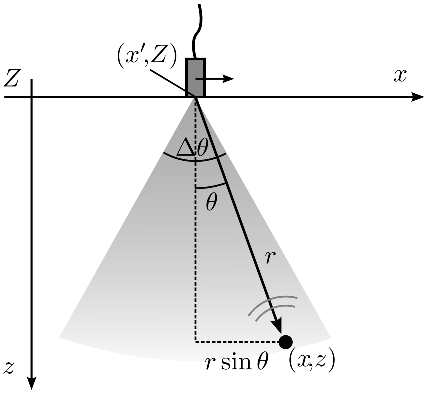

Figure 3.12: Measurement geometry for linear scan of point scatterer.

the transducer x' coordinate:

$$\begin{aligned} k_x = \frac{\partial \xi}{\partial x'} &= \frac{4\pi}{\lambda} \cdot \frac{x - x'}{\sqrt{(x-x')^2 + (z-Z)^2}} \\ &= \frac{4\pi}{\lambda} \cdot \frac{x - x'}{r} \\ &= \frac{4\pi}{\lambda} \cdot \sin\theta. \end{aligned} \tag{3.27}$$

The range of k_x values, denoted Δk_x, is thus determined by the transducer beamwidth, $\Delta\theta$. Note that this makes Δk_x independent of depth z. In Section 2.4.4 it was shown that for a planar, uniformly excited source of diameter D, the beamwidth is $\Delta\theta \approx \lambda/D$. Inserting this into (3.27), and using the small terms approximation $\sin\theta \approx \theta$, we get that

$$\begin{aligned} \Delta k_x &\approx \frac{4\pi}{\lambda} \cdot \Delta\theta \\ &\approx \frac{4\pi}{\lambda} \cdot \frac{\lambda}{D} = \frac{4\pi}{D}, \end{aligned} \tag{3.28}$$

yielding a theoretical resolution along the x axis of

$$\delta x \approx \frac{2\pi}{\Delta k_x} \approx \frac{D}{2}. \tag{3.29}$$

3.6.2 Spatial sampling criteria

According to the spatial sampling theorem, the spacing δx_s between measurement positions x' should fulfill the requirement $\delta x_s < 2\pi/\Delta k_x$ [Goodman, 1996, Sec. 2.4]. Again using the relationship in (3.28), we find that this corresponds to $\delta x_s < D/2$. However, in the derivation of Δk_x in the previous section we did not take the full transducer directivity function into account. The jinc directivity function given in (2.7) is non-zero outside the -6 dB beamwidth $\Delta\theta \approx \lambda/D$, and sampling at $\delta x_s < D/2$ may result in aliasing in the focused image. In practice, a spatial sampling interval of $\delta x_s < D/4$ is recommended to avoid any significant aliasing effects [Gough and Hawkins, 1997; Callow, 2003].

3.7 Experiment: Point scatterer in water

An experiment was performed to demonstrate the application of synthetic aperture focusing on real data. A linear scan of a 1.5-mm steel wire was performed using a transducer with 2.25 MHz center frequency and 6 mm diameter. The scan was performed perpendicular to the wire, with a spatial sampling interval of $\delta x_s = 0.5$ mm, and a temporal sampling frequency of 25 MHz. The raw data envelope for the wire target is shown in Fig. 3.13.

The raw data was processed with both the DAS algorithm and the PSM algorithm. The Stolt migration algorithm was not included, since its results

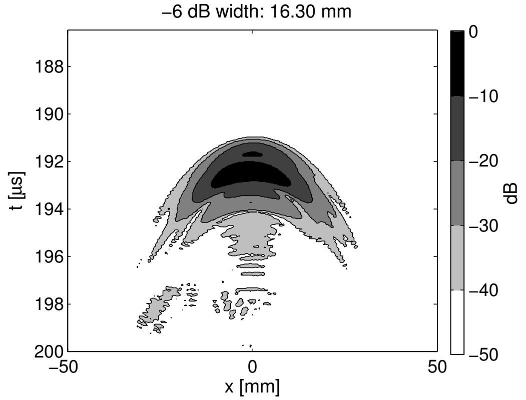

Figure 3.13: Raw data envelope from scan of wire target in water.

are identical to those of PSM when perfect interpolation is applied. Before processing with the DAS algorithm, the data set was upsampled from 12.5 to 200 MHz along the t axis, using zero-filling and low-pass filtering with a FIR filter of 321 elements. Such oversampling enables the use of nearest-neighbour interpolation without introducing large errors, as discussed in Section 3.4.3. Two different apodization functions were used; a rectangular function and a Hann function. Both functions were applied in narrow and wide versions, corresponding to the -20 and -40 dB width of the raw data response. The apodization functions and the corresponding focused images are shown in Fig. 3.14.

With the narrow rectangular apodization, the point target is well focused, with a -6 dB width of 2.92 mm. However, there are wide sidelobes present on each side of the point response. In comparison, the wide rectangular apodization yields a -6 dB width of 2.72 mm, slightly smaller than for the narrow apodization. The shape of the sidelobes is also changed; the lobes are further away from the point response, and have a slightly reduced amplitude.

Comparing these images with the images focused with Hann apodization, it is seen that Hann apodization reduces the sidelobes to the point that they are no longer visible in the displayed dynamic range. However, the -6 dB widths are slightly larger with Hann apodization. This effect is common for all non-uniform apodization windows; there is a trade-off between the sidelobe amplitudes and the width of the main lobe. [Martinez et al., 1999].

Figure 3.15 shows the focused image produced by the PSM algorithm. The -6 dB width of the point target is 2.70 mm, which is approximately the same as for the DAS processing with the wide rectangular apodization. However, similarly to the DAS images with Hann apodization, there are no visible sidelobes. Thus, PSM processing appears to yield the high resolution of DAS with rectangular apodization, but with a lower sidelobe level.

To compare DAS and PSM further, amplitude profile plots were made for

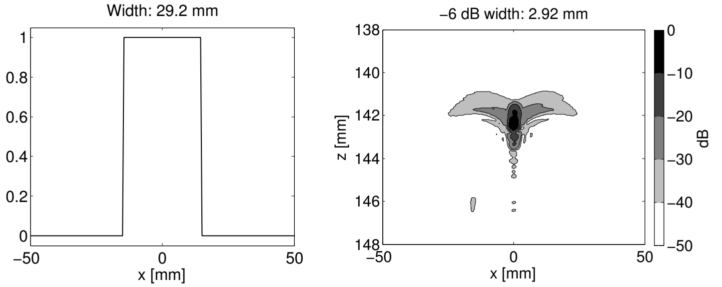

(a) Narrow rect. apodization (b) PSF, narrow rect. apodization

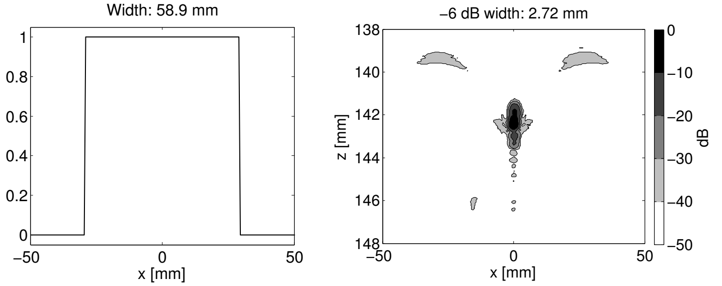

(c) Wide rect. apodization (d) PSF, wide rect. apodization

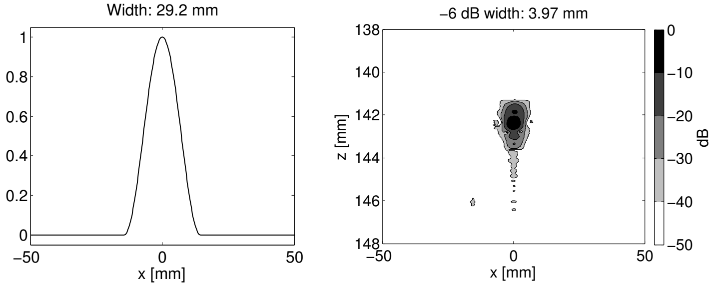

(e) Narrow Hann apodization (f) PSF, narrow Hann apodization

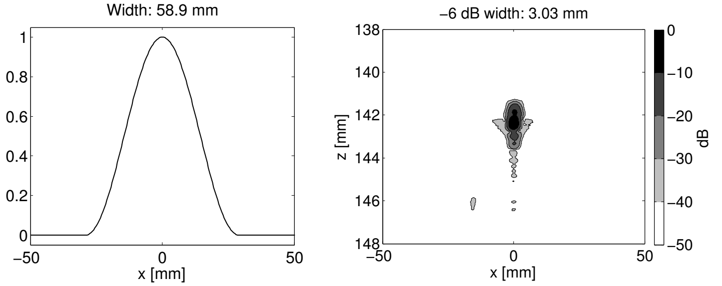

(g) Wide Hann apodization (h) PSF, wide Hann apodization

Figure 3.14: Apodization functions and focused images for DAS processing of data from wire target.

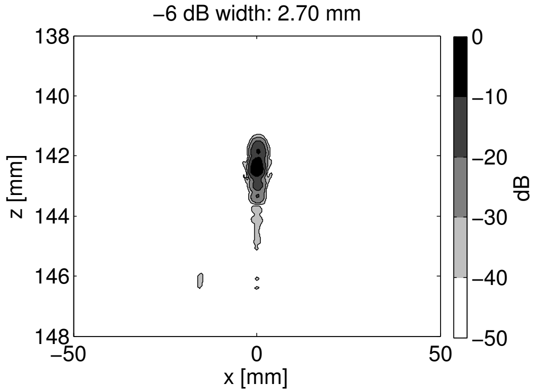

Figure 3.15: Focused image for PSM processing of data from wire target.

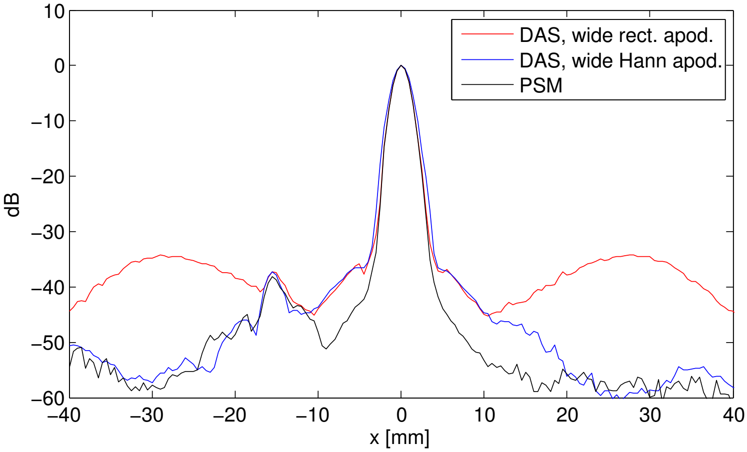

Figure 3.16: Comparison of maximum amplitude profile plots made from the DAS images shown in Fig. 3.14(d) and 3.14(h), and from the PSM image shown in Fig. 3.15.

the DAS images with wide apodization, as well as for the PSM image. The profile plots were made by detecting the maximum amplitude of the focused image in each x position. The results, plotted in Fig. 3.16, clearly indicate the high-amplitude sidelobes produced by DAS with rectangular apodization. Note also that close to the main lobe, PSM has lower sidelobes than both DAS images. The low-amplitude peak seen at x = -15 mm is due to an additional reflection received in the experiment, and is not related to the main point spread function.

This simple experiment shows that there are some small differences in image quality between DAS and PSM, and that these depend on the choice of apodization for the DAS algorithm. Note that it is possible to apply apodization in Fourier-domain algorithms like PSM and Stolt migration by low-pass filtering the k_x spectrum [Cumming and Wong, 2004], but since the sidelobe levels of these algorithms are relatively low even without apodization, we have not included apodization in the algorithm descriptions.

Differences between delay-and-sum focusing and Fourier domain focusing have been observed in a number of papers [Stepinski, 2007; Hunter et al., 2008]. Hunter et al. [2008] point out that Fourier domain algorithms like PSM yield an exact backpropagation of the wave field, while the time-domain DAS algorithm is more heuristic in nature. In [Velichko and Wilcox, 2010], an analytical comparison is made between a number of time-domain and frequency-domain algorithms for array imaging, and it is shown that the algorithms differ in how they weight signals from different spatial positions.

A thorough quantitative comparison of time- and Fourier-domain algorithms would require a large number of simulations and experiments, and is outside the scope of this thesis. It is widely accepted within the field of synthetic aperture imaging the image quality of time- and frequency domain algorithms is approximately the same [Ulander et al., 2003], and the choice between the two is usually based on other factors, for example processing time, hardware platform and positional accuracy.

Chapter 4

Imaging in multilayered media

The synthetic aperture algorithms presented in the previous chapter are all based on the assumption of a homogeneous propagating medium with a constant wave velocity. There are, however, several applications for ultrasonic imaging where the medium consists of a number of horizontal layers with different wave velocities. In order to properly focus backscattered echoes from within the layers, synthetic aperture algorithms for multilayered structures need to take the thickness and wave velocity of each layer into account.

Figure 4.1(a) shows the raw data from a multilayer experiment which is further described in Section 4.5. From top to bottom, the imaged region consists of water, acrylic glass and aluminium layers, with four point-like scatterers in each. Figure 4.1(b) shows the image from a single-layer PSM processing of the data, where the wave velocity of water was used for the entire image. The scatterers in the water layer are well focused, but due to the difference in wave velocity, the focusing effect diminishes in the acrylic glass and aluminium layers. Processing the same data set with multilayer synthetic aperture algorithms significantly improves the lateral resolution, as we shall see in this chapter.

In the field of seismic exploration, the interior structure of the Earth is imaged by emitting low-frequency sonic waves into the geological layers, and recording the backscattered echoes. Different types of rock often have different wave velocities, and the wave velocity generally increases with depth. In general, the velocity is a function of the position in three-dimensional space, but in practice it is often assumed to vary with depth only, $c(z)$ [Claerbout, 2010]. Such a model is also suitable for describing the multilayered structures we consider here.

Versions of the DAS algorithm are often used for processing of seismic data, where the delay-and-sum operations are often referred to as Normal Moveout Correction (NMO) and Common Depth Point Stack (CDP Stack) [Wood and Treitel, 1975]. The DAS algorithm can be modified to handle $c(z)$ velocity variations, based on the concept of root-mean-square velocity, and in this chapter we describe the modified algorithm for the case of multilayered media.

In the PSM algorithm, the wave field is extrapolated from one depth to another by multiplication with a complex exponential, $\exp\big(ik_z\Delta z\big)$, where k_z is a function of wave velocity. k_z be recalculated to accommodate changes in wave velocity as the wave field is extrapolated, and thus PSM is valid for any velocity function $c(z)$. The application of PSM for ultrasonic imaging in multilayered media was introduced first in [Olofsson, 2010], and is explained further in this chapter.

Due to its high efficiency, the Stolt migration algorithm is attractive for multilayer imaging as well as single-layer imaging, but the substitution of variables in the algorithm requires that the wave velocity is constant. The Stolt migration algorithm is therefore not applicable for data which spans more than one layer. However, as we show in this chapter, the PSM algorithm can be used to extrapolate the measurements from one layer to the next, leaving imaging within each layer to the Stolt algorithm. This approach was first introduced for seismic imaging in [Kim et al., 1989], and is adapted here for ultrasonic imaging.

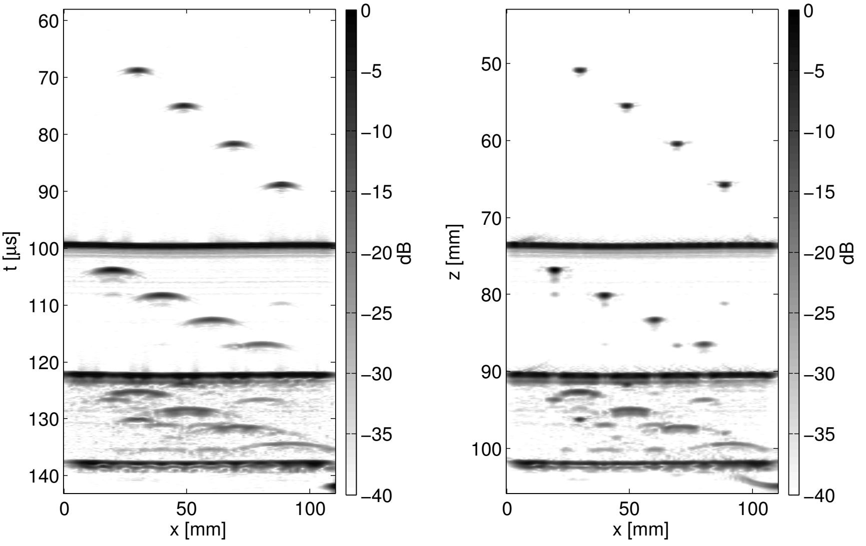

(a) Raw data

(b) Focused image

Figure 4.1: Comparison of raw data and image produced by single-layer PSM processing. The image was focused using the wave velocity of water for the entire image.

4.1 Multilayer delay-and-sum

4.1.1 RMS velocity

Consider first the single-layer geometry shown in Fig. 4.2(a). The transducer position is denoted (x', Z), and the scatterer position is denoted (x, z). In Section 3.4.1, it was shown that in the DAS algorithm, the pulse-echo wave field is integrated along curves corresponding to the two-way delay time t between the transducer and the scatterer. For a single layer geometry with wave velocity c, the delay time is given by

$$t(x - x', z) = \frac{2}{c}\sqrt{(x - x')^2 + (z - Z)^2}. \tag{4.1}$$

Now, consider the multilayered geometry shown in Fig. 4.2(b). The layers are numbered $1, 2, \ldots, L$, and the thickness and wave velocity of layer l is denoted with d_l and c_l, respectively. The transducer is scanned along the top of layer 1, denoted Z_1. The different sound velocities give rise to reflection and refraction at the layer interfaces, making the path of the wave irregular. Given the incident angle of a wave at an interface, the angle of the refracted wave can be calculated using Snell's law. However, given the position of the transducer and the scatterer, it is not possible to calculate the exact wave path between the two analytically [Schneider, 1984; Margrave, 2003]. Numerical ray tracing methods can be employed [Johnson and Barna, 1983; Kraus, 1983; Margrave, 2003; Shlivinski and Langenberg, 2007], but in practical applications these are often slow and complicated to implement. Here we will employ an approximate solution which is often used in processing of seismic data [Schneider, 1984; Schultz, 1984]. The solution is based on the concept of root-mean-square (RMS) velocity.

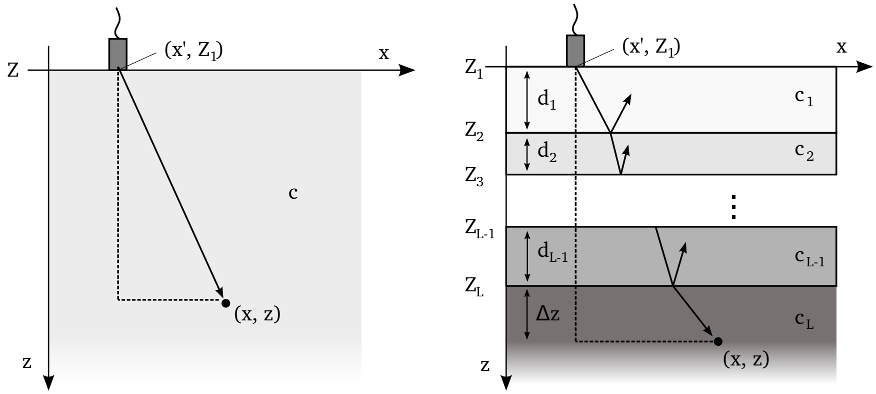

(a) Single layer (b) Multilayer

Figure 4.2: Measurement geometry for homogeneous and multilayered media.

The wave velocity c is assumed to be a function of depth, $c(z)$. The one-way travel time for a pulse following a vertical path from Z to z, termed the normal incidence travel time, is then given by

$$\tau(z) = \int_{Z}^{z} \frac{1}{c(\tilde{z})} \mathrm{d}\tilde{z}. \tag{4.2}$$

In the layered geometry shown in Fig. 4.2(b), the integral in (4.2) is reduced to a sum,

$$\tau(z) = \left(\sum_{l=1}^{L-1} \frac{d_l}{c_l} \right) + \frac{\Delta z}{c_L}. \tag{4.3}$$

There is a monotonous relationship between z and τ, and thus the wave velocity can also be expressed as a function of τ, $c(\tau)$. The RMS velocity is the root-mean-square velocity with respect to τ,

$$c_{\mathrm{rms}} = \sqrt{\frac{1}{\tau} \int_{0}^{\tau} c^2(\tilde{\tau})\ \mathrm{d}\tilde{\tau}}, \tag{4.4}$$

which for the layered geometry can be rewritten as

$$c_{\mathrm{rms}}(z) = \sqrt{\frac{\sum\limits_{l=1}^{L-1} c_l d_l + c_L \Delta z}{\tau(z)}}\ . \tag{4.5}$$

The one-way delay time between a transducer and a scatterer in a multilayered geometry can be expressed as a Taylor series,

$$t^2(x - x', z) = \tau^2(z) + a_2(x{-}x')^2 + a_4(x{-}x')^4 + \dots, \tag{4.6}$$

where only even terms are included due to symmetry. It can be shown [Schneider, 1984] that a_2, the coefficient for the quadratic term, is equal to $1/c^2_{\mathrm{rms}}(z)$. Omitting all higher order terms, we obtain an expression for the travel time which is approximate but accurate for small offsets $(x - x')$:

$$t_{\mathrm{rms}}(x - x', z) = 2 \cdot \sqrt{\tau^2(z) + \frac{(x - x')^2}{c^2_{\mathrm{rms}}(z)}}\ . \tag{4.7}$$

4.1.2 Multilayer DAS

Equation (4.7) enables the formulation of a DAS algorithm for multilayered media which is very similar to the single-layer algorithm described in Section

3.4.1. Let $s(t, x')$ denote the backscattered signal recorded in the transducer position x'. The focused image pixel $i_p(x, z)$ is then given by

$$i_p(x,z) = \int \alpha(\hat{x}) \cdot s\big(t_{\text{rms}}(x - x', z), x'\big)\mathrm{d}x', \tag{4.8}$$

where $\alpha(\hat{x})$ denotes general apodization weights. We will refer to this algorithm as Multi-Layer Delay-And-Sum (MLDAS).

The normalized x coordinate used for the apodization weights is given by $\hat{x} = (x - x')/\Delta x(z)$, where $\Delta x(z)$ denotes the transducer beamwidth, as discussed in Section 3.4.2. In a multilayered geometry, the refraction at each interface changes the shape of the transducer beam, as illustrated in Fig. 4.3. If the beamwidth in the first layer is given by $\Delta\theta$, the angle of the beam edge in layer l is given by

$$\theta_l = \sin^{-1}\left(\frac{c_l}{c_1} \cdot \sin(\Delta\theta/2)\right), \tag{4.9}$$

and the beamwidth Δx at depth z is given by

$$\Delta x(z) = 2 \cdot \left(\sum_{i=1}^{l-1} d_l \cdot \tan(\theta_l) + \Delta z \cdot \tan(\theta_l)\right). \tag{4.10}$$

In the implementation of the MLDAS algorithm in this thesis we employ the Hann apodization function given in (3.9).

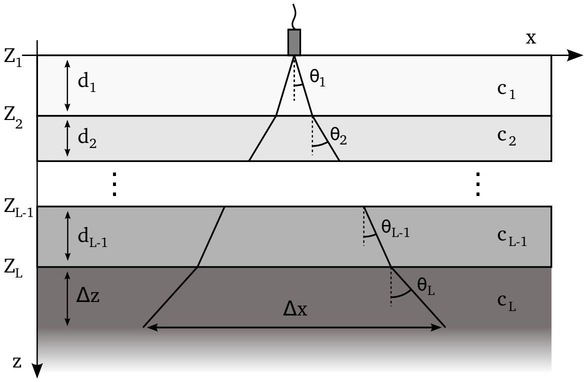

Figure 4.3: Transducer beam shape in multilayered geometry. The divergence of the beam changes from layer to layer due to refraction at the layer interfaces.

4.2 Multilayer Fourier-domain imaging

4.2.1 Multilayer phase shift migration

We assume the same multilayer geometry as in the preceding section, with layers numbered $l = 1, 2, ..., L$, and d_l and c_l denoting the thickness and wave velocity of layer l, respectively. The top of the uppermost layer is denoted by Z_1, and the interfaces between the layers are denoted by Z_l, so that the top of layer l is given by $Z_l = Z_1 + \sum_{m=1}^{l-1} d_m$.

We know from Section 3.5.2 that in a medium with constant sound speed, the wave field at an arbitrary depth z, $P(\omega, k_x, z)$, can be calculated by multiplying a reference wave field $P(\omega, k_x, Z)$ with a phase factor $e^{ik_z(z-Z)}$. In the multilayer case, the field cannot be extrapolated through several layers directly, since k_z is a function of the medium velocity c_l,

$$k_{zl} = -\operatorname{sgn}(\omega) \cdot \sqrt{\frac{\omega^2}{\hat{c}_l^2} - k_x^2}, \tag{4.11}$$

where the layer dependence is indicated by index l. However, extrapolation within each layer is still possible,

$$P(\omega, k_x, Z_l + \Delta z) = P(\omega, k_x, Z_l) \cdot e^{ik_{zl}\Delta z}, \quad \text{if } \Delta z < d_l, \tag{4.12}$$

where $P(\omega, k_x, Z_l)$ denotes the field at interface Z_l, and $P(\omega, k_x, Z_l + \Delta z)$ denotes the field at depth $z = Z_l + \Delta z$.

If the wave field is to be extrapolated through more than one layer, the transmission through the layer interfaces has to be considered. The transmission factor between different media is generally a complex function, dependent on both incident angle and the acoustic impedances of the media [Brekhovskikh and Godin, 1990]. However, for most commonly available ultrasound transducers, the directivity of the transducer limits the emitted and received wave fields to a relatively small angle interval. We will therefore assume that the transmission factors are approximately independent of incident angle, so that the wave fields directly above and directly below an interface are proportional;

$$P(\omega, k_x, Z_l^-) \propto P(\omega, k_x, Z_l^+), \tag{4.13}$$

where the plus and minus signs are used to indicate the upper and lower side of the interface, respectively. Since we are mainly interested in relative amplitudes within each layer, the amplitude scaling effect imposed by the interfaces is here deemed unimportant to the imaging problem.

Assuming proportionality across interfaces, the wave field at an arbitrary interface Z_l can, within a scaling factor, be calculated from the wave field measured at Z_1,

$$P(\omega, k_x, Z_l) \propto P(\omega, k_x, Z_1) \cdot \exp\left(i \sum_{m=1}^{l-1} k_{zm} d_m \right). \tag{4.14}$$

The equations (4.12) and (4.14) constitute the basis for PSM imaging of several layers. The imaging procedure for layer l can be summarized as follows:

1. Calculate the wave field at the top of the layer interface, $P(\omega, k_x, Z_l)$, using (4.14)
2. For each depth $Z_l + \Delta z$ to be imaged within the layer:
   (a) Shift the wave field downwards with Δz by multiplying with a phase factor, according to (4.12), to obtain $P(\omega, k_x, Z_l + \Delta z)$
   (b) Create an image line $i_p(x, Z_l + \Delta z)$ by integrating with regard to ω and inverse transforming with regard to k_x, similarly to (3.21).

4.2.2 Multilayer Stolt migration

In Section 3.5.4, it was shown that Stolt migration enables focusing of the complete pulse-echo wave field in a single operation, through a substitution of variables. The substitution requires that the wave velocity is constant, and Stolt migration can therefore only be performed inside a single layer. Thus, to use Stolt migration in layer l, the wave field must first be extrapolated to the interface Z_l using (4.14). The focused image for layer l is then given by

$$i_{p,l}(x, \Delta z) = \iint_{-\infty}^{\infty} \underbrace{A_l(k_x, k_z) \cdot P(\omega_l(k_x, k_z), k_x, Z_l)}_{P(k_x, k_z, Z_l)} \cdot e^{ik_z \Delta z} e^{ik_x x} \, \mathrm{d}k_x \mathrm{d}k_z, \quad (4.15)$$

where

$$A_l(k_x, k_z) = \frac{\hat{c}_l}{\sqrt{1 + \frac{k_x^2}{k_z^2}}} \text{ , and} \quad (4.16)$$

$$\omega_l(k_x, k_z) = -\mathrm{sgn}(k_z) \cdot \hat{c}_l \sqrt{k_x^2 + k_z^2}. \quad (4.17)$$

The imaging procedure to create an image of layer l can be summarized in the following way:

1. Calculate the wave field at the top of the layer, $P(\omega, k_x, Z_l)$, using (4.14)
2. Use (4.16) and (4.17) to obtain the remapped wave field $P(k_x, k_z, Z_l)$.
3. Inverse transform to obtain the image within the layer, $i_{p,l}(x, \Delta z)$, given by (4.15)

We will refer to this algorithm as the MUlti-Layer Omega-K algorithm (MULOK). The term *Omega-K* is used rather than Stolt migration because it is more common in radar literature [Cumming and Wong, 2004].

As for many engineering problems, the mathematics of the PSM and MULOK algorithms conceal the complexity of practical implementation. Further implementation details are given in Appendix 4.A.

4.3 Lateral resolution in multilayered media

In Section 3.6.1 it was shown that the lateral resolution of an synthetic aperture image is dependent on the bandwidth of the k_x spectrum, and that the bandwidth is limited by the effective length D of the transducer, so that the lateral resolution is approximately $D/2$. But is this also true for the multilayer case?

According to Snell's law, the k_x wavenumber of a wave incident on a layer interface must remain the same after transmission into the next medium. Thus, the refraction of the wave does not in itself alter the horizontal wavenumber, but the transmission factors between media are generally dependent on incidence angle, making the interface a low-pass filter for the k_x spectrum [Brekhovskikh and Godin, 1990]. Above the *critical angle* of the interface, the incident wave is totally reflected. The bandwidth of the k_x spectrum is only maintained as long as the transmission factors are approximately uniform within the divergence angle of the transducer. In practice, this requirement is fulfilled for many transducer designs and material combinations of interest. For example, for a immersion scan of copper using a 2.25 MHz 10 mm diameter transducer, the two-way transmission factor varies by only approximately 6% within the transducer beam [Olofsson, 2010]. As long as the k_x spectrum bandwidth can be assumed to be the same for the single-layer and multilayer case, the theoretical lateral resolution of $D/2$ is also the same.

4.4 Algorithm efficiency

4.4.1 Asymptotic complexity

The efficiency of an algorithm is often quantified by analyzing how the number of operations grow as the size of the input data tends towards infinity, and this asymptotic complexity is denoted using "Big O" notation. In the case of the PSM and MULOK algorithms, the size of the input data is given by the number of time samples, N, the number of measurement positions, M, and the number of layers, L. Note that the sampling frequency is assumed to be constant, so that the number of frequency samples within the transducer bandwidth is proportional to the number of time samples.

In the MLDAS algorithm, each image pixel is formed by delaying and summing the signals recorded within the synthetic aperture. In general, the effective size of the synthetic aperture increases with depth, as shown in Section 4.1.2, but to simplify the analysis we will assume that the synthetic aperture size is constant within the imaged range.

The delay operation requires an interpolation step, as discussed in Section 3.4.3. As long as the synthetic aperture size is constant, the number of operations needed for interpolation and summation for each image pixel is also constant. Thus, since there are NM pixels in the image, the MLDAS algorithm is $O(NM)$ for a synthetic aperture of constant size. Note however

Table 4.1: Complexity for the individual steps of the PSM algorithm

Operation	Complexity
Initial Fourier transform	$O\big(MN\log MN\big)$
Phase shift to Z_l	$O(LMN)$
Phase shift to $Z_l + \Delta z_l$	$O(MN^2)$
Summation over ω	$O(MN^2)$
Inverse transform (k_x)	$O(MN\log M)$

Table 4.2: Complexity of the individual steps of the MULOK algorithm

Operation	Complexity
Initial Fourier transform	$O\big(MN\log MN\big)$
Phase shift to Z_l	$O(LMN)$
Interpolation from ω to k_z	$O(LMN\log N)$
Amplitude scaling	$O(LMN)$
Inverse Fourier transform	$O\big(LMN\cdot\log MN\big)$

that in similar analyses, for example in [Nagai, 1985] and [Ulander et al., 2003], it is assumed that all M transducer positions are included in the synthetic aperture, for all pixels in the image. With this assumption, the number of operations needed to focus a single pixel grows with M, and the algorithm is $O(NM^2)$. However, in the following discussion we maintain the assumption that the synthetic aperture size is constant, and that MLDAS is $O(NM)$.

The analysis of the PSM and MLDAS algorithms is slightly more complicated and has therefore been placed in Appendix 4.A.5. A summary of the complexity for each algorithm step is given in Tables 4.1 and 4.2. The overall complexity of each algorithm is given by the algorithm step with the highest order complexity. To analyze this, we consider the complexities with regard to N, M and L separately, assuming that the two remaining variables are kept constant. The highest order complexities are summarized in Table 4.3. MULOK is seen to have a lower complexity than PSM with regard to N, since $N\log N < N^2$, while the complexity with regard to M and L is the same for both algorithms. The MLDAS algorithm has a lower complexity than PSM and MULOK in terms of both N and M, and its processing time is independent of L. However, a large number of operations are involved in forming each pixel, yielding large constant factors not included in the analysis.

Table 4.3: Asymptotic complexities of MLDAS, PSM and MULOK, with respect to N, M and L separately.

Algorithm	N	M	L
MLDAS	$O(N)$	$O(M)$	–
PSM	$O(N^2)$	$O(M\log M)$	$O(L)$
MULOK	$O(N\log N)$	$O(M\log M)$	$O(L)$

4.4.2 Empirical evaluation of execution times

To compare the execution times for practical implementations of the algorithms, a number of simulated processings were performed in Matlab. For convenience, test data sets were made using matrices with random numbers rather than actual ultrasonic scans. This should not affect the execution times of the algorithms, as they are only dependent on the size of the data sets, and not on their content. The number of pixels in the output images was set equal to that of the raw data input. For the MLDAS algorithm, the input data was upsampled before focusing to enable nearest-neighbour interpolation, as discussed in Section 3.4.3. The time required to perform this upsampling is relatively small, and was not included in the execution time measurements. Also, the angular beamwidth used for the MLDAS apodization was set to 13° for all the layers. This beamwidth corresponds approximately to the apodization beamwidth used for a 2.25 MHz transducer with 6 mm diameter in water. The simulations were performed on a dual-core 2 GHz laptop, running a 64-bit Linux version of Matlab R2011b (The Mathworks, Natick, MA, USA).

Two series of simulations were performed, to study the dependence on number of time samples, N, and number of measurement positions, M. In the first series, M was kept constant at 256, and N was varied within the range [64, 8192]. The results are shown in Fig. 4.4(a) and (b), corresponding to simulations with 2 and 5 layers, respectively. Lines indicating the asymptotic complexity with regard to N were added to the results for each algorithm, normalized to match the values for $N = 8192$. In the second experiment series, N was kept constant at 256, and M was varied in the range [64, 8192]. The results are shown in Fig. 4.4(c) and (d), with similar lines as in Fig. 4.4(a) and (b) indicating the asymptotic complexity with regard to M. Note that both axes in the plots are logarithmic.

In general, the results match the asymptotic complexities in Table 4.3 closely, especially for high values of N and M. This indicates that the general trends seen here can be assumed to be valid in general, even if the execution times presented here are valid only for one specific implementation of the algorithms.

In Fig. 4.4(a), it is seen that the PSM algorithm has the lowest processing time for small N, but that its rate of increase is also significantly higher than that of the other algorithms. Thus, even though the processing time for MLDAS is significantly higher than PSM and MULOK for small N, the PSM line crosses the MLDAS line at $N \approx 4096$. However, the MULOK processing time is consistently lower than the MLDAS processing time by a large factor. For $N = 8192$, the processing times are 140 s, 70 s and 3.6 s for PSM, MLDAS and MULOK, respectively.

Fig. 4.4(b) shows how the processing times are affected by changing the number of layers from 2 to 5. The PSM and MLDAS results are practically identical to the 2-layer case in Fig. 4.4(a), but the MULOK processing time is increased for all N. At $N = 8192$, the MULOK processing time is 7.3 s, an

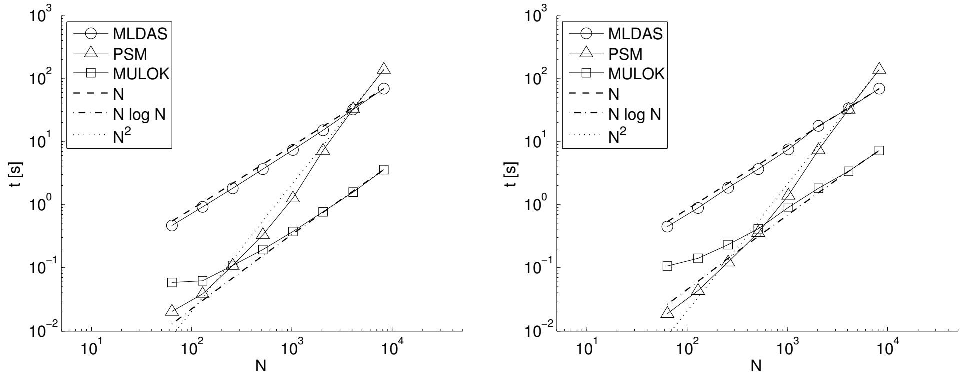

(a) M = 256, L = 2 (b) M = 256, L = 5

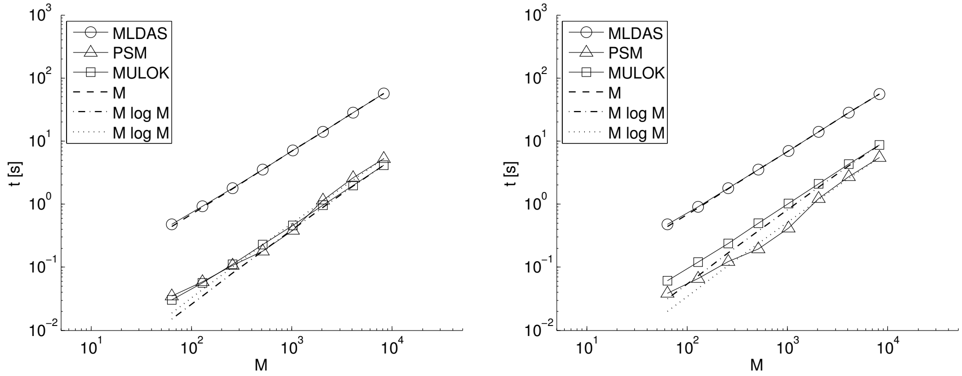

(c) N = 256, L = 2 (d) N = 256, L = 5

Figure 4.4: Comparison of execution times for MLDAS, PSM and MULOK algorithms.

increase from the 2-layer case of approximately 100%.

With N constant and M increasing, the asymptotic rate of increase for the three algorithms is very similar, since the additional $\log M$ factor for PSM and MULOK is relatively small even for large M. This is clearly seen in Fig. 4.4(c), where the MLDAS processing time is consistently higher than the PSM and MULOK processing time for all M. At $M = 8192$, the processing times are 56 s, 5.2 s, and 4.2, for MLDAS, PSM and MULOK, respectively.

Finally, Fig. 4.4(d) is similar to Fig. 4.4(b) in showing that increasing the number of layers also increases the MULOK processing time, while the MLDAS and PSM processing times remain unchanged. The reason that MULOK is more heavily influenced by L than PSM can be found by comparing the complexities for each algorithmic step, listed in Table 4.1 and Table 4.2. PSM has only one step whose complexity is proportional to L, while almost all steps in MULOK are have complexities proportional to L.

4.5 Experiment with three-layer structure

4.5.1 Experimental setup

An experiment was performed to study the imaging performance of the multilayer algorithms for real ultrasound data. Two test blocks with side-drilled holes were placed on top of each other and immersed in a water tank, and an array of four steel pins was placed over the two blocks, as shown in Fig. 4.5. A B-scan of the arrangement was performed using a 2.25 MHz transducer with 6 mm diameter, moved in steps of 1 mm, with a sampling frequency of 12.5 MHz. 1040 time samples were recorded in 111 measurement positions.

The test blocks were made of acrylic glass and aluminium, and were 31 and 50 mm thick, respectively. Each of the blocks had four side-drilled holes, which were all 1.6 mm in diameter and 30 mm deep. The vertical spacing between the holes was 6 mm in the acrylic glass block and 10 mm in the aluminium block, while the horizontal spacing was 20 mm for both blocks. The blocks were also shifted approximately 10 mm horizontally, so that the upper holes would not create a dominating "shadow" for the lower holes. The steel pins were 0.3 mm in diameter, with a vertical spacing of 5 mm and a horizontal spacing of 20

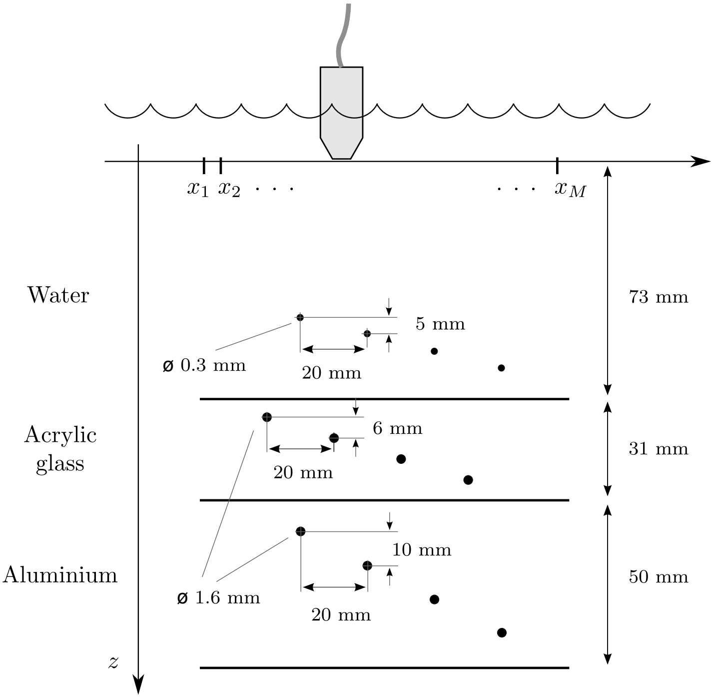

Figure 4.5: Measurement geometry for experiment with point-like scatterers in water, acrylic glass and aluminium layers.

mm.

To compensate for limited dynamic range in the signal acquisition system, a time-dependent damping/amplification was applied during the scan. The reflection from the interface between water and acrylic glass was damped by 10 dB, and the reflections from within the aluminium layer were amplified by 20 dB.

The raw data was processed with both the MLDAS, PSM and MULOK algorithms, assuming a longitudinal wave velocity for water, acrylic glass and aluminium of 1480 m/s, 2730 m/s and 6320 m/s, respectively. In the MLDAS algorithm, a Hann window was applied, as discussed in Section 3.4.2 and 4.1.2. The beamwidth, which determines the size of the synthetic aperture in the MLDAS algorithm, was set to 15.7 degrees, corresponding to 2.5 λ/D at the transducer center frequency. A relatively wide beam was used to maintain a high lateral resolution, as discussed in Section 3.7. Also, for the MLDAS algorithm the raw data was upsampled from 12.5 MHz to 200 MHz to enable accurate nearest-neighbour interpolation, as discussed in Section 3.4.3. The resampling was performed by zero-filling and low-pass filtering with a FIR filter with 321 elements.

4.5.2 Results after synthetic aperture focusing

The raw data envelope image and the focused images are shown in Fig. 4.6, plotted on a dB intensity scale with 40 dB dynamic range.

In the raw image in Fig. 4.6(a), the front echo from the acrylic glass surface is seen as a horizontal line at approximately 100 μs, and echoes from the acrylic glass - aluminium and aluminium - water interfaces are visible at approximately 123 and 137 μs, respectively. Note that due to the difference in wave velocity, the apparent thickness of the layers on the time axis is far from their actual thickness. Reflections from the steel pins and the side-drilled holes are seen as four reflections in each of the layers, with the width of the reflections increasing with depth due to the divergence of the transducer beam. There are also some weaker reflections cluttering the image in both the acrylic glass and aluminium layers, caused by multiple reflections of the scatterers.

It is evident from Fig. 4.6(b)-(d) that the images produced by PSM and MULOK are visually very similar. The reflections from the scatterers have been focused, resulting in an improved lateral resolution that is approximately the same for all scatterers, independent of depth or layer. Multiple reflections have been partially focused or defocused, depending on how close they are in time to their original scatterers. For example, the reflection seen at approximately t = 130 μs, x = 30 mm in the raw data appears to be caused by a scatterer in the aluminium layer, but it is actually a multiple reflection of the leftmost scatterer in the water layer. In the focused images, the reflection has been defocused into a curve. Note also that the scatterers in the aluminium layer seem to have low-amplitude side lobes. These may be caused by so-called “creeping waves” in the side-drilled holes. [Lopez-Sanchez et al., 2005].

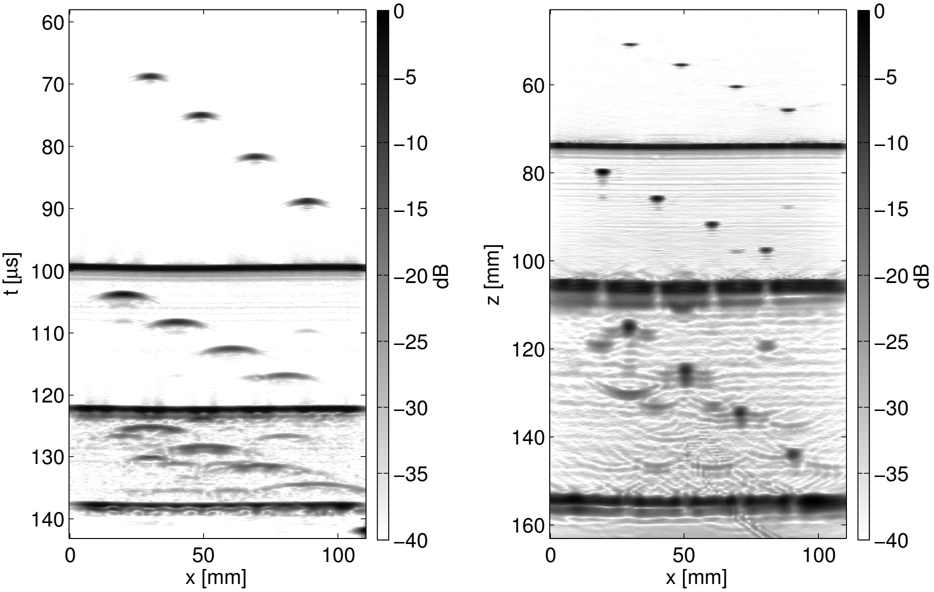

(a) Raw data

(b) Focused image, MLDAS

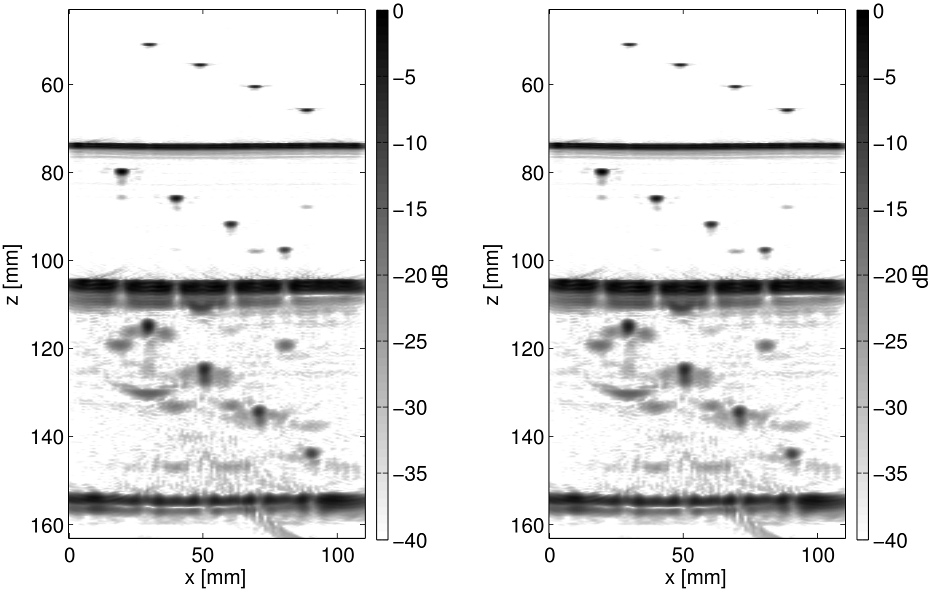

(c) Focused image, PSM

(d) Focused image, MULOK

Figure 4.6: Raw data and focused images from experiment with point-like scatterers in water, acrylic glass and aluminium.

Comparing the MLDAS image to the PSM and MULOK images, it is seen that MLDAS yields a slightly higher level of processing noise. The curved artifacts in the aluminium layer are also more pronounced. To study the differences between the images further, difference images were produced, and the results are shown in Fig. 4.7. The difference was taken between the dB values of the images, corresponding to a power ratio in linear units. The MLDAS-PSM and MLDAS-MULOK difference images were found to be practically identical, and therefore only the MLDAS-PSM image is shown.

The MLDAS-PSM difference image shows the two images are almost identical at the scatterers and interfaces. However, outside these areas the noise floor is higher for the MLDAS algorithm. To further visualize this effect, a single A-scan was extracted from each of the images, from the x position indicated with dashed lines in Fig. 4.7. The A-scans are shown in Fig. 4.8. The plots indicate that in the water and acrylic glass layers, the noise floor in the MLDAS image 10-15 dB higher than in the PSM and MULOK images.

The difference image in Fig. 4.7(b) shows that the differences between the PSM and MULOK images are very small, and mainly located outside the scatterer and interface areas. The differences are probably caused by imperfect interpolation of the $\omega - k_x$ spectrum in the MULOK algorithm.

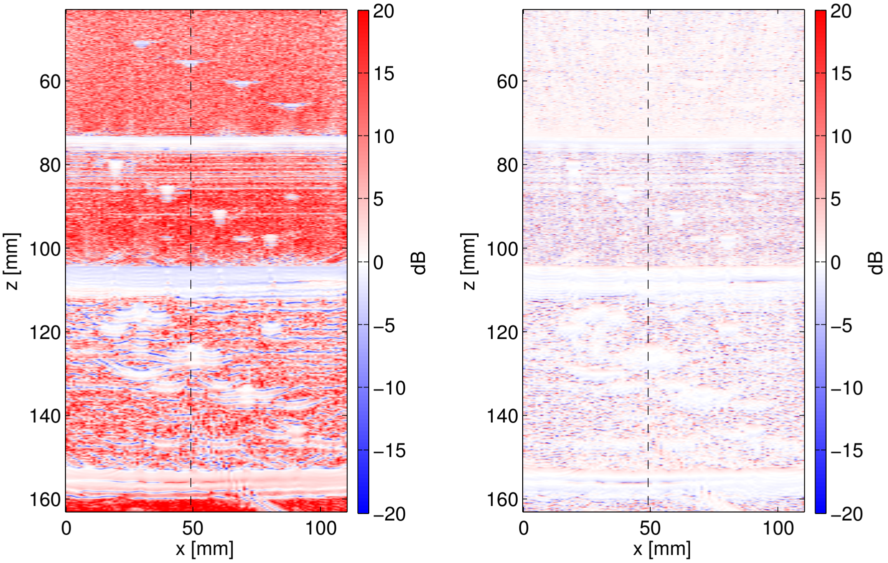

(a) Difference MLDAS-PSM (b) Difference PSM-MULOK

Figure 4.7: Difference images. The dashed line indicates the position of the example A-scan shown in Fig. 4.8.

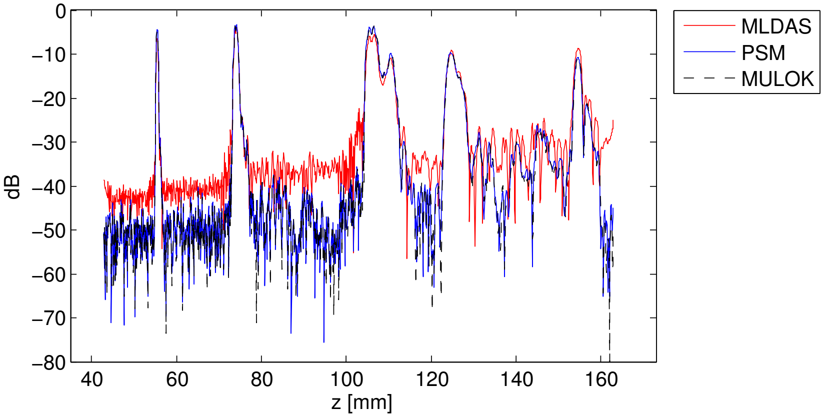

Figure 4.8: Comparison of A-scans from MLDAS, PSM and MULOK images. The amplitude of the reflections from scatterers and interfaces are approximately equal, but the noise floor is slightly higher for MLDAS.

4.5.3 -6 dB width of scatterers

The -6 dB width of the point scatterers was analyzed for both the raw data and the focused images, and the results are shown in Fig. 4.9. In Fig. 4.9(a), we see that in the raw data, the scatterer width increases significantly throughout the layered structure, from approximately 5 mm for the closest scatterer in water, to approximately 24 mm for the deepest scatterer in the aluminium layer. The raw data for the aluminium layer was slightly corrupted by multiple reflections and background noise, as seen in Fig. 4.6(a), and it was therefore hard to determine the -6 dB width accurately. This is probably the reason why the estimated -6 dB width does not increase monotonically with depth in the aluminium layer.

Figure 4.9(b) shows that in the focused images, the -6 dB width is 3-4 mm for all the scatterers, almost independent of depth. This corresponds well with the theoretical resolution of half the transducer diameter, which in this case is 3 mm (see Section 3.6.1). In the aluminium layer, the scatterers are slightly wider than in the other two layers, probably due to the higher level of background noise. Another possible explanation is that the transmission into the aluminium layer slightly decreases the k_x bandwidth, as discussed in Section 4.3.

The MLDAS algorithm is seen to yield -6 dB widths which are slightly higher than those of PSM and MULOK. This may be due to the use of Hann windowing of the synthetic aperture, as demonstrated in Section 3.7. The approximate nature of (4.7), which is used to calculate the pulse-echo delay time in MLDAS, may also affect the resolution of the focused image.

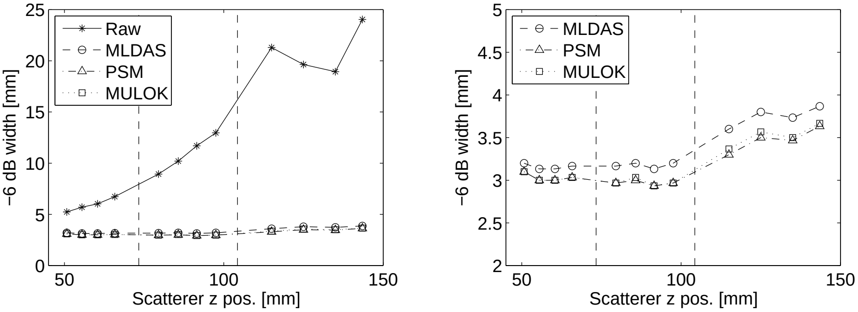

(a) Raw and focused (b) Focused only

Figure 4.9: -6 dB width of scatterers in three-layer structure of water, acrylic glass and aluminium. The interfaces between the layers are indicated with vertical dashed lines.

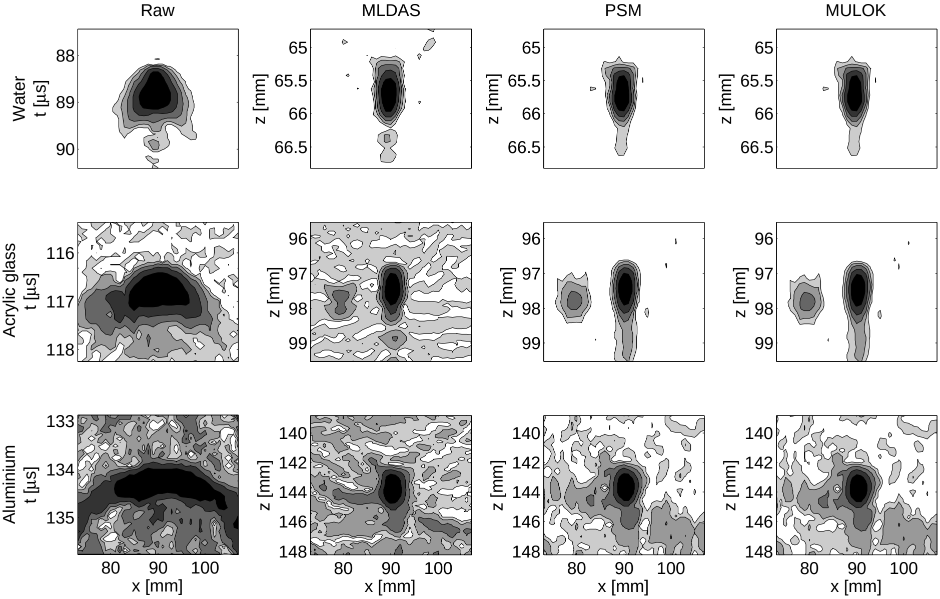

Figure 4.10: Comparison of point spread functions for rightmost scatterer in each layer. Rows, top to bottom: Water, acrylic glass, and aluminium layers. Columns, left to right: Raw data, MLDAS image, PSM image, MULOK image. The amplitude difference between each contour is 6 dB.

4.5.4 Example point spread functions

To study the point spread functions of the raw and focused images in more detail, zoomed-in contour plots of the rightmost scatterer in each layer were made. The plots are shown in Fig. 4.10, with 6 dB difference between each contour. Note that there is a difference in scale between the horizontal and vertical axis.

The plots of the raw data PSF show how the width of the response increases with depth and layer, and that the background noise level increases correspondingly. The focused PSFs are all relatively similar, except for the background noise, which is relatively high in the aluminium layer. Note that the background noise is slightly higher for MLDAS, in both the acrylic glass and the aluminium layer.

4.6 Discussion

In theory, the algorithms presented in this chapter can be applied to structures with an arbitrary number of layers. However, since the transmission factor between layers is generally lower than one, both the transmitted pulse and the backscattered echo will be significantly damped at each interface. Thus, the signal-to-noise ratio is likely to limit the number of layers that can be imaged in practice. In addition, multiple reflections from within the first layers will interfere with echoes from layers further down, as seen in the experiment in Section 4.5.

In Section 4.4.2, the execution times of the MLDAS, PSM and MULOK algorithms were analyzed for simulated data sets of different sizes. The results indicated that the MLDAS algorithm generally has a higher execution time than PSM and MULOK. However, the execution time of the PSM algorithm increases quickly with the number of time samples, N, and thus it is less efficient than MLDAS as N grows large. MULOK, on the other hand, was consistently more efficient than MLDAS for all the simulations. The MULOK execution time increases with the number of layers, L, but due to the issues discussed in the preceding paragraph, the number of layers will probably be limited to two or three. Thus, MULOK should generally yield a lower execution time than MLDAS and PSM. Note, however, that time-domain methods like MLDAS may be simpler to implement than Fourier-domain algorithms on some computational platforms.

Note also that for Fourier-domain methods to make use of the FFT algorithm, the measurement positions are required to be equally spaced along a straight line. Small deviations from the line can be compensated for, but this reduces the efficiency of the algorithm [Ulander et al., 2003]. Time-domain methods do not have the same strict requirements regarding measurement position, and are therefore more easily adapted to applications where the transducer follows an irregular scanning path [Callow, 2003].

The experiment in Section 4.5 demonstrated that all three algorithms yield a significant focusing of data from multilayered structures. The PSM and MULOK algorithms were shown to perform slightly better than MLDAS in terms of signal-to-noise level and lateral resolution. According to the theory presented in Section 3.5 and 4.2, PSM and MULOK should yield identical results, and the small differences observed between the two are probably mainly due to inaccuracies in the resampling of the $\omega-k_x$ spectrum in the MULOK algorithm. In practice, the accuracy of the interpolation used for resampling can be adjusted according to the requirements of the specific application. Note also that there are variations of the $\omega-k$ algorithm which perform resampling without any interpolation, for example using the chirp z-transform [Lanari, 1995]. Modifying MULOK to accommodate such methods is seen as a subject for future work.

In the multilayered geometry considered here, it is assumed that the layers are all horizontal. This assumption is not valid if the layers are tilted relative to the transducer scan line, which may often be the case in practical applications. However, if the tilt is relatively small, the problem can be circumvented by extrapolating the wave field to a line parallel to the layers, yielding a new data set with a rotated coordinate system. This is shown in [Olofsson et al., 2010], and also in Appendix 4.B. The new data set can then be processed by multilayer algorithms without further modifications.

4.7 Summary

In this chapter we have presented three algorithms for 2D multilayer synthetic aperture imaging, called MLDAS, PSM and MULOK. MLDAS is based in the time domain, while PSM and MULOK are based in the Fourier domain. Comparison of execution times revealed that MLDAS is relatively inefficient due to the large number of operations needed to focus each image pixel. PSM is efficient as long as the depth range is relatively small, while MULOK is efficient for both small and large ranges, as long as the number of layers is small. The algorithms were applied to data from an experiment with water, acrylic glass and aluminium layers, and the results showed that the lateral resolution after focusing was approximately the same for all three algorithms. The -6 dB width of point scatterers in the focused images was approximately equal to half the transducer diameter, independent of depth or layer. However, the processing noise level was generally higher for MLDAS than for PSM and MULOK.

4.A Implementation details for PSM and MULOK algorithms

4.A.1 Matrix representation of discrete data

In Section 4.2, the theory for the PSM and MULOK algorithms was outlined for the case of continuous signals, and it was also assumed that the wave field in the measurement plane is known for all x and t. In practice, the wave field must be sampled discretely both in time and space, for a finite time period and over a finite section of the x axis.

We assume that at each measurement position, a pulse is emitted, and N_t time samples are recorded, corresponding to time instants $t_1, t_2, \ldots, t_{N_t}$. The measurement is performed at M different x positions, $x_1, x_2, \ldots, x_M$. Time samples are equally spaced with $\delta t_s = 1/f_s$, where f_s is the sampling frequency, and the x positions are equally spaced with δx_s. Assuming that the measurement is done at depth Z_1, the discrete data set can be organized in a matrix $\boldsymbol{P}_{tx}[Z_1]$, with element p_{ij} corresponding to time instant t_i of the pulse-echo measurement at position x_j:

$$\boldsymbol{P}_{tx}[Z_1] = \begin{array}{c} \\ t_1 \\ t_2 \\ \vdots \\ t_{N_t} \end{array} \begin{array}{c} \begin{array}{cccc} x_1 & x_2 & \ldots & x_M \end{array} \\ \begin{bmatrix} p_{11} & p_{12} & \cdots & p_{1M} \\ p_{21} & p_{22} & & \vdots \\ \vdots & & \ddots & \vdots \\ p_{N_t 1} & \ldots & \ldots & p_{N_t M} \end{bmatrix} \end{array} . \tag{4.18}$$

Note that some zero-padding of $\boldsymbol{P}_{tx}$ in the x direction may be required to avoid spatial aliasing in the focused image [Gu et al., 2004]. Additional zero-padding can be applied to make the dimensions of $\boldsymbol{P}_{tx}$ equal to powers of two, or products of small prime factors, to speed up the FFT algorithm. Assuming that N_t and M includes zero-padding, the discrete Fourier transform of $\boldsymbol{P}_{tx}[Z_1]$ is also an N_t times M matrix, and we denote this matrix $\hat{\boldsymbol{P}}_{\omega k_x}[Z_1]$. The elements of $\hat{\boldsymbol{P}}_{\omega k_x}[Z_1]$ correspond to ω in the range $[-\pi f_s, \pi f_s]$, but only elements that correspond to the transducer passband are significantly different from zero. Because the frequency spectra of real valued signals are symmetric, we can also limit the processing to positive ω values, effectively reducing the size of the data set and speeding up the algorithm. Denoting the upper and lower cutoff frequency for the transducer by $f_{\min}$ and $f_{\max}$, we define $\boldsymbol{P}_{\omega k_x}[Z_1]$ as the subset of $\hat{\boldsymbol{P}}_{\omega k_x}[Z_1]$ corresponding to $\omega \in 2\pi[f_{\min}, f_{\max}]$:

$$\boldsymbol{P}_{\omega k_x}[Z_1] = \begin{array}{c} \\ \omega_1 \\ \omega_2 \\ \vdots \\ \omega_{N_\omega} \end{array} \begin{array}{c} \begin{array}{cccc} k_{x1} & k_{x2} & \ldots & k_{xM} \end{array} \\ \begin{bmatrix} P_{11} & P_{12} & \ldots & P_{1M} \\ P_{21} & P_{22} & & \vdots \\ \vdots & & \ddots & \vdots \\ P_{N_\omega 1} & \ldots & \ldots & P_{N_\omega M} \end{bmatrix} \end{array} , \tag{4.19}$$

where $\omega_1 = 2\pi \left\lfloor N_t \frac{f_{\min}}{f_s} \right\rfloor$, $\omega_{N_\omega} = 2\pi \left\lceil N_t \frac{f_{\max}}{f_s} \right\rceil$, and the step size is $\Delta\omega = 2\pi f_{\mathrm{s}}/N_t$. The relationship between N_ω and N_t is given by the ratio of transducer bandwidth to sampling frequency:

$$N_\omega / N_t \approx (f_{\max} - f_{\min})/f_{\mathrm{s}}. \tag{4.20}$$

Also, assuming that the Fourier transform output is arranged so that the zero wavenumber is centered, and that M is even, the k_x wavenumbers are given by

$$\boldsymbol{k}_x = \frac{2\pi}{\delta x_s \cdot M} \cdot [-M/2, -M/2+1, \cdots, 0, \cdots, M/2-1]\,. \tag{4.21}$$

4.A.2 Wave field extrapolation

We know from Section 4.2.1 that a wave field at depth Z_l can be shifted to an arbitrary depth $Z_l + \Delta z$ within layer l by multiplication with a complex exponential $e^{ik_{zl}\Delta z}$, where k_{zl} is given by

$$k_{zl} = -\mathrm{sgn}(\omega) \cdot \sqrt{\frac{\omega^2}{\hat{c}_l^2} - k_x^2}. \tag{4.22}$$

The frequency-wavenumber spectrum should be limited to propagating waves, corresponding to real-valued k_{zl}, and this requirement is fulfilled as long as the square root argument of (4.22) is positive. All elements of $\boldsymbol{P}_{\omega k_x}$ for which $\frac{\omega^2}{\hat{c}_l^2} - k_x^2 < 0$ should therefore be set to zero.

Let $\boldsymbol{K}_{zl}$ be the discrete matrix representation of k_{zl}. It is an N_ω times M matrix given by

$$\boldsymbol{K}_{zl} = \begin{bmatrix} k_{zl}(\omega_1, k_{x1}) & \dots & k_{zl}(\omega_1, k_{xM}) \\ \vdots & \ddots & \vdots \\ k_{zl}(\omega_{N_\omega}, k_{x1}) & \dots & k_{zl}(\omega_{N_\omega}, k_{xM}) \end{bmatrix}. \tag{4.23}$$

The extrapolation from depth Z_l to depth $Z_l + \Delta z$ is performed with an entrywise multiplication:

$$\boldsymbol{P}_{\omega k_x}[Z_l + \Delta z] = \boldsymbol{P}_{\omega k_x}[Z_l] \circ \exp\left(i\boldsymbol{K}_{zl}\Delta z\right). \tag{4.24}$$

4.A.3 Stolt migration

The Stolt migration algorithm requires a substitution of variables given by (4.15), (4.16) and (4.17). The discrete version of $P(\omega, k_x, Z_l)$, denoted $\boldsymbol{P}_{\omega k_x}[Z_l]$, is computed for a finite, equally spaced set of ω values. Similarly, the discrete version of $P(k_x, k_{zl}, Z_l)$, denoted by $\boldsymbol{P}_{k_z k_x}[Z_l]$, should be computed for an equally spaced set of k_z. However, the mapping given by $\omega_l(k_x, k_{zl})$ does not in general coincide with the equispaced values of ω in $P(\omega, k_x, Z_l)$, and therefore an interpolation step is needed.

Using (4.17), we find that for a given k_{xj}, the ω values to be interpolated for are given by the vector

$$\boldsymbol{\omega}_l^{ip}(j) = \hat{c}_l \cdot \sqrt{k_{xj}^2 + \boldsymbol{k}_z^2}, \tag{4.25}$$

where the sign function is omitted because only positive ω values are included in the processing. The $\boldsymbol{k}_z$ vector contains the discrete k_z values, and is squared element by element. The interpolated values also have to be scaled according to (4.16), and the amplitude factors for k_{xj} are given by

$$\boldsymbol{a}_l(j) = \frac{\hat{c}_l}{\sqrt{1 + k_{xj}^2 / \boldsymbol{k}_z^2}}. \tag{4.26}$$

Assuming that all k_z values are negative, the $\boldsymbol{k}_z$ vector is given by

$$\boldsymbol{k}_z = -\delta k_z \cdot [0, 1, \ldots, N_{k_z} - 1]^T , \tag{4.27}$$

where δk_z is the step size between each k_z, and N_{k_z} is the total number of values. These should be chosen to cover the range of possible k_z values and also avoid any aliasing. This is fulfilled if

$$\delta k_z \leq \frac{2\pi}{\hat{c}_l} \cdot \frac{f_s}{N_t} \tag{4.28}$$

and

$$N_{k_z} \geq \frac{2\pi f_{\max} / \hat{c}_l}{\delta k_z}. \tag{4.29}$$

4.A.4 Detailed algorithm descriptions

Figure 4.11 illustrates the flow of the PSM and the MULOK algorithms, from the input ultrasonic data (denoted by $\boldsymbol{P}_{tx}[Z_1]$) to the focused image (denoted by $\boldsymbol{I}_{zx}$). $\boldsymbol{P}_{tx}[Z_1]$ is first Fourier transformed, and the elements corresponding to the transducer passband are extracted. Then, for each layer, the wave field is multiplied with the phase factor $\exp\left(i \sum_{m=1}^{l-1} \boldsymbol{K}_{zm} d_m\right)$ to shift it from Z_1 down to the top of the layer l, given by Z_l. For the first layer, the phase factor is set equal to 1, resulting in zero phase shift. The shifted wave field is a common starting point for both algorithms, and the subsequent steps for PSM and MULOK are shown on the left and the right side of the flowchart, respectively.

The PSM algorithm is based on forming an image line $\boldsymbol{i}(Z_l + \Delta z)$ for each depth to be imaged. The first operation is to compute $\boldsymbol{P}_{\omega k_x}[Z_l + \Delta z_l]$ by multiplying with the additional phase factor $\exp(i \boldsymbol{K}_{zl} \Delta z_l)$. An image line is then formed by summing over all ω and inverse Fourier transforming the resulting vector.

For the Stolt imaging algorithm, the next step after calculating $\boldsymbol{P}_{\omega k_x}[Z_l]$ is to interpolate from the original $\omega - k_x$ grid to a new $\omega - k_x$ grid. This is done by looping through all k_x values, interpolating for each column of $\boldsymbol{P}_{\omega k_x}[Z_l]$ with the ω values given by the $\boldsymbol{\omega}_l^{ip}(j)$ vector, and multiplying with the $\boldsymbol{a}_l(j)$ vector. Only part of the result corresponds to z values within the layer, that is, $\Delta z \in [0, d_l]$. For each layer, this part is cut out and saved as the local image $\boldsymbol{I}_{zx}[l]$.

When all the layers have been processed, the subimages $\boldsymbol{I}_{zx}[l]$ are stacked on top of each other to form the complete image of all the layers.

4.A.5 Analysis of asymptotic complexity

Having defined both the PSM and the MULOK implementations, it is possible to study the computational complexity of the two. Big O notation is used to describe the growth rate of operations as function of the size of the input data. As described in Section 4.A.4, the raw data $\boldsymbol{P}_{tx}[Z_1]$ is a N_t times M matrix, corresponding to N_t time samples and M measurement positions. After Fourier transforming the data, a N_ω times M submatrix of the result is extracted for use in the subsequent processing, where N_ω is proportional to N_t. The number of z lines for the PSM algorithm, denoted by N_z, and the number of k_z values for the MULOK algorithm, denoted by N_{k_z}, are also proportional to N_t. For the sake of asymptotic complexity analysis, we can ignore all such proportionality constants, and set $N_t = N_\omega = N_z = N_{k_z} = N$. The number of layers is denoted by L.

The initial Fourier transform, from (t, x) to (ω, k_x) coordinates, is a two-dimensional transform with complexity $O(MN \log MN)$. The following multiplication with a phase factor to calculate $\boldsymbol{P}_{\omega k_x}[Z_l]$ is an entrywise multiplication that is performed $L - 1$ times. The complexity of this operation is thus $O(NML)$.

For the phase shift migration algorithm, the wave field is multiplied with yet another phase factor. This multiplication is performed N times, once for each image line, and thus the complexity for all image lines is $O(MN^2)$. The summation over ω is also performed N times, resulting in a total complexity of $O(MN^2)$. Finally, the last operation is the inverse Fourier transform of an M-length vector, performed N times, which is $O(MN \log M)$. The complexities of the individual steps of the PSM algorithm are summarized in Table 4.1.

For the MULOK algorithm, the calculation of $\boldsymbol{P}_{\omega k_x}[Z_l]$ is followed by an interpolation step. The complexity of this step depends on the type of interpolation utilized, but in this work, the following method was used: $\boldsymbol{P}_{\omega k_x}[Z_l]$ was first interpolated to a denser rectangular grid by inverse Fourier transforming along the ω dimension, zeropadding, and Fourier transforming back again. This operation is $O(MN \log N)$. The final interpolation was subsequently performed by linear interpolation between points on this denser grid. This operation consists of a search to find the two closest ω values and calculating a weighted sum of P for these values, and the corresponding

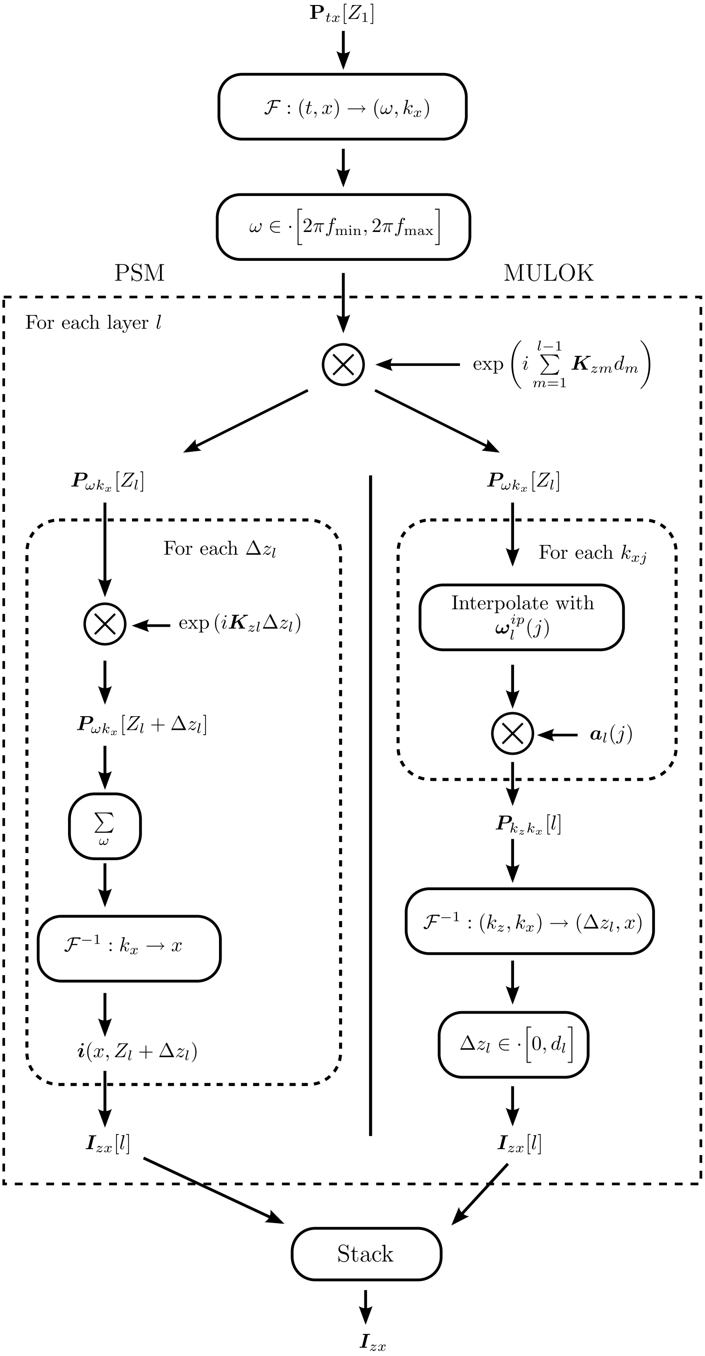

Figure 4.11: Flowchart for Stolt and phase shift migration algorithms, employing matrix representation of discrete data.

complexity is $O(MN \log N)$. Since the 2D interpolation is performed once for each layer, the overall complexity is then $O(LMN \log N)$. Multiplication with the amplitude factors $\boldsymbol{a}_l(j)$ is $O(LMN)$, and the inverse Fourier transform to produce the image is $O(LMN \log MN)$. The complexities of the different steps of the MULOK algorithm are summarized in Table 4.2.

4.B Tilt compensation

The multilayer algorithms presented in Chapter 4 and 5 require that the velocity is a function of depth only, $c(z)$. This assumption is violated if the interfaces between layers are non-planar. Variants of phase shift migration have been developed to treat more general velocity variations, see [Stoffa et al., 1990] and references therein. In ultrasonic scanning of man-made objects, which are often planar, the assumption can still be violated if the object is not placed parallel to the scanning plane. In practical applications it may be difficult to avoid tilting completely, and a method to robustly treat non-horizontal layers is therefore needed. The simple tilt-compensation method described here is based on extrapolating the measured wave field to a virtual measurement line that is parallel to the object surface. For simplicity, the method will only be presented for the 2D case, but an extension to 3D is straightforward.

The situation is illustrated in Fig. 4.12. An object is tilted with an angle θ relative to the measurement coordinate system. The tilt of the object is compensated by extrapolating the measured wave field from $z = Z$ to the virtual measurement line given by $z = Z + ax$, where $a = \tan\theta$.

The starting point for the tilt compensation is the wave field extrapolation given by (3.20). We set $Z = 0$, without loss of generality, and denote $P(\omega, k_x, z = 0)$ as $P(\omega, k_x)$ to simplify notation, yielding the following expression for the extrapolated wave field;

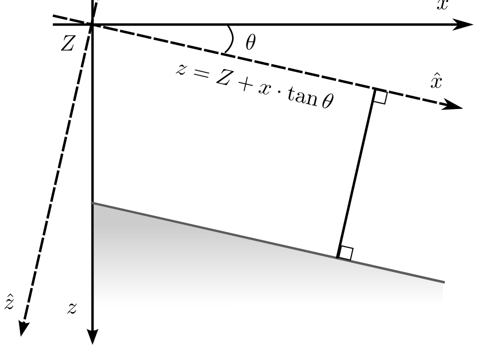

Figure 4.12: Rotated coordinate system for a tilted layer.

$$p(t,x,z) = \iint\limits_{-\infty}^{\infty} P(\omega,k_x)\cdot e^{ik_z z}\cdot e^{ik_x x}\cdot e^{-i\omega t}\,\mathrm{d}k_x\,\mathrm{d}\omega, \tag{4.30}$$

where k_z is a function of ω and k_x, as given by (3.19). We want to calculate the wave field along a tilted line $z = ax$, and insert this into (4.30):

$$p(t,x,z=ax) = \iint\limits_{-\infty}^{\infty} P(\omega,k_x)\cdot e^{ik_z ax}\cdot e^{ik_x x}e^{-i\omega t}\,\mathrm{d}k_x\,\mathrm{d}\omega. \tag{4.31}$$

Combining the $e^{ik_z ax}$ and $e^{ik_x x}$ terms, we obtain

$$p(t,x,z=ax) = \iint\limits_{-\infty}^{\infty} P(\omega,k_x)\cdot e^{i\hat{k}_x x}\cdot e^{-i\omega t}\,\mathrm{d}k_x\,\mathrm{d}\omega, \tag{4.32}$$

where $\hat{k}_x$ is given by

$$\begin{aligned}\hat{k}_x &= k_x + ak_z && (4.33)\\ &= k_x - a\cdot\operatorname{sgn}(\omega)\cdot\sqrt{\frac{\omega^2}{\hat{c}^2} - k_x^2}. && (4.34)\end{aligned}$$

The integral in (4.32) can be recast as a proper inverse Fourier Transform by a substitution of variables. Rearranging (4.34), we obtain

$$k_x(\omega,\hat{k}_x,a) = \frac{1}{1+a^2}\left(\hat{k}_x + a\sqrt{(1+a^2)\cdot\frac{\omega^2}{\hat{c}^2} - \hat{k}_x^2}\right). \tag{4.35}$$

By using the calculus rules of substitution, (4.32) is transformed to

$$p(t,x,z=ax) = \iint P(\omega,\hat{k}_x)\ e^{i\hat{k}_x x}e^{-i\omega t}\mathrm{d}\hat{k}_x\mathrm{d}\omega, \tag{4.36}$$

where

$$P(\omega,\hat{k}_x) = A(\hat{k}_x,\omega,a)\cdot P\left(\omega, k_x(\omega,\hat{k}_x,a)\right), \text{ and} \tag{4.37}$$

$$A(\omega,\hat{k}_x,a) = \frac{\partial k_x}{\partial\hat{k}_x} = \frac{1}{1+a^2}\left(1 - \frac{a\hat{k}_x}{\sqrt{(1+a^2)\cdot\frac{\omega^2}{\hat{c}^2} - \hat{k}_x^2}}\right). \tag{4.38}$$

In practice, the substitution of k_x with $\hat{k}_x$ is performed by an interpolation in the k_x domain, similar to the interpolation performed for Stolt migration, as described in Section 3.5.4. Note also that if the wave field is sampled with a spacing of δx_s in the original coordinate system, it is sampled with $\delta\hat{x}_s = \delta x_s/\cos\theta$ in the rotated coordinate system.

After the transformation to the rotated coordinate system, the Fourier-domain wave field $P(\omega, \hat{k}_x)$ given by (4.37) can be used directly by the PSM algorithm as the starting point for wave field extrapolation.

A simple experiment was performed to demonstrate tilt compensation on real data. A copper block with a number of side-drilled holes was scanned using a 2.25 MHz transducer with 10 mm diameter. The copper block was tilted approximately 2 degrees relative to the transducer scan line. In the resulting raw data set, shown in Fig. 4.13(a), the front and back surface reflections are seen as tilted lines, and the side-drilled holes are seen as a number of curved reflections from inside the block.

The tilt compensation method described above was applied, extrapolating the wave field to the virtual scan line indicated in Fig. 4.13(a). The resulting wave field, shown in Fig. 4.13(b), was focused using the multilayer PSM algorithm, and the focused image is shown in Fig. 4.13(c).

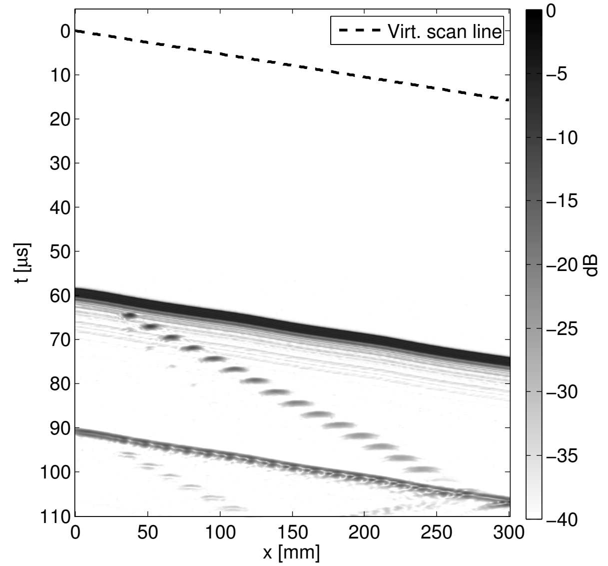

(a) Raw data

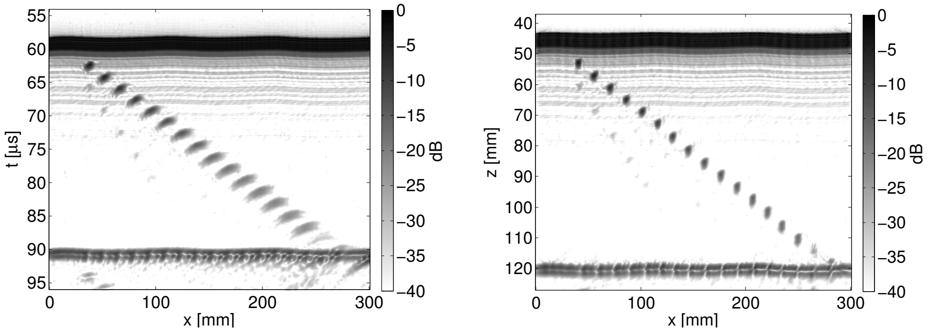

(b) Raw data, compensated for tilt

(c) Focused image

Figure 4.13: Raw data, tilt compensated data, and PSM focused image from experiment with side-drilled holes in copper block.

Chapter 5

3D multilayer synthetic aperture imaging

In the two previous chapters, the SAFT algorithms were presented for a two-dimensional geometry. In some synthetic aperture applications, such as synthetic aperture radar and sonar, the region being imaged is essentially two-dimensional, and such algorithms are sufficient. However, in ultrasonic imaging the region of interest is often a three-dimensional volume, and to image such a volume, the transducer must be moved over a surface rather than along a line. This produces a 3D data set with pulse-echo time on one axis and surface coordinates on the other two axes.

3D versions of SAFT have been developed alongside 2D algorithms since SAFT came into use [Doctor et al., 1986; Mayer et al., 1990; Doctor et al., 1996], and experiments have shown that they can yield a significant increase in resolution along both lateral axes. In this chapter, we expand the PSM algorithm to enable multilayer 3D imaging. A similar expansion of the MLDAS and MULOK algorithms is relatively simple, but is not included here. The performance of the 3D PSM algorithm is evaluated through an experiment with point-like scatterers in acrylic glass and aluminium layers. To demonstrate the difference between 2D and 3D focusing, the 2D PSM algorithm is also applied for the same experiment, by independently processing 2D slices from the 3D data set.

One of the potential uses of multilayer SAFT is imaging of pitting corrosion where the object under test can only be accessed from the non-corroded side. An example of pitting corrosion is shown in Fig. 5.1(a), and the corresponding two-layer measurement geometry is illustrated in Fig. 5.1(b). At the end of the chapter, we present an experiment with 3D SAFT imaging of artificial pitting in an aluminium plate.


(a) (b)

Figure 5.1: (a) Example of pitting corrosion. (b) Measurement geometry for outside pitting corrosion.

5.1 Expansion of PSM to 3D

The derivation of the PSM algorithm for the 2D case is given in Section 3.5, and this derivation follows along the same lines. In a three-dimensional Cartesian coordinate system, plane wave solutions to the acoustic wave equation are on the form

$$p(t,x,z) \propto e^{i(k_x x + k_y y + k_z z - \omega t)} \tag{5.1}$$

where k_x, k_y and k_z are the wavenumbers along the x, y and z axes. The wavenumbers are related to ω through the dispersion relation

$$\left(\frac{\omega}{\hat{c}}\right)^2 = k_x^2 + k_y^2 + k_z^2 \tag{5.2}$$

where we have used the effective wave velocity $\hat{c} = c/2$ according to the exploding reflector model described in Section 3.2. We choose k_z as the dependent variable, and assume that all recorded waves propagate in the negative direction along the z axis, so that k_z and ω have opposite signs:

$$k_z(\omega, k_x, k_y, \hat{c}) = -\operatorname{sgn}(\omega) \cdot \sqrt{\frac{\omega^2}{\hat{c}^2} - k_x^2 - k_y^2}. \tag{5.3}$$

We denote the Fourier transform of a 3D wave field at depth z as

$$P(\omega, k_x, k_y, z) = \mathcal{F}_{t,x,y}\big\{p(t,x,y,z)\big\}, \tag{5.4}$$

and the inverse transform as

$$p(t,x,y,z) = \mathcal{F}^{-1}_{t,x,y}\big\{P(\omega, k_x, k_y, z)\big\}. \tag{5.5}$$

The pulse-echo wave field is recorded in the $x-y$ plane given by $z = Z$. As for the 2D case, the wave field can be extrapolated to an arbitrary depth z by a phase shift in the Fourier domain;

$$P(\omega, k_x, k_y, Z + \Delta z) = P(\omega, k_x, k_y, Z) \cdot \exp\left(i k_z \Delta z\right). \tag{5.6}$$

A focused 2D image plane at depth z is obtained by integrating over ω and inverse Fourier transforming from (k_x, k_y) to (x, y) coordinates:

$$i_p(x, y, Z + \Delta z) = \mathcal{F}^{-1}_{x,y} \left\{ \int_{-\infty}^{\infty} P(\omega, k_x, k_y, Z) \cdot \exp\left(ik_z \Delta z\right) \, \mathrm{d}\omega \right\}. \tag{5.7}$$

A full 3D image is formed by applying (5.7) for all depths of interest. The adaptation of 3D PSM to multilayer imaging follows that of Section 4.2.1 exactly, and will not be repeated here.

5.2 Point scatterer experiment

To test 3D imaging in multilayered media, an experiment similar to that described in Section 4.5 was performed. The experimental setup is shown in Fig. 5.2. Two test blocks, one made of acrylic glass and the other of aluminium, were manufactured for the experiment. Each block had four flat-bottom holes with 3 mm diameter, spaced 20 mm apart. The holes in the acrylic glass block were 6, 12, 18 and 24 mm deep, and the holes in the aluminium block were 10, 20, 30 and 40 mm deep. The acrylic glass block was placed on top of the aluminium block, and the arrangement was immersed in water to create a three-layer structure. The blocks were also placed with a 10 mm offset in both the x and y directions, to ensure that the holes in the aluminium block would not be shadowed by the holes in the acrylic glass block. A 3D plot of the holes in the blocks is shown in Fig. 5.3.

3D raw data for the two blocks was acquired by scanning a 2.25 MHz, 6 mm diameter transducer 63 mm above the surface of the acrylic glass block,

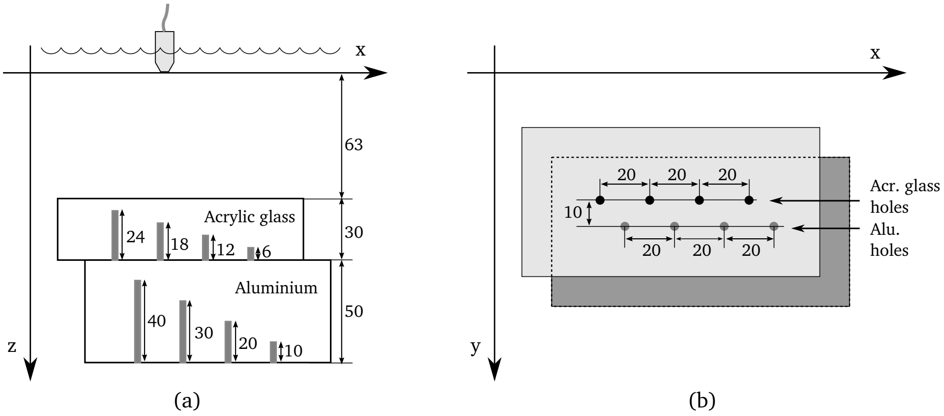

Figure 5.2: Experimental setup, acrylic glass and aluminium blocks with flat-bottom holes. (a) Seen from side. (b) Seen from above. All dimensions are in mm.

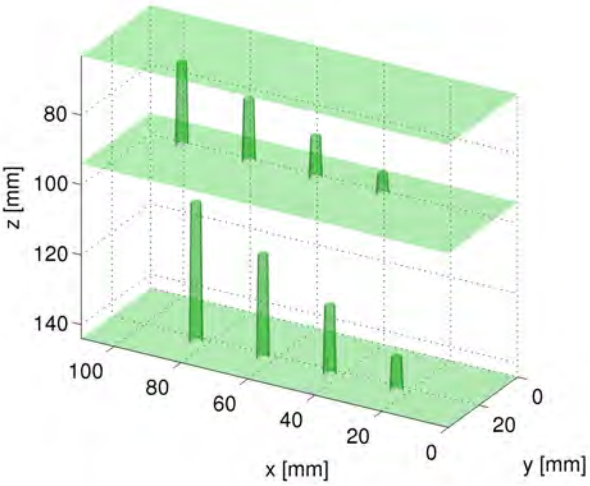

Figure 5.3: 3D plot of flat-bottom holes drilled into acrylic glass (top) and aluminium (bottom).

as shown in Fig. 5.2. The spatial sampling interval was 1 mm along both axes. Figure 5.4 shows an isosurface plot of the raw data. In each layer, the isosurfaces encapsulate all voxels with amplitudes above 1/5 of the maximum amplitude in the layer, which was found to be a suitable threshold for visualization. The layer interfaces are indicated with simple green planes. The plot shows that the scatterer responses are disc-shaped, and that the responses in the aluminium layer are wider than in the acrylic glass layer, due to the divergence of the transducer beam. Because of the transmission loss at the interface between the layers, the responses from the aluminium layer are also quite noisy.

To illustrate the difference between 2D and 3D SAFT, the data set was processed using both the 2D and 3D version of the PSM algorithm. With the 2D version, each $x-z$ plane of the raw data was processed separately. Isosurfaces for both focused data sets, generated in the same way as for Fig. 5.4, are shown in Fig. 5.5. For the 2D focused data in Fig. 5.5(a), the SAFT processing has significantly reduced the PSF width along the x axis, while the width along the y axis is unchanged. In comparison, Fig. 5.5(b) shows that 3D focusing reduces the PSF width equally along both axes.

As an alternative visualization of the data, amplitude C-scans were made, by detecting the maximum amplitude along the depth axis within each layer. The results are shown in Fig. 5.6. As in Fig. 5.4 and 5.5, it is seen that 2D SAFT improves the lateral resolution along the x axis only, while 3D PSM yields significant improvement along both axes. Note that in the aluminium layer, the 2D SAFT yields some reduction of the background noise relative to the raw data, and 3D SAFT yields an even further improvement. This is because

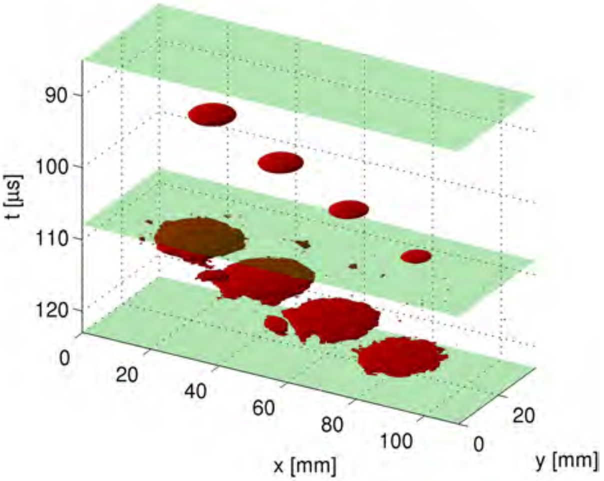

Figure 5.4: 3D plot of raw data from flat-bottom holes in acrylic glass and aluminium layers. In each layer, the scatterers are shown as isosurfaces encapsulating all voxels with amplitudes above 1/5 of the maximum amplitude.

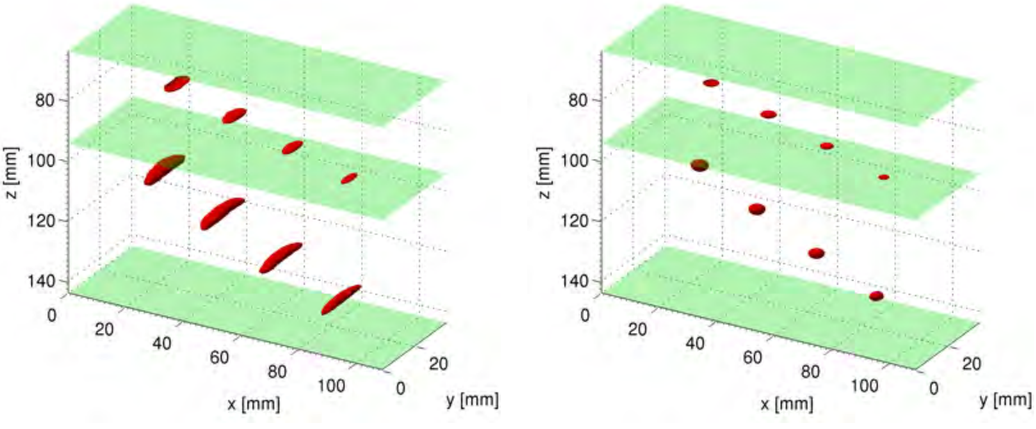

(a) 2D focused

(b) 3D focused

Figure 5.5: Isosurface plots of focused data from experiment with point scatterers in acrylic glass and aluminium layers. (a) Data focused using the 2D PSM algorithm for each $x - z$ plane. (b) Data focused using the full 3D PSM algorithm.

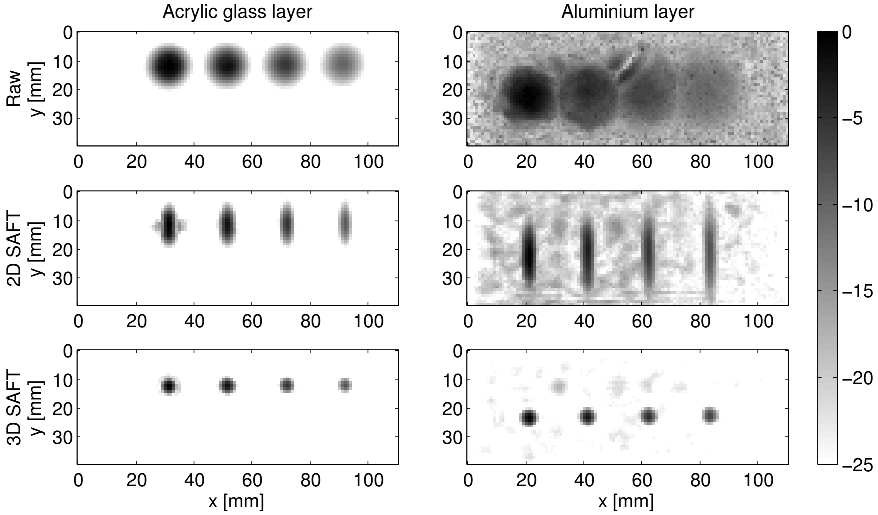

Figure 5.6: C-scans obtained from 3D data sets. Left: Acrylic glass layer. Right: Aluminium layer. Top to bottom: Raw data, image focused with 2D PSM for $x-z$ planes, and image focused with 3D PSM. The images have been normalized relative to the highest amplitude in each image.

the responses from the scatterers are coherently added in synthetic aperture processing, while random measurement noise tends to cancel itself out [Frazier and O'Brien Jr., 1998]. The improvement is more significant for the 3D case because the coherent summation includes a larger number of measurements.

The average -6 dB diameter of the PSF for each scatterer was estimated for raw and 3D focused data, by measuring the -6 dB area a in the C-scan, and setting the diameter $d = \sqrt{\pi/a}$. The results are shown in Fig. 5.7, with -6 dB diameter plotted against the z position of each scatterer.

In the acrylic glass layer, the diameter is approximately 10 mm for all the scatterers. However, after the experiment was performed, it was found that the responses from the two uppermost scatterers were clipped in the signal acquisition, resulting in an overestimation of the diameter for these scatterers. In the aluminium layer, the diameter increases with depth, up to approximately 22 mm for the deepest scatterer.

After focusing, the diameter is approximately the same for each scatterer, with a mean diameter of 2.3 mm in the acrylic glass and 2.7 mm in the aluminium. This corresponds well to the theoretical resolution of approximately half the transducer diameter, as derived in Section 3.6.1.

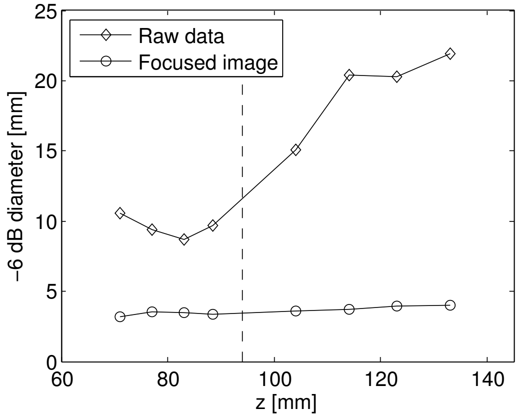

Figure 5.7: Estimated -6 dB diameter of scatterers. The interface between the acrylic glass and aluminium layers is indicated with a vertical dashed line.

5.3 Experiment with artificial pitting corrosion

A second experiment was conducted to test the application of 3D SAFT for imaging of pitting corrosion. Several pits of various sizes were machined out of a 30 mm aluminium plate, as shown in Fig. 5.8(a). The pitting profile is shown as a 3D surface plot in Fig. 5.8(b), and as a plot of remaining plate thickness in Fig. 5.8(c). The test block was immersed in water, and a transducer with 2.25 MHz center frequency and 6 mm diameter was used to perform a 3D scan of the block. The distance from the scanning surface to the block was 50 mm, as shown in Fig. 5.8(d), and the spatial sampling interval was 0.5 mm along both axes.

The raw data was processed with the 3D PSM algorithm, and for both the raw and the focused data sets, the maximum amplitude below the front surface was detected. The resulting amplitude C-scans are shown in Fig. 5.9(a) and 5.9(b). The plate thickness was also estimated, through the depth difference between the front surface echo and the maximum amplitude reflection within the plate. Figures 5.9(c) and 5.9(d) show the estimated thickness of the plate for the raw and focused data, respectively.

In the raw data amplitude C-scan in Fig. 5.9(a), the back-scattered amplitude is generally lower in the pitting area, due to increased scattering. The general shape of the low-amplitude area matches the shape of the pitting profile, but no further details can be seen. In comparison, the focused amplitude image in Fig. 5.9(b) shows several localized areas with strong backscattering, which closely match the local peaks of the pitting profile. Note that in areas where the pitting surface is oblique relative to the transducer scanning plane, for example along the circumference of the pitting area, the amplitude is very low. This is because the oblique surfaces deflect the ultrasonic pulse, reflecting little or no energy back towards the transducer.

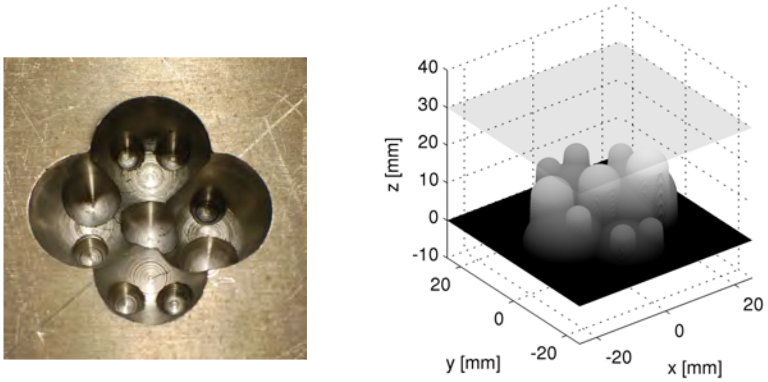

(a) Machined pits on outside of plate

(b) 3D plot of artificial pitting.

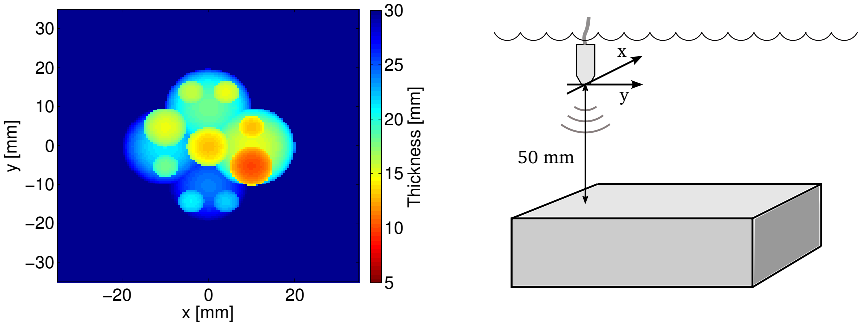

(c) Remaining plate thickness

(d) Measurement geometry

Figure 5.8: Pitting profile and measurement geometry for experiment with 3D imaging of pitting in aluminium plate.

The images of estimated thickness in Fig. 5.9(c) and 5.9(d) should ideally be identical to Fig. 5.8(c). However, the thickness estimated from raw data is seen as a collection of irregularly shaped patches. The thickness for the patches matches the thickness for parts of the pitting profile, but the overall shape is not close to the true pitting shape. In comparison, the thickness plot for the focused data is relatively accurate, although the individual peaks appear somewhat flattened. Sections with back-scattered amplitude below -20 dB were masked out with a white color, since they were found to yield erroneous thickness estimates.

The lateral resolution of the focused images is generally slightly better in the x direction than in the y direction. It is assumed that this is due to a difference in the scanner positioning accuracy between the two axes.

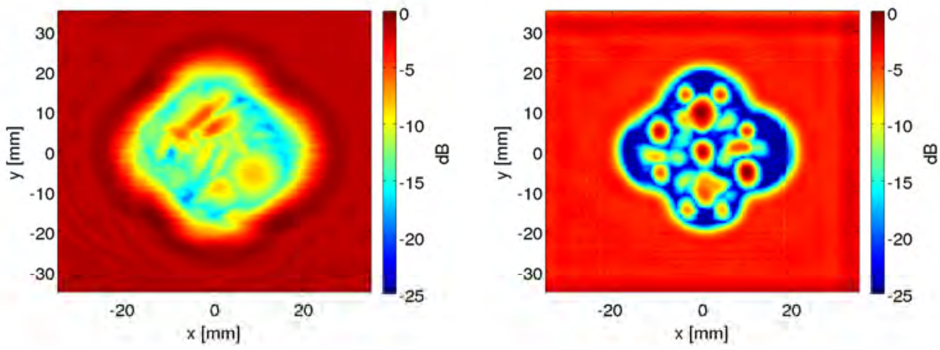

(a) Amplitude C-scan, raw data

(b) Amplitude C-scan, focused image

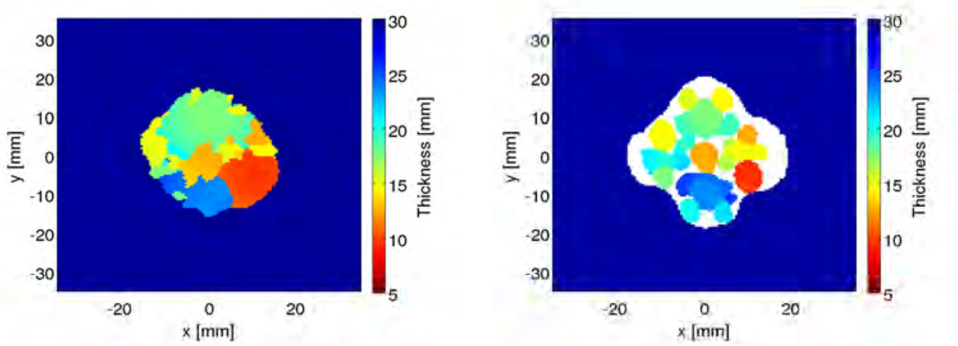

(c) Estimated thickness, raw data

(d) Estimated thickness, focused image

Figure 5.9: Amplitude and thickness plots based on the maximum amplitude detected below the surface echo of the aluminium plate. In (d), thickness estimates for reflections below -20 dB relative to the maximum amplitude are masked with white color.

5.4 Discussion

The experiment with point scatterers in Section 5.2 demonstrated that using 2D SAFT on a 3D data set yields a focusing effect along only one of the two lateral axes. In some applications this can be sufficient, for example if the transducer is physically focused along the other axis. However, to achieve a high lateral resolution along both axes using an unfocused transducer, the full 3D SAFT algorithm is required.

For Fourier domain algorithms for 3D SAFT, like the PSM algorithm presented in this chapter, the memory requirements are quite high. The full 3D data set, which easily grows to several million points even for moderately sized scans, has to be Fourier transformed and stored in memory. In practical applications, the data set can be segmented into smaller blocks, whose size are adjusted to the available memory. Some overlap between the blocks is then required to properly focus objects close to the block edges, reducing the overall efficiency of the imaging algorithm. Time-domain SAFT algorithms focus each pixel independently, only requiring that data from within the synthetic aperture are available. Thus, even though Fourier-domain algorithms are generally faster than time-domain algorithms, as shown in Section 4.4.2, a time-domain algorithm like MLDAS may in some cases be preferred for 3D multilayer imaging, due to its small memory footprint.

The experiment with artificial pitting in Section 5.3 showed that parts of the pitting profile yielded very little backscattered energy. This effect is due to specular reflections at oblique surfaces, and is well known within the field of ultrasonic NDT [Kino et al., 1980; ASNT, 2007]. However, the pitting profile used in the experiment was very smooth, and the irregular surface created by real pitting corrosion may yield more backscattered energy from oblique surfaces.

5.5 Summary

In this chapter we have extended the PSM algorithm for three-dimensional imaging. Through an experiment on point-like scatterers in a multilayered geometry, we have shown that the attainable resolution along both lateral axes is approximately half the transducer diameter, independent of depth or layer. In a second experiment, we have demonstrated that 3D multilayer SAFT can be used for high-resolution imaging and sizing of pitting corrosion on the outside of a plate. However, the experiment also indicated that it is difficult to form a complete image of the pitting shape, due to specular reflections at oblique surfaces.

Chapter 6

Imaging in cylindrical geometries

In the previous chapters, synthetic aperture algorithms for measurements performed along a straight line or over a flat plane were presented. However, in some applications, for example imaging in blood vessels or pipes, a cylindrical measurement geometry is more suitable [Haun et al., 2002; Duran et al., 2002]. In this chapter we consider the measurement geometry shown in Fig. 6.1, where a transducer is moved over a cylindrical surface, performing outward pulse-echo measurements.

SAFT algorithms for similar measurement geometries have previously been proposed. O'Donnell and Thomas [1992] describe a time-domain SAFT algorithm for internal coronary imaging using circular arrays, and in a follow-up paper [O'Donnell et al., 1997], practical results from a catheter-mounted array are reported. An approximate Fourier-domain algorithm for a similar circular array is described in [Vray et al., 2001]. However, the circular array yields a two-dimensional image, and in order to create a three-dimensional focused image, the full cylindrical measurement surface has to be used. Haun et al. [2002] present a Fourier domain algorithm for three-dimensional imaging using a cylindrical measurement geometry. The algorithm is derived using an approximate expression for the transducer-target distance, and the transducer beam is required to be relatively narrow for the algorithm to be accurate.

In this chapter, we present a SAFT algorithm for cylindrical scans which has no restrictions on the transducer beamwidth. The algorithm is based directly on the Fourier domain solutions to the scalar wave equation, and in this sense the algorithm is exact. Thus, compared to the algorithm in [Haun et al., 2002], the proposed algorithm extends Fourier-domain SAFT for cylindrical scans to the general case.

In a practical implementation of the algorithm, it is important to have a good estimate of the attainable resolution. In Section 3.6.1 it was shown that for a linear scan, the lateral resolution after SAFT focusing is approximately equal to half the transducer diameter. In this chapter, we derive a similarly

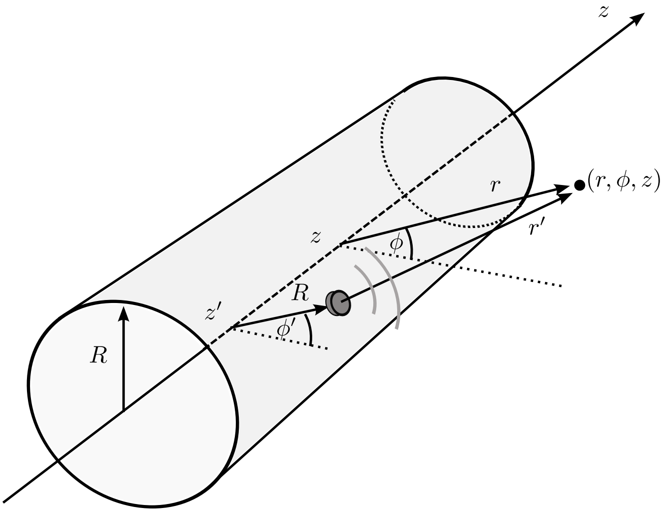

Figure 6.1: Cylindrical scanning geometry. A transducer is scanned over a cylindrical surface given by a constant radius R. The transducer coordinates are denoted (R,ϕ',z'), and the coordinates of a point scatterer are denoted (r,ϕ,z). The distance between the transducer and the scatterer is denoted r'.

simple expression for the attainable resolution of a cylindrical scan.

To test the performance of the new algorithm, we apply it in a number of numerical simulations and experiments on point-like scatterers. We also demonstrate the difference between the proposed algorithm and the algorithm in [Haun et al., 2002], through a simulation with a wide-beam transducer.

6.1 Theory

6.1.1 Wave equation solutions in cylindrical coordinates

In cylindrical coordinates, solutions to the scalar acoustic wave equation are on the form [Williams, 1999]

$$p(t,\phi,z,r) \propto H_n^{(1),(2)}(k_r r)e^{\pm in\phi}e^{\pm ik_z z}e^{-i\omega t}, \tag{6.1}$$

where $H_n^{(1),(2)}(k_r r)$ denotes a Hankel function of the first or second kind, of order n. The wavenumbers along the r and z axes are denoted k_r and k_z, respectively, and ω denotes angular frequency. The relationship between k_r, k_z and ω is given by

$$k_r = \sqrt{\left(\frac{\omega}{\hat{c}}\right)^2 - k_z^2}, \tag{6.2}$$

where we have used the effective wave velocity $\hat{c} = c/2$ according to the exploding reflector model described in Section 3.2. The Hankel functions of first and second order correspond to outward and inward traveling waves, respectively. We assume here that the wave field is measured on the cylindrical surface given by $r = R$, and that all sources are located in the space $r > R$. In this case, only inward traveling waves are recorded, and thus the wave equation solutions are limited to Hankel functions of the second kind. The most general solution is a combination of all possible solutions,

$$p(t, \phi, z, r) = \sum_{n=-\infty}^{\infty} e^{in\phi} \iint\limits_{-\infty}^{\infty} A_n(k_z, \omega) H_n^{(2)}(k_r r)\, e^{ik_z z} e^{-i\omega t}\, \mathrm{d}k_z \mathrm{d}\omega, \tag{6.3}$$

where $A_n(k_z, \omega)$ denotes the complex amplitude for each individual solution.

6.1.2 Wave field extrapolation

The sound pressure at the cylindrical plane given by $r = R$ is denoted by $p(t, \phi, z, R)$. Since ϕ is periodic with 2π, the transformation of $p(t, \phi, z, R)$ from the time-space domain to the Fourier domain is given by a Fourier series expansion in ϕ and a Fourier transform in z and t:

$$P_n(\omega, k_z, R) = \left(\frac{1}{2\pi}\right)^3 \cdot \int\limits_0^{2\pi} \mathrm{d}\phi \iint\limits_{-\infty}^{\infty} p(t, \phi, z, R)\, e^{-in\phi} e^{-ik_z z} e^{i\omega t}\, \mathrm{d}z\, \mathrm{d}t, \tag{6.4}$$

where $\left(\frac{1}{2\pi}\right)^3$ is a normalization factor. The inverse transform is given by

$$p(t, \phi, z, R) = \sum_{n=-\infty}^{\infty} e^{in\phi} \iint\limits_{-\infty}^{\infty} P_n(\omega, k_z, R)\, e^{ik_z z} e^{-i\omega t}\, \mathrm{d}k_z\, \mathrm{d}\omega. \tag{6.5}$$

To simplify notation, the transforms will be denoted $\mathcal{F}_{t,\phi,z}\{\cdot\}$ and $\mathcal{F}^{-1}_{t,\phi,z}\{\cdot\}$, for the forward and inverse transform, respectively. Comparing (6.5) with (6.3) and solving for $A_n(k_z, \omega)$, we obtain an expression for extrapolating the wave field measured at $r = R$ to an arbitrary range r,

$$p(t, \phi, z, r) = \mathcal{F}^{-1}_{t,\phi,z} \left\{ P_n(\omega, k_z, R) \cdot \frac{H_n^{(2)}(k_r r)}{H_n^{(2)}(k_r R)} \right\}. \tag{6.6}$$

Thus, in the Fourier domain the wave field is extrapolated from R to r through multiplication with the transfer function

$$G(\omega, n, k_z, r, R, \hat{c}) = \frac{H_n^{(2)}(r\sqrt{(\omega/\hat{c})^2 - k_z^2})}{H_n^{(2)}(R\sqrt{(\omega/\hat{c})^2 - k_z^2})}, \tag{6.7}$$

where the expression for k_r from (6.2) has been inserted to show the dependence on ω and k_z.

In the measurement geometry shown in Fig. 6.1, the positions of the transducer and a point scatterer are given by cylindrical coordinates (R, ϕ', z') and (r, ϕ, z), respectively. The transducer-scatterer distance is given by

$$r' = \sqrt{R^2 + r^2 - 2Rr\cos(\phi - \phi') + (z - z')^2}. \tag{6.8}$$

Haun et al. [2002] use the Rayleigh-Sommerfeld diffraction formula to derive an approximate expression for the transfer function G,

$$\hat{G}(\omega, n, k_z, r, R, \hat{c}) \approx \sqrt{\frac{r}{R}} \exp\left(i(r - R)\sqrt{\frac{\omega^2}{\hat{c}^2} - \frac{n^2}{Rr} - k_z^2} \right). \tag{6.9}$$

$\hat{G}$ is accurate as long as the term $\cos(\phi - \phi')$ in (6.8) can be approximated as $1 - (\phi - \phi')^2/2$. If the transducer has a narrow beamwidth, this is valid, and $\hat{G}$ can be used for wave field extrapolation. An analysis of the accuracy of the approximation is included in [Haun et al., 2002].

6.1.3 Imaging

To obtain a focused image from the extrapolated wave field, we apply the imaging condition for the exploding reflector model, $t = 0$, to (6.6). This reduces the inverse transform from ω to t to a simple integral over ω, and yields the following expression for the image plane i_p at range r:

$$i_p(r, \phi, z) = \mathcal{F}^{-1}_{\phi,z}\left\{ \int_{-\infty}^{\infty} P_n(\omega, k_z, R) \cdot G(\omega, n, k_z, r, R, \hat{c})\, \mathrm{d}\omega \right\}. \tag{6.10}$$

Equation (6.10) can be used iteratively to build a three-dimensional image for a set of ranges r. A flow chart illustrating this algorithm is shown in Fig. 6.2. The pulse-echo measurements $p(t, \phi, z, R)$ are first Fourier transformed to obtain $P_n(\omega, k_z, R)$, and then for each range r, the wave field is extrapolated from R to r by multiplication with the transfer function $G(\omega, n, k_z, r, R, \hat{c})$. A focused image plane $i_p(\phi, z, r)$ is obtained by integration over ω and inverse Fourier transformation to spatial coordinates. The procedure is similar to the PSM algorithm described in Section 3.5 and 5.1, and we will therefore refer to it as the Cylindrical Phase Shift Migration algorithm (CPSM).

6.1.4 Lateral resolution

The attainable angular resolution is given by the bandwidth of the angular wavenumber, Δn [Haun et al., 2002]. To determine Δn, an expression for the minimum and maximum n must be found. In the following analysis we use the real wave velocity, c, rather than the effective wave velocity, $\hat{c}$.

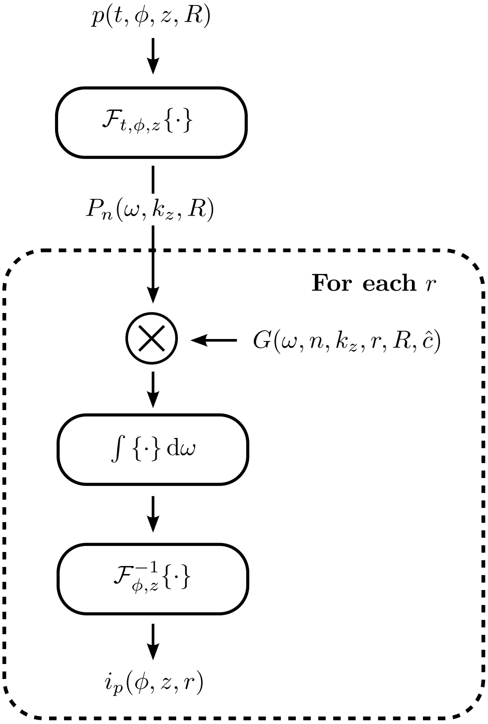

Figure 6.2: Flow-chart of the focusing algorithm described in Section 6.1.3. The 3D raw data is first Fourier transformed, and then focused for constant r planes, by multiplication with the transfer function G, summation over ω, and inverse Fourier transformation.

The phase of a signal that is emitted from the transducer and reflected back is given by $2\omega \cdot (r'/c)$, where r' is given by (6.8). Using the same approach as in Section 3.6.1, we obtain an expression for n by calculating the derivative of the phase with regard to ϕ, yielding

$$n = \frac{\omega}{c/2} \cdot \frac{Rr\sin(\phi-\phi')}{r'} \ . \tag{6.11}$$

From (6.8) and (6.11) it is seen that with regard to z, $|n|$ is maximum if $z - z' = 0$, and thus it is sufficient to look at the 2D case where $z = z'$. This case is shown in Fig. 6.3. The angle γ indicated in Fig. 6.3 represents the angular coordinate in a polar coordinate system that follows the transducer. The relation between ϕ, ϕ' and γ is given by the law of sines, which enables us to rewrite (6.11) as

$$n = \frac{4\pi}{\lambda} \cdot R\sin\gamma. \tag{6.12}$$

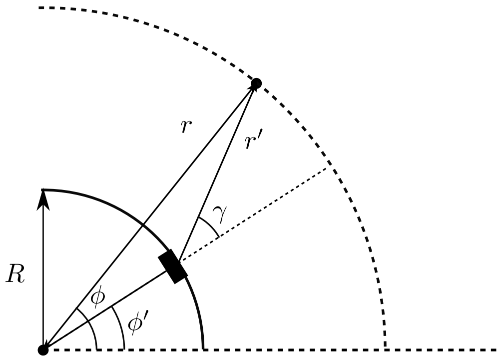

Figure 6.3: Circular scan geometry, where (r, ϕ) denotes the global coordinate system, and (r', γ) denotes the coordinate system following the transducer.

Thus, the range of n depends on the range of γ, which is given by the width of the transducer beam. If the transducer is flat and circular with diameter D, its directivity is given by the jinc function in (2.4), and for the pulse-echo case, the -6 dB points are given by

$$\sin\gamma = \pm 0.515\frac{\lambda}{D}. \tag{6.13}$$

Inserting (6.13) into (6.12), and rounding off 0.515 to 0.5, we find that the range of n is approximately given by

$$n \in \left[-\frac{2\pi R}{D}, \frac{2\pi R}{D}\right], \tag{6.14}$$

so that the bandwidth of n is $\Delta n \approx 4\pi\frac{R}{D}$. Thus, the attainable resolution in ϕ is

$$\delta\phi = \frac{2\pi}{\Delta n} \approx \frac{D}{2R}. \tag{6.15}$$

This indicates that the angular resolution after focusing is approximately constant with regard to range, only depending on the size of the transducer and the radius of the measurement arc. $\delta\phi$ is also an expression for the maximum angular step size that can be used, if the spatial sampling criterion is to be satisfied.

The attainable resolution along the z axis can be derived from the k_z bandwidth, following the same approach as above. $|k_z|$ is maximum for the 2D case $\phi' = \phi$, which is similar to the linear scan case described in Section 3.6.1. The attainable resolution is therefore

$$\delta z \approx \frac{D}{2}. \tag{6.16}$$

The angular resolution in (6.15) corresponds to a spatial resolution which depends on the range r. This "arc length" resolution is given by

$$\delta s = \delta\phi \cdot r = \frac{Dr}{2R}, \tag{6.17}$$

which is equal to δz for $r = R$, and larger than δz for all $r > R$.

6.2 Numerical simulations

6.2.1 Model

A number of numerical simulations were performed to study the performance of the CPSM algorithm with different system parameters. It was assumed that the propagating medium was water, with wave velocity 1500 m/s, and that a single point scatterer was present in the medium. The transducer face was assumed to be flat and circular, with uniform excitation, and the emitted signal, $s_0(t)$, was modeled as a Gaussian-modulated sinusoidal pulse with center frequency 1.5 MHz and 60% relative band width. Absorption in water is relatively low in this frequency range, and absorption was therefore not included in the model.

For each transducer position (ϕ', z'), the transducer-scatterer distance r' was calculated using (6.8). The backscattered signal received by the transducer was modeled as

$$s(t, \phi', z') = \left(\frac{1}{r'}\right)^2 \int_{-\infty}^{\infty} S_0(\omega) \cdot e^{i\omega 2r'/c} \cdot D_{\mathrm{C,PE}}(\omega, \gamma) \cdot e^{-i\omega t} \, \mathrm{d}\omega, \tag{6.18}$$

where the factor $(1/r')^2$ is due to the two-way geometrical spreading of the wave front, $S_0(\omega)$ denotes the Fourier transform of $s_0(t)$, and the phase shift given by $e^{i\omega 2r'/c}$ accounts for the two-way travel time of the pulse. $D_{\mathrm{C,PE}}(\omega, \gamma)$ denotes the pulse-echo jinc directivity function in (2.7). The simulations were performed with discretely sampled signals, but (6.18) is presented in continuous time for consistency with the theory as presented in Section 6.1. All simulations were performed in Matlab.

The envelope of the simulated raw data was found by first applying the Hilbert transform and then taking the absolute value of the resulting analytic signal. The CPSM algorithm produces complex-valued images, and the envelope of each focused image was found directly by its absolute value.

Although the CPSM algorithm is three-dimensional in nature, it is the angular dimension that is of most interest here. The simulations were therefore limited to two-dimensional angular scans, with the transducer and scatterer placed at the same z coordinate, $z' = z$. Since an angular scan is a special case of the cylindrical scan, it can be processed with the CPSM algorithm without any modifications.

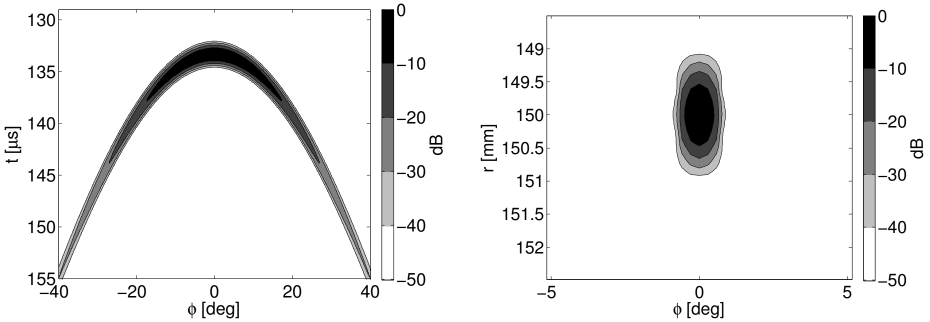

(a) Raw data envelope

(b) Focused with exact transfer function

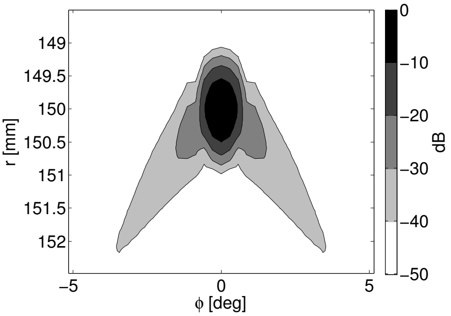

(c) Focused with approximate transfer function

Figure 6.4: Raw data and focused images for simulated point scatterer with scanning radius $R = 50$ mm and scatterer range $r = 150$ mm. Note that the axis ranges are smaller for the focused images.

6.2.2 Comparison of exact and approximate algorithm for wide beam transducer

A simulation was conducted to compare the performance of the algorithm proposed here with the algorithm presented in [Haun et al., 2002]. The only difference between the two is that the proposed algorithm uses the exact transfer function given in (6.7), while the algorithm in [Haun et al., 2002] uses the approximate transfer function in (6.9).

A point reflector located at $r = 150$ mm was scanned by a 1.5 mm diameter circular transducer, moved along a circular arc with 50 mm radius. Using (2.4), the -6 dB width of the transducer beam is found to be approximately $\Delta\gamma = 56°$ at the center frequency. The raw data envelope of the scan is shown in Fig. 6.4(a), illustrating that the point scatterer response is curved and very wide.

The simulated data was processed with both the exact and the approximate algorithm, and the focused point responses are shown in Figs. 6.4(b) and 6.4(c). Note that the axis ranges are different from those of Fig. 6.4(a). The exact algorithm produces a round, focused point, while the approximate algorithm produces a point with low-amplitude sidelobes. For the exact algorithm, the -6 and -40 dB width of the focused point is 0.81 and 2.01 degrees, respectively. In comparison, the -6 and -40 dB width for the approximate algorithm is 0.89 and 8.39 degrees. Thus, the sidelobes of the approximate algorithm make the response relatively wide at low amplitudes.

6.2.3 Effect of transducer size and scanning radius on lateral resolution

In Section 6.1.4 it was found that for a circular transducer of diameter D, the angular resolution after focusing should be approximately $D/(2R)$. A number of 2D scans were simulated to study the effect of D and R on the angular resolution.

Simulations with $D = [2,4,6]$ mm and $R = [50,100,150]$ mm were performed, with a point scatterer placed 100 mm outside the measurement arc. The scans were processed with the CPSM algorithm, and the -6 dB width of the point scatterer response was found. The results are shown in Fig. 6.5(a). The -6 dB width is approximately proportional to the transducer diameter D, and decreases with increasing radius R. In Fig. 6.5(b), the -6 dB widths are plotted normalized with $D/(2R)$. It can be seen that although there are small individual differences, the -6 dB width is close to 0.92 $D/(2R)$ for all the focused points.

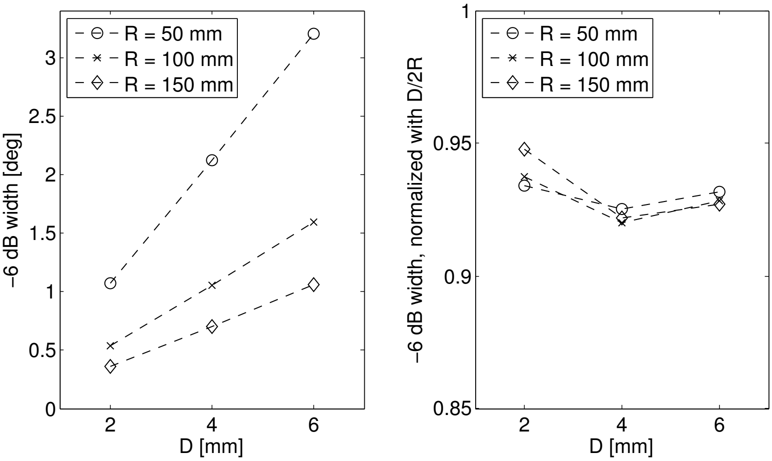

(a) Absolute width (b) Normalized width

Figure 6.5: Absolute and normalized width of point scatterers after focusing, for different transducer diameters D and scanning radii R.

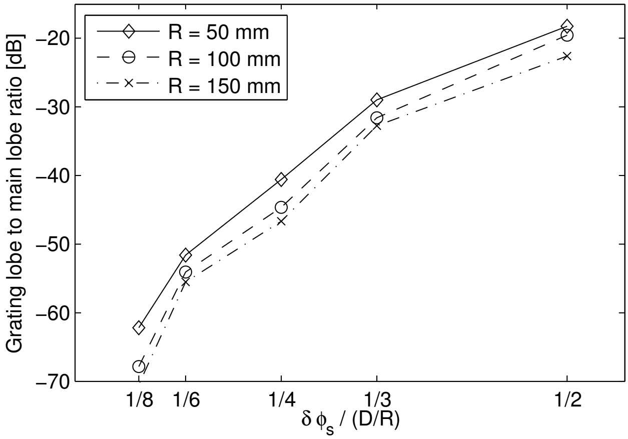

Figure 6.6: Ratio of grating lobe amplitude relative to main lobe amplitude, for different angular sampling intervals $\delta\phi_s$ and scanning radii R. The grating lobe amplitudes increase with increasing sampling interval, and are slightly higher for small scanning radii.

6.2.4 Effect of angular step size on grating lobe levels

In Section 6.1.4 it was suggested that if the step size along the ϕ axis is less than $D/(2R)$, the spatial sampling criterion will be satisfied, and grating lobes in the focused image can be avoided. However, the complete transducer beam pattern was not taken into account in the derivation, and in practice a smaller sampling interval may be required. A number of 2D simulations with a point scatterer and different angular step sizes were performed to study this further.

The simulations were conducted with a transducer with diameter $D = 5$ mm, scanning radii $R = [50, 100, 150]$ mm, and a point scatterer placed at 100 mm from the transducer. The raw data was sampled with angular sampling interval $\delta\phi_s = [\frac{1}{8}, \frac{1}{6}, \frac{1}{4}, \frac{1}{3}, \frac{1}{2}]$ times D/R, and for each simulation, the grating lobe levels were compared with the main lobe levels. The results are shown in Fig. 6.6. In general, the grating lobes grow in amplitude as the sampling interval increases. The grating lobes are also slightly higher for small scanning radii R. At $\delta\phi_s = D/(2R)$, the grating lobes are only approximately 20-25 dB below the main lobe, which is probably too high for most practical applications. A smaller sampling interval can be chosen according to the requirements of the individual application.

Examples of point scatterer responses for scans with $R = 100$ mm and three different angular sampling intervals are shown in Fig. 6.7. These illustrate how the grating lobes change in amplitude and shape as the angular sampling interval increases.

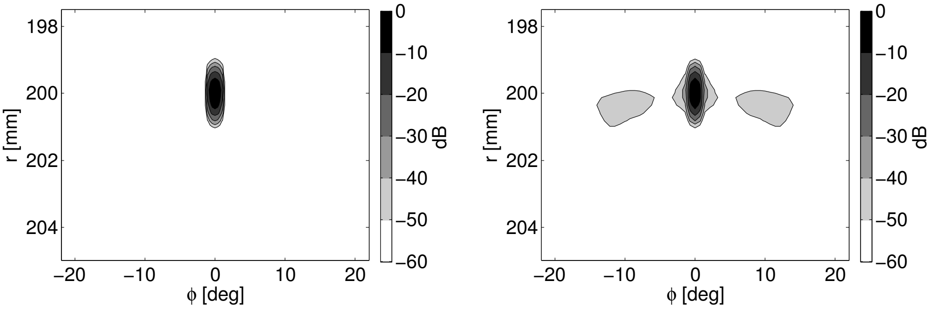

(a) $\delta\phi_s = D/8R$ (b) $\delta\phi_s = D/4R$

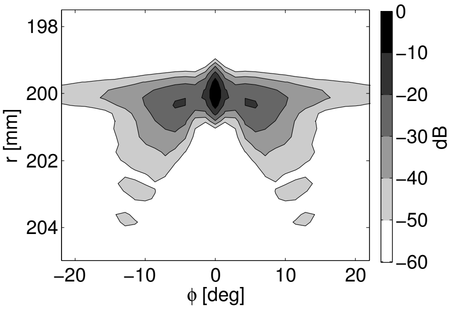

(c) $\delta\phi_s = D/2R$

Figure 6.7: Focused images of point scatterers, based on raw data acquired with different sampling intervals $\delta\phi_s$. Grating lobes are clearly visible in (b) and (c).

6.3 Point scatterer experiment

An experiment was performed to test the performance of the CPSM algorithm on real data. The experimental setup is shown in Fig. 6.8. Five small lead bullets, 2.5 mm in diameter, were used as point-like scatterers. The bullets were placed on 0.12 mm diameter nylon string, which was strung between two metal plates. The nylon string frame was put into a water tank, and the bullets were aligned at the same position along the z axis of the scanner, with a 30 mm horizontal and a 20 mm vertical offset between each bullet. Pulse-echo measurements were performed with a 1.5 MHz transducer with 5 mm diameter, with a scanning radius of $R = 62$ mm. The distance from the measurement surface was 82 mm to the closest bullet and 160 mm to the farthest bullet.

The raw 3D data set was processed by the CPSM algorithm, and the envelope for both the raw and the focused data set was calculated. Amplitude C-scans were generated by detecting the maximum envelope amplitude at each measurement position (ϕ, z), and these are shown in Figs. 6.9(a) and 6.9(c). In the raw data C-scan, the responses from the five scatterers are seen as five diffuse areas. In comparison, the C-scan for the focused data shows them as

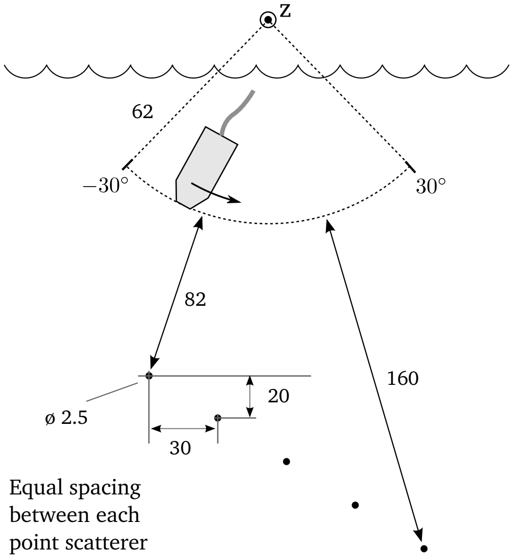

Figure 6.8: Experimental setup with point scatterers and cylindrically sweeped transducer. The z axis is perpendicular to the displayed plane, pointing towards the reader. All dimensions are in mm.

sharply defined, relatively small points. Note that for three of scatterers, the reflections from the nylon string can be seen as weak horizontal lines. Such lines are also present for the last two scatterers, but these are outside the displayed dynamic range.

2D slices centered on the bullets were extracted from each data set. The positions of the slices are indicated with dashed lines in the C-scans, and the raw and focused slices are shown in Fig. 6.9(b), and 6.9(d), respectively. The increase in lateral resolution after focusing is clearly visible. Note also that the main reflections from the lead bullets are followed by a tail of weaker echoes, which are probably caused by internal reverberation in the bullets.

To study the change in PSF after focusing, zoomed-in plots of the raw and focused response from the middle scatterer were made. The raw PSF, shown in Fig. 6.10(a), is curved and relatively broad, with a high amount of background noise. In comparison the focused PSF, shown in Fig. 6.10(b) is a round point with significantly increased signal-to-noise ratio. The beginning of the trailing echoes are seen below the main reflection. Note that these echoes also become narrower in the focused image.

The -6 dB width of each scatterer along the ϕ and z axes, denoted $\delta\phi$ and δz, was measured for both the raw and the focused image. The results are shown in Fig. 6.11. In Fig. 6.11(a), the widths are normalized with the theoretical expressions for the lateral resolution. For the raw data, δz increases

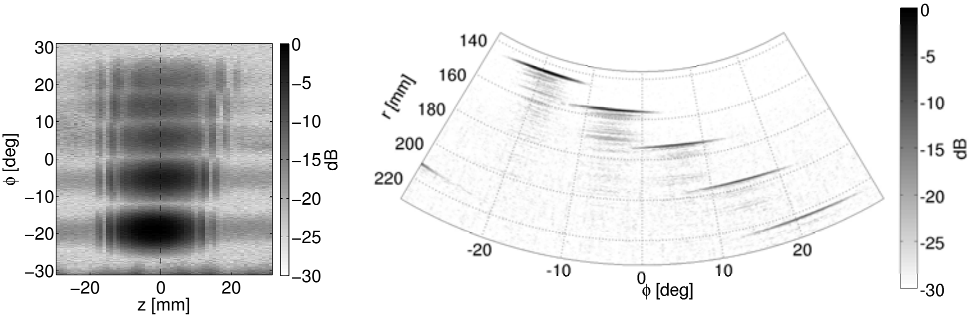

(a) Raw amplitude C-scan.

(b) Raw data slice from $z = 0$.

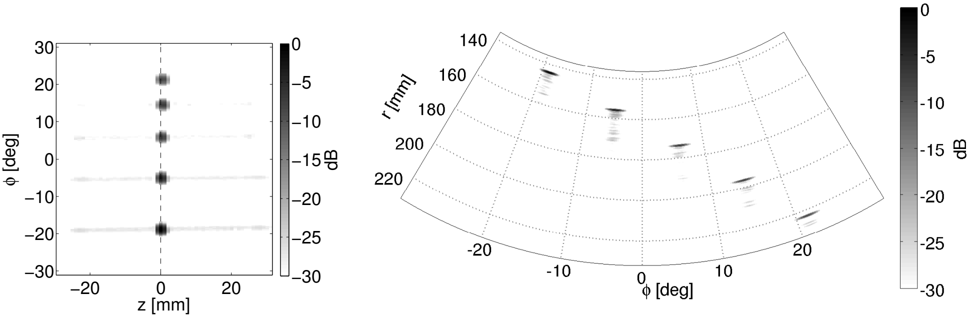

(c) Focused amplitude C-scan.

(d) Focused image slice from $z = 0$.

Figure 6.9: Comparison of C-scans and B-scan slices from raw and focused images of lead bullets. The position of the slices is indicated with dashed lines in (a) and (c).

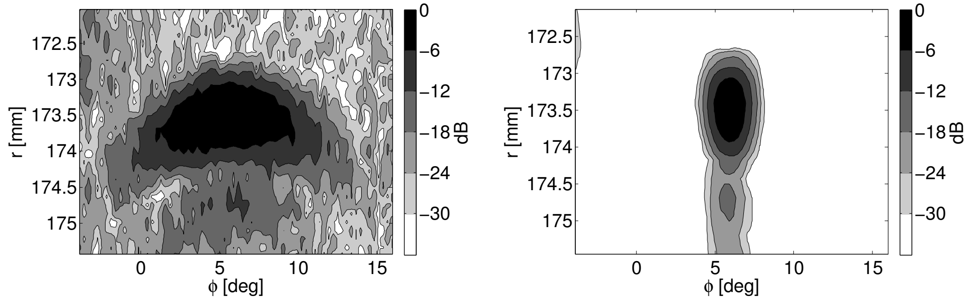

(a) Raw PSF

(b) Focused PSF

Figure 6.10: Point spread functions for middle scatterer before and after focusing.

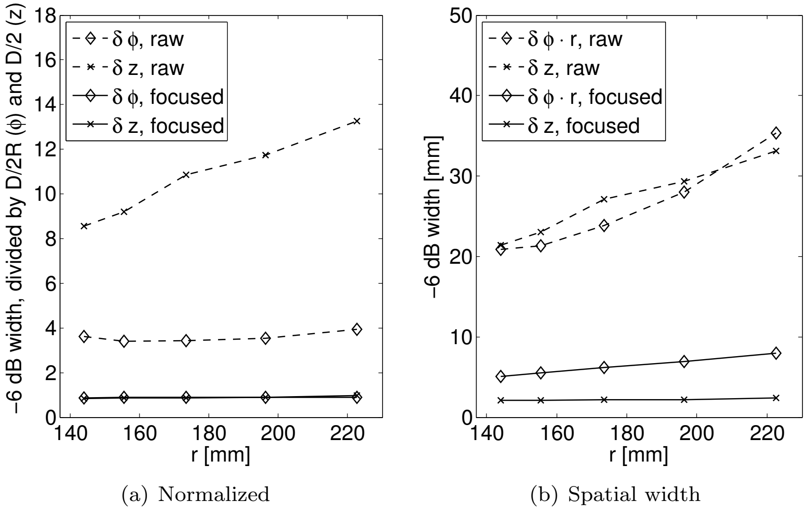

(a) Normalized (b) Spatial width

Figure 6.11: -6 dB widths of lead bullets in raw and focused images. In (a), the widths are displayed normalized with $D/2R$ for the ϕ axis and $D/2$ for the z axis. In (b), the z width is displayed without any normalization, and the ϕ width is multiplied with r, to show the spatial resolution.

with distance, from approximately 8 to 14, while $\delta\phi$ is at an almost constant level, slightly below 4. However, in the focused image the normalized $\delta\phi$ and δz are all in the range 0.85-1. This indicates that the resolution is close to that predicted by theory, independent of the distance to the transducer.

In Fig. 6.11(b), the spatial width of the point spread function is plotted in mm for both axes. For the ϕ axis, the spatial width at range r is given by the arc length width $\delta s = \delta\phi \cdot r$. The plot shows that in the raw image, δs and δz are very similar, increasing almost linearly from approximately 20 mm for the closest scatterer to 35 mm for the farthest. In the focused image, δs increases linearly from approximately 5 mm to 8 mm, while δz is constant at approximately 2-2.5 mm. The results show that there is a significant difference in resolution along the two scanning axes after focusing, and that the difference increases with distance.

Note that the experimental data was also processed with the approximate algorithm proposed in [Haun et al., 2002]. In contrast to the simulation presented in Section 6.2.2, the transducer beamwidth in the experiment was sufficiently narrow for the approximate transfer function to be accurate, and the results were therefore essentially the same as when the exact transfer function was used.

6.4 Discussion

In Sec 6.2.2 it was shown that the performance of the proposed CPSM algorithm can be better than that of the approximate algorithm presented in [Haun et al., 2002] when the ultrasonic beam is wide. Note, however, that the approximate transfer function in (6.9) may be simpler to implement in practice than the exact transfer function in (6.7), since complex exponentials are generally simpler to compute than Hankel functions. This will make a difference if the transfer function has to be calculated in real time. In order to speed up the CPSM algorithm while still retaining much of its accuracy, an accurate closed-form approximation to the Hankel function [Gardner and Collin, 2000] can be used. Since the transfer function is independent of the recorded data, it can also be precalculated and stored in lookup tables, removing the need for fast real-time calculation. Thus, the choice between using the exact or the approximate transfer function generally depends on the details of the implementation.

In Section 6.1.4 it was found that for a circular transducer of diameter D, the theoretical angular resolution after focusing is approximately $D/2R$. The simulations in Section 6.2.3 resulted in -6 dB widths of 0.92 to 0.94 times $D/2R$, which is relatively close. The experiment on point scatterers also yielded -6 dB widths close to the theoretical angular resolution, for both the ϕ and the z axis. Thus, the obtained resolution is close to the theoretical resolution for several different transducer diameters, scanning radii and target ranges. We therefore propose keeping $\delta\phi \approx D/2R$ and $\delta z \approx D/2$ as an approximate measure of the attainable resolution in practical applications.

In a synthetic aperture application, the spatial sampling interval should be small enough to keep the grating lobes below an acceptable level. The number of measurements should at the same time be kept at a minimum to avoid generating an unnecessarily large amount of data. The simulations in Section 6.2.4 showed that an angular sampling interval of $\delta\phi_s = D/4R$ resulted in grating lobe levels 40 to 50 dB below the main lobe, and we see this as a suitable compromise for practical applications. This is also consistent with the recommendation in [Gough and Hawkins, 1997] that the sampling interval for a linear scan with a transducer of length L should be $L/4$.

The cylindrical measurement geometry considered in this chapter is basically a combination of a circular scan and a linear scan, and the difference between these affects the size of the synthetic aperture along the two scanning axes. For a linear scan, the synthetic aperture grows in proportion with the distance to the image point, as discussed in Section 3.1 and shown in Fig. 3.2. This makes the lateral resolution along the linear scan axis constant in the whole imaged region. However, for a circular scan, the synthetic aperture size is not proportional with the distance to the image point. An illustration of the synthetic aperture formation for a circular scan is shown in Fig. 6.12. The size of the synthetic aperture is ultimately limited by the diameter of the scanning circle, and if the transducer is directional, the maximum synthetic aperture is even smaller. Thus, synthetic aperture focusing for circular scans can not provide a constant absolute lateral resolution, as for the linear scan, but rather provides a constant angular resolution.

The difference between the two scanning axes was demonstrated in the experiment in Section 6.3. The width of the synthetic aperture corresponds to the width of the PSF in raw data, and thus the difference in synthetic aperture size can be seen in Fig. 6.11(a); for the z axis, the width of the PSF increases with range, while for the ϕ axis, the width is approximately constant. Fig. 6.11(b) shows that as a result, the PSF width after focusing is constant for the z axis, while it increases with range for the ϕ axis. The expression for δs in (6.17) indicates that for cases where $r \gg R$, the difference in resolution between the two axes can become quite large. It is important to be aware of this difference in the design of practical imaging systems with cylindrical apertures.

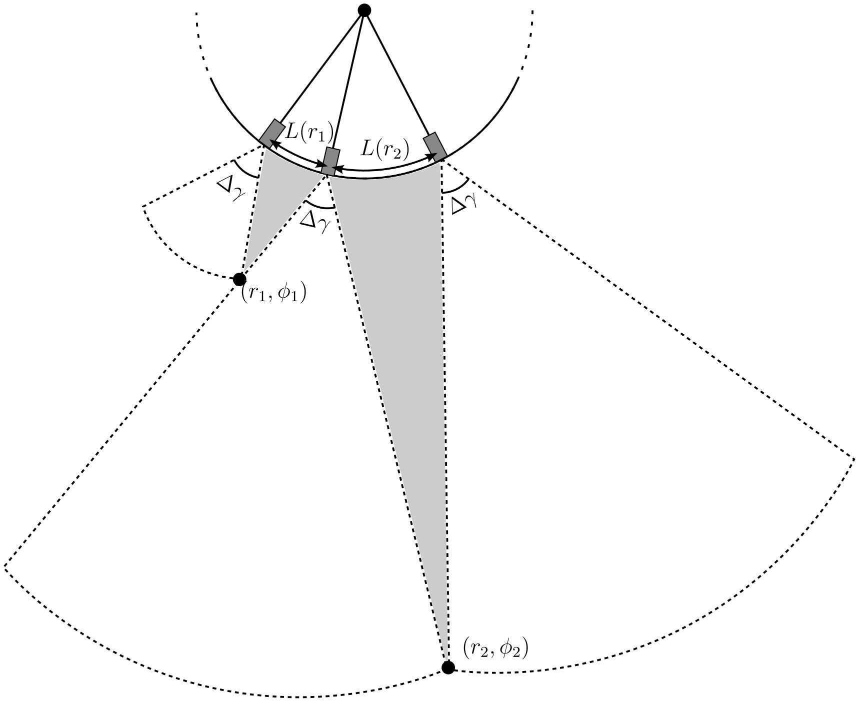

Figure 6.12: Synthetic aperture formation for circular scan. The size of the synthetic aperture, here denoted with $L(r)$, grows as the distance r to the imaging point increases. However, contrary to the linear scan case, L is not proportional to r. As r tends towards infinity, L tends towards a constant value.

6.5 Summary

In this chapter, we have presented an algorithm for synthetic aperture focusing of pulse-echo measurements performed over a cylindrical surface, called CPSM. The algorithm is based directly on the Fourier-domain solutions to the scalar wave equation in cylindrical coordinates, and in this sense the algorithm is exact. Comparison with a similar but approximate algorithm demonstrated that the proposed algorithm yields a higher resolution and lower sidelobes when the transducer beamwidth is large. We have also shown that for a circular transducer of diameter D, the attainable angular resolution after focusing is approximately $D/(2R)$, where R is the scanning radius. The attainable resolution along the z axis is approximately $D/2$, consistent with the lateral resolution for two-dimensional linear scan. By studying the effect of the angular sampling interval on grating lobes in the focused image, we found that a sampling interval of $D/(4R)$ or less should be sufficient in most applications.

Chapter 7

Application of CPSM in pipe inspection

In the previous chapter, we introduced a general algorithm for SAFT focusing of cylindrical scans, and in this chapter we apply it in imaging of pipes from the inside. Internal pipeline inspections are often performed using a robot traveling through the pipeline [Rajani and Kleiner, 2004; Eiswirth et al., 2000], and we assume here that the inspection system outlined in Fig. 1.4 is used.

The pipe geometry in Fig. 1.4 is well suited for a focused transducer, since the distance from the transducer to the pipe wall is constant and can be adjusted to fit the focal length. However, if the distance to the pipe wall changes during an inspection, the pipe wall will no longer be in the focal zone, and the lateral resolution will be poor. There are several scenarios in practical pipe inspection where this can occur, e.g. where the inspection robot meets an obstacle in the pipe, the pipe diameter changes, or there is a bend in the pipeline, as shown in Fig. 7.1(a), (b) and (c), respectively.

SAFT can be applied to scans performed with focused transducers, to improve the lateral resolution outside the focal zone. The focal point of the transducer is then treated as a small, virtual source [Passmann and Ermert, 1996; Frazier and O'Brien Jr., 1998; Haun et al., 2002]. For linear scans, the virtual source method can yield a lateral resolution comparable to the focal point, for all ranges [Frazier and O'Brien Jr., 1998]. In this chapter we adapt the CPSM algorithm to the virtual source method, and determine its lateral resolution.

The performance of the proposed method for pipe inspection is also evaluated through experiments on a severely corroded pipe. A comparison is made between a scan where the transducer is placed close enough for the pipe wall to be in focus, and another where the pipe wall is completely out of focus, with CPSM focusing applied in postprocessing.

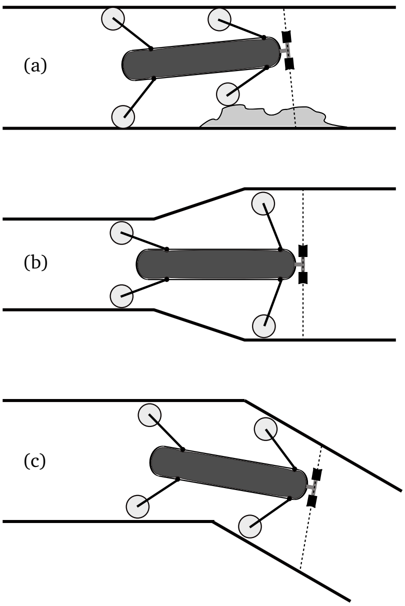

Figure 7.1: Distance from transducer to pipe wall changing during scan, due to a) an obstacle in the pipeline, b) the diameter of the pipeline changing, and c) a bend in the pipeline.

An additional experiment, performed with an unfocused transducer, is described in an appendix at the end of the chapter. In the experiment, CPSM imaging is applied for a number of simple, clearly defined shapes, yielding an intuitive demonstration of the focusing effect.

7.1 Theory

7.1.1 Virtual source

A focused transducer is made so that the time delay from all parts of the transducer to the focal point is equal. This creates an ultrasonic beam that is maximally focused at the focal distance F along the transducer axis, as shown in Fig. 7.2. The beam pattern produced by a focused transducer is different from that of a transducer with a flat aperture, and this has to be taken into account in SAFT algorithms for focused transducers.

In principle, the complete spatial impulse response of the transducer can be employed in the imaging process [Lingvall et al., 2003; Wennerström and Stepinski, 2007]. However, the derivation of SAFT algorithms for focused transducers can be simplified by assuming that the transducer focal point acts

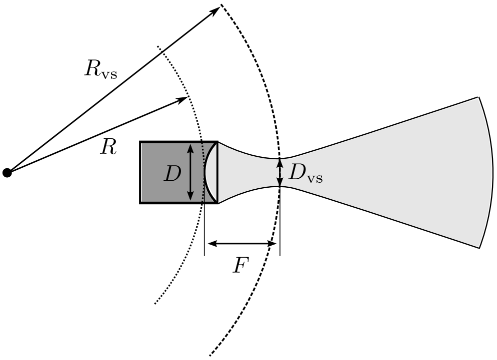

Figure 7.2: Focused transducer with diameter D moved along a circular arc of radius R. The focal point is treated as a virtual source with diameter D_{vs} moved along an arc of radius $R_{\mathrm{vs}} = R + F$.

as a virtual point source [Passmann and Ermert, 1996; Frazier and O'Brien Jr., 1998; Haun et al., 2002], and we will make the same assumption here. For the CPSM algorithm, this implies that the virtual source has an effective radius $R_{\mathrm{vs}} = R+F$, and an effective diameter D_{vs} that is smaller than the transducer diameter D, as shown in Fig. 7.2.

Since the focal point of the transducer is treated as the origin of the ultrasonic wave, the additional time delay between the transducer and the focal point has to be compensated for. For the pulse-echo case a negative time shift of $\Delta t = -F/\hat{c}$ should be applied, which in the Fourier domain corresponds to multiplication with the phasor $\exp(i\omega \cdot F/\hat{c})$. In addition, the system transfer function G has to be calculated with reference to the scanning radius of the virtual source, R_{vs}, rather then the real scanning radius R. A flowchart for the modified algorithm is shown in Fig. 7.3.

7.1.2 Lateral resolution

At the focal spot of a circular, focused transducer, the directivity function is approximately given by the jinc function in (2.10). The zeros to each side of the main lobe are given by $\sin\gamma = \pm 1.22\lambda/D$, where γ is the angle relative to the transducer axis of symmetry. We define the distance between the zeros as the effective diameter of the virtual source, and employing the small terms approximation $\sin\gamma \approx \gamma$ we obtain

$$D_{\mathrm{vs}} \approx 2.44\frac{\lambda F}{D}. \tag{7.1}$$

Approximate expressions for the lateral resolution after CPSM focusing are found by inserting R_{vs} and D_{vs} into (6.15), (6.16) and (6.17):

$$\delta\phi = D_{\mathrm{vs}}/(2R_{\mathrm{vs}}) \tag{7.2}$$

$$\delta z = D_{\mathrm{vs}}/2 \tag{7.3}$$

$$\delta s = \delta\phi \cdot r = \frac{D_{\mathrm{vs}}}{2} \cdot \frac{r}{R_{\mathrm{vs}}} \tag{7.4}$$

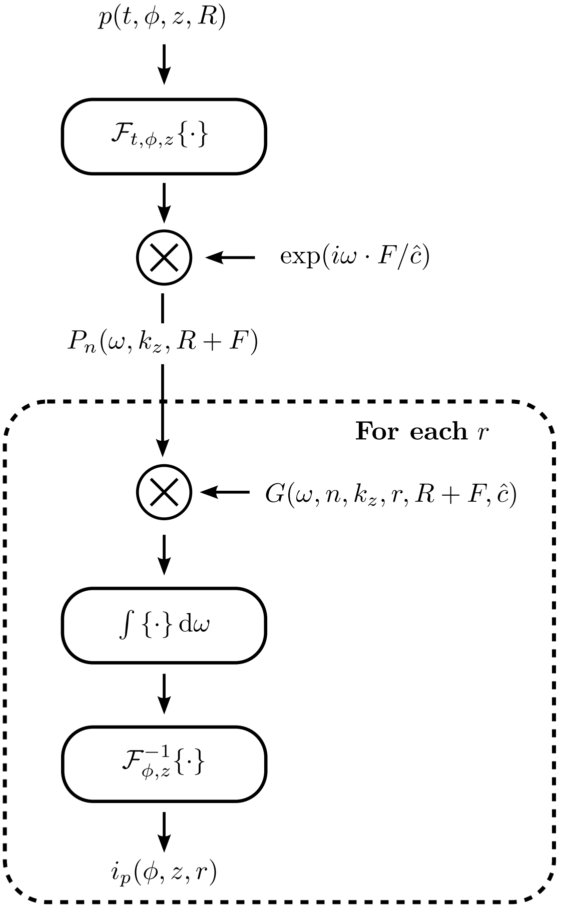

Figure 7.3: Algorithm flowchart for the CPSM algorithm, adapted to the virtual source method. Compared to the CPSM algorithm in Fig. 6.2, the modified algorithm requires an additional time shift $\exp(i\omega \cdot 2F/c)$, and uses the virtual source radius $R_{\mathrm{vs}} = R + F$ in the calculation of G.

7.2 Experiments

7.2.1 Experimental setup

Ultrasonic pulse-echo measurements were performed with a scanner made for moving a transducer along a cylindrical surface. The object under inspection was placed in a water tank, and the scanner was placed above the tank, so that the scanner arm and the transducer was submerged in water. The transducer was 12.7 mm in diameter, with a center frequency of 2.25 MHz and a focal length of approximately 20 mm.

Raw ultrasonic data was processed with the CPSM algorithm, as described in Section 7.1. The envelope of the image was calculated by taking the absolute value of the complex data produced by the algorithm. Similarly, the envelope of raw data was obtained by first applying the Hilbert transform along the time axis, and then taking the absolute value of the resulting analytic signal.

7.2.2 Point scatterer experiment

An experiment on point-like scatterers was performed to determine the size and shape of the point scatterer response before and after CPSM focusing. 1.5 mm thick steel wires were used as scatterers, and 2D scans were performed along

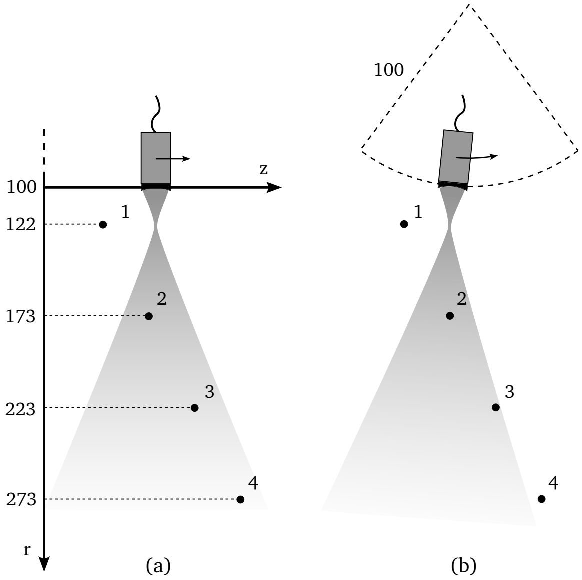

Figure 7.4: Experimental setup for scan of wire targets. a) Scan along z axis. b) Scan along ϕ axis. The scatterers are numbered 1 to 4 with increasing distance to the transducer.

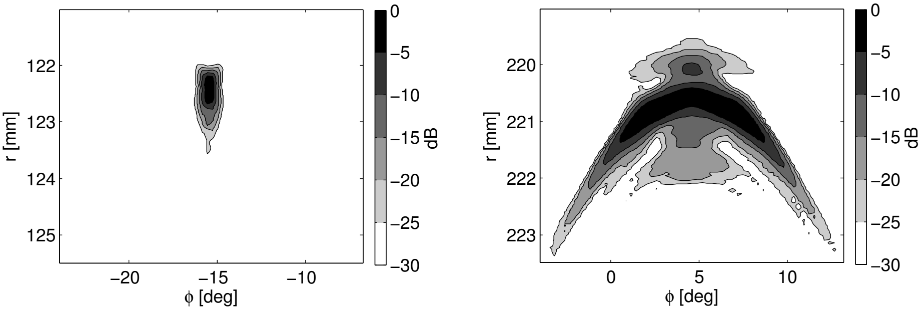

(a) Raw data PSF, scatterer 1

(b) Raw data PSF, scatterer 3

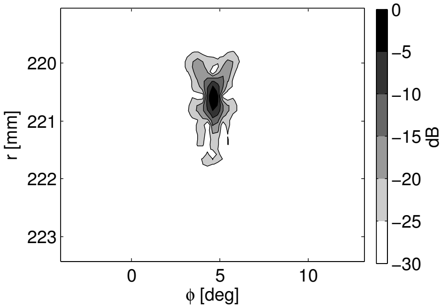

(c) Focused PSF, scatterer 3

Figure 7.5: Example point spread functions from angular scan of wire targets. Scatterer 1 is located in the focal zone of the transducer, while scatterer 3 is located far beyond the focal zone.

both the ϕ and z axis, with the wires placed perpendicular to the scanning direction, as shown in Fig. 7.4. The scanning radius R was 100 mm.

Due to the divergence of the transducer beam beyond the focal zone, the width of the raw data PSF increases rapidly with the range r. This is clearly seen in Fig. 7.5(a) and 7.5(b), which shows the angular scan PSF for scatterer number 1 and 3, located approximately 22 and 123 mm from the transducer, respectively. Scatterer number 1 is inside the focal zone of the transducer, and thus the PSF is small and well focused. In contrast, the PSF from scatterer number 3 is curved and relatively broad. There are also some additional artifacts present above and below the curve of the main reflection. These artifacts were not present in the experiment in Section 6.3, in which an unfocused transducer was used, and it is assumed that they are due to edge waves from the focused transducer [Djelouah et al., 1991; Wennerström and Stepinski, 2007]. Figure 7.5(c) shows the PSF of scatterer 3 after CPSM focusing. The focusing effect is clearly visible, and the width of the response is similar to that of scatterer 1. However, the artifacts observed in the unfocused

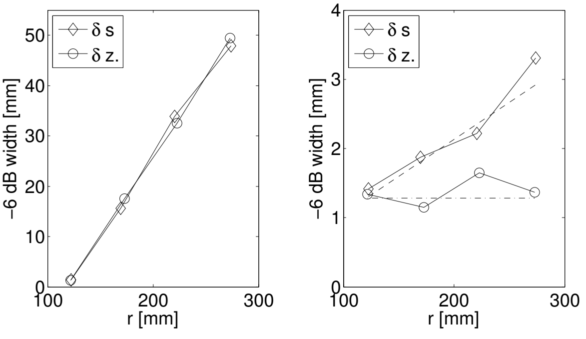

(a) Raw (b) Focused

Figure 7.6: -6 dB width of point scatterers along both scanning axes. Note that the y-axis limits are different in the two plots. In (b), the theoretical resolution is indicated with a dashed and a dash-dot line for δs and δz, respectively.

PSF seem to also affect the focused PSF, creating sidelobes which widen the response at low amplitudes.

The -6 dB widths of the PSFs, denoted $\delta\phi$ and δz, were measured for all the scatterers. $\delta\phi$ was multiplied with the range r of each scatterer, to produce the arc length resolution δs. The raw data results are plotted in Fig. 7.6(a), showing that before focusing, δs and δz are very similar. In the focal region δs and δz are small, approximately 1.3-1.4 mm, but both increase rapidly with increasing transducer-scatterer distance, up to approximately 50 mm for the furthermost scatterer. In comparison, Fig. 7.6(b) shows that CPSM focusing significantly reduces δs and δz for all scatterers outside the focal region. δs increases approximately linearly with distance, from 1.4 mm up to approximately 3.4 mm for the furthermost scatterer, while δz is in the range 1.2–1.6 mm for all scatterers. The theoretical resolution after focusing is shown together with the measurements, plotted as a dashed and a dash-dot line for δs and δz, respectively. The theoretical resolution was calculated using (7.1), (7.3) and (7.4), with $\lambda = c/f_c$, where f_c denotes transducer center frequency. The correspondence between measurements and theoretical resolution is seen to be relatively good for both axes.

7.2.3 Corroded pipe experiment

In the second experiment a section of cast iron pipe with severe corrosion damage was scanned. The complex and irregular surface of the pipe was chosen as a test case to demonstrate the performance of CPSM focusing with a virtual source in a practical application. The pipe was originally part of a water pipeline in Skien, Norway, and was in service from 1883 to 2009. The inner diameter of the pipe was originally approximately 360 mm. When the pipe was dug up, it was sandblasted to reveal the underlying pitting damage. A picture

Figure 7.7: Photograph of interior surface of pipe section. The four screws used as reference points are indicated with white rings.

of the section is shown in Fig. 7.7. The photo was taken with a light source placed low, to the right of the pipe, to create shadows revealing the structure of the surface. Four small holes were drilled through the pipe, and machine screws were placed in the holes to act as reference points. The placement of the screws is indicated by white rings.

To obtain an independent estimate of the surface topography of the pipe, a stereo vision depth estimation technique was employed. Two images of the pipe surface were taken, with a lateral displacement ("baseline") of $b = 70$ mm, using a Nikon D40 camera and a lens with focal distance $f = 18$ mm. The images were corrected for lens distortion using J.-Y. Bouget's Camera Calibration Toolbox for Matlab [Bouget, 2010], and subsequently rectified and stereo matched using Peter Corke's Machine Vision Toolbox [Corke, 2011a,b]. The stereo matching produces a map of the relative displacement of pixels between the images, the disparity d, which is related to the distance z_c from the camera by the equation

$$z_c = \frac{fb}{\rho d}, \tag{7.5}$$

where ρ is the pixel side length [Corke, 2011b]. To remove the effect of the pipe curvature on the depth image, a 2nd-degree polynomial surface was fitted to the depth map and subsequently subtracted from it. Finally, a 3x3 mm median filter was applied to remove erroneous outliers. The resulting surface topography map is shown in Fig. 7.9(a). A number of large pits, identified by bright spots, are clearly seen. Comparison with Fig. 7.7 shows that all the fine detail may not be incorporated in the stereo vision topography plot, but that the location and shape of the largest pits is accurately imaged.

Two ultrasonic scans of the pipe were performed; one where the scanning radius was set to 160 mm, so that the pipe surface was in the transducer focal

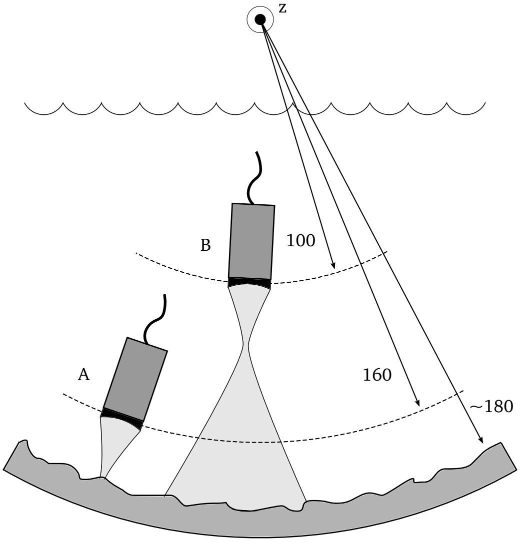

Figure 7.8: Experimental setup for cylindrical scan of pipe section. The z axis is perpendicular to the displayed plane, pointing towards the reader. Scan A: Transducer scanned at 160 mm radius, pipe surface in focal zone of transducer. Scan B: Transducer scanned at 100 mm radius, pipe surface far beyond focal zone.

zone, and another with a 100 mm scanning radius, where the pipe surface was far beyond the focal zone. The scans were labeled scan A and B, respectively, as shown in Fig. 7.8.

The topography of the pipe was then estimated from three different data sets: Scan A, which is inherently focused, scan B without CPSM focusing, and scan B with CPSM focusing. For each data set, the range r to the pipe surface was estimated by detecting the maximum envelope value in each measurement position (ϕ, z). We will refer to the resulting 2D data sets as topography C-scans. The mean range was subtracted from each C-scan, revealing mm-scale topography variations, and a 3x3 mm median filter was applied to remove a few erroneous estimates. The results are shown in Fig. 7.9(b)-(d).

To illustrate the appearance of the data in the range dimension, a 2D slice was also extracted from each 3D data set. The slice positions are indicated with dashed lines in Fig. 7.9(b)-(d), and the slices are shown in Fig. 7.10.

Comparing Fig. 7.9(b) with Fig. 7.9(a), it is seen that scan A yields a topography map very similar to that of the stereo vision technique. Since the two topography estimates are independent, the similarity is an indication that both are relatively accurate. The slice from scan A, shown in Fig. 7.10(a), shows that the reflection from the pipe surface is clearly defined, and smoothly changing with lateral offset z.

Without focusing, scan B yields a topography estimate where the pits have

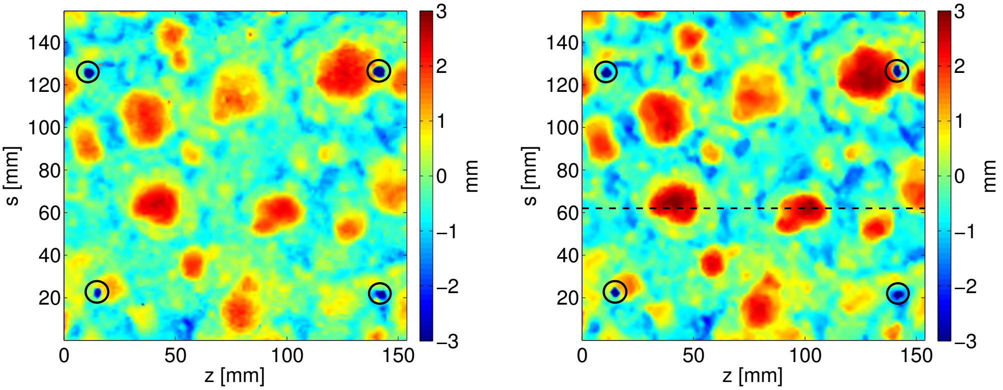

(a) Stereo vision (b) Ultrasound, Scan A

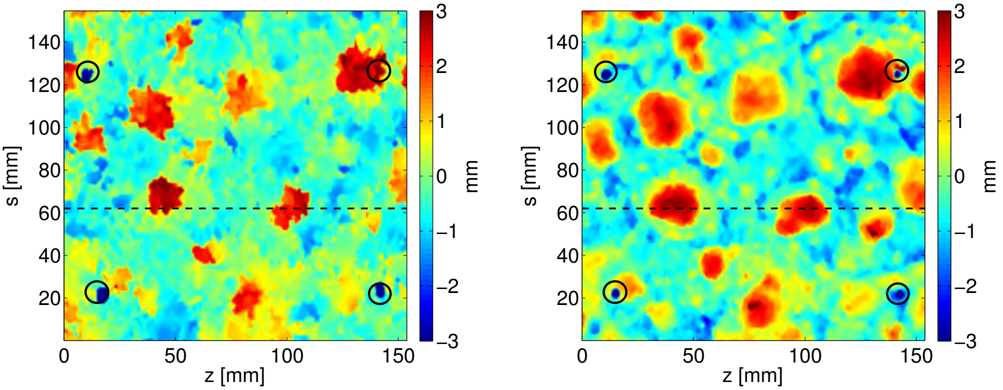

(c) Ultrasound, scan B, raw (d) Ultrasound, scan B, focused

Figure 7.9: Topography of pipe surface estimated with stereo vision and ultrasound scans. Reference points indicated are with white rings, and the position of the slices shown in Fig. 7.10 are indicated with dashed lines in (b)-(d).

a very irregular shape, as seen in Fig. 7.9(c). The reason for this is clearly seen in the slice plot in Fig. 7.10(b): Since the pipe wall is outside the focal zone, reflections from different parts of the pipe are smeared together laterally. Because of this smearing, there is no clearly defined reflection from the pipe surface, and the estimation of the topography is less accurate. Note for example that the two largest pits appear smaller than they really are.

Applying CPSM focusing to scan B yields a significant improvement of the topography C-scan, as seen in Fig. 7.9(d). Comparison with Fig. 7.9(b) shows that the accuracy of the topography estimation is similar that of scan A. This impression is confirmed by the slice plot in Fig. 7.10(c), which is similar to the slice plot from scan A in Fig. 7.10(a). The surface reflection appears slightly more irregular, and there are some additional echoes below the surface

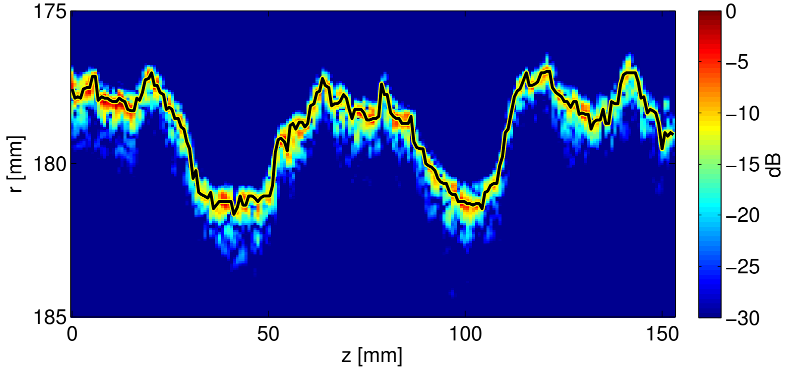

(a) Scan A

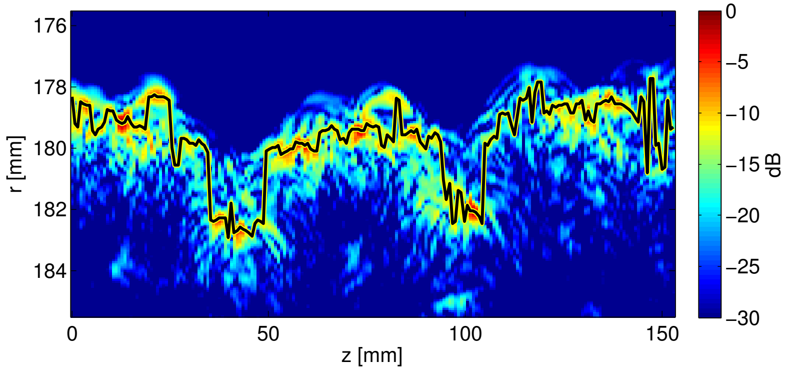

(b) Scan B, unfocused

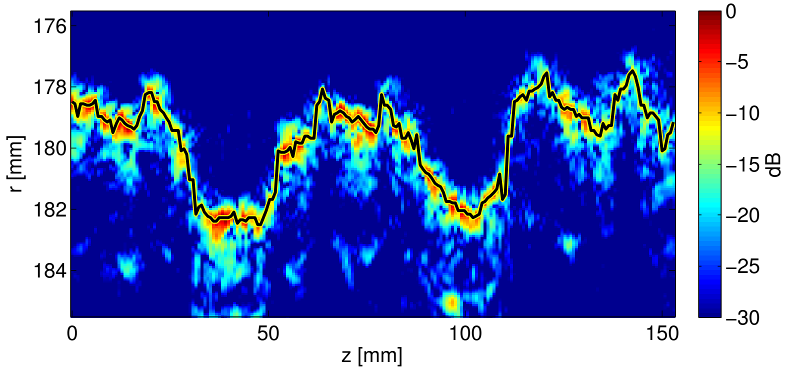

(c) Scan B, focused with CPSM

Figure 7.10: Slices from ultrasound scans, taken at s $\approx$ 60 mm, as indicated with dashed lines in Fig. 7.9(b)-(d). The topography estimated from the maximum envelope amplitude is indicated with a black line.

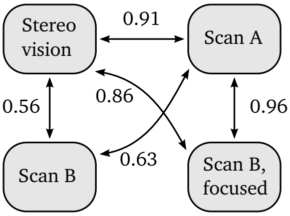

Figure 7.11: ZNCC similarity measure between the four different topography estimates. A value of 1 indicates a perfect match.

reflection, but the improvement from Fig. 7.10(b) is clear.

To quantify the similarity between the different topography C-scans, the zero-mean normalized crosscorrelation (ZNCC) between them was calculated. ZNCC normalizes the pixel values of the images so that any shift or difference in scale is removed, and only the shapes are compared [Corke, 2011b]. A ZNCC value of 1 indicates a perfect match. The results are summarized in Fig 7.11. The unfocused version of scan B has a ZNCC of 0.56 and 0.63 with the stereo vision and scan A topography estimates, respectively. In comparison, the focused version of scan B has a corresponding ZNCC match of 0.86 and 0.96, confirming that focusing significantly improves the topography estimation.

7.3 Discussion

The point scatterer experiment presented in Section 7.2.2 demonstrated that CPSM processing can significantly improve the lateral resolution outside the focal region of a focused transducer. The results also corresponded well with the expressions for theoretical resolution derived in Section 7.1.2.

The discussion on resolution and synthetic aperture size in Section 6.4 is also valid for the modified algorithm in this chapter. From (7.3) and (7.4) we find that the ratio of the arc length resolution to the z resolution is $\delta s/\delta z = r/R_{\text{vs}}$, and for $r \gg R_{\text{vs}}$, the difference in resolution is large. However, for scan B in the pipe imaging experiment in Section 7.2.3, the ratio r/R_{vs} was approximately 1.5, and thus the resolution along the two axes was relatively similar.

In the previous chapter it was found that for an unfocused transducer with diameter D, the angular resolution along the z and ϕ axis is approximately $D/2$ and $D/(2R)$, respectively. Thus, to achieve a high resolution with an unfocused transducer, the transducer diameter should be as small as possible. However, small transducers generally yield a low signal-to-noise ratio (SNR). Using a relatively large, focused transducer to create a small virtual source, as we have in this chapter, we obtain both a relatively high SNR and a high lateral resolution. This makes the proposed virtual source method well suited for practical applications.

The experiment in Section 7.2.3 demonstrated the use of CPSM focusing in a pipe inspection scenario. The two scans of the pipe surface yielded topography maps of approximately the same quality, even though one of the scans was performed with the pipe wall was far beyond the transducer focal region. Although the experiment is not representative for all pipe inspection scenarios, it demonstrates that CPSM can increase the range within which the transducer yields a high resolution. Thus, CPSM focusing can be applied to improve the lateral resolution in cases where the distance between the transducer and the pipe wall changes, for example where the pipe diameter increases or the inspection robot is imperfectly centered in the pipe.

In both this and the preceding chapter, we have assumed that the pipe inspection is performed with a single, rotating transducer. However, full angular coverage could also be achieved by using a circular array transducer. If the array is used to emulate a transducer with a fixed focus depth, the virtual source method described in this chapter can be used in the same way as for a physically focused transducer.

7.4 Summary

In this chapter we have adapted the CPSM algorithm for use with a focused transducer, by treating the focal point of the transducer as a virtual source. We have shown, through experiments on point-like scatters, that the modified algorithm significantly extends the range in which the focused transducer produces a high lateral resolution. A theoretical expression for the attainable lateral resolution was suggested, based on the effective size and scanning radius of the virtual source, and this was found to correspond well to the lateral resolution achieved in experiments. Some low-amplitude artifacts were observed in the focused images of point scatterers, but these were probably caused by edge waves from the focused transducer, and not the CPSM algorithm itself. The algorithm was also applied in a pipe inspection experiment, to focus a 3D scan of a severely corroded pipe. It was shown that with CPSM focusing, the surface topography of the pipe could be estimated with high resolution, even if the transducer was placed several focal lengths away from the pipe surface.

7.A Imaging of metal objects in pipe

In this appendix, we describe an additional experiment with surface topography estimation in a pipe geometry. The experiment was not performed with a focused transducer and was therefore not included in the main body of the chapter. However, it is included here because it gives an intuitive demonstration of the effect of CPSM focusing, for a number of objects with clearly defined shapes.

7.A.1 Experimental setup

A section of 300 mm diameter pipe was placed in a tank, and four different metal objects were arranged on the inside surface of the pipe. The objects, a key, a tuning fork, a drum tuning key, and a ring, are shown in Fig. 7.12(a). A cylindrical scan of the objects in the pipe was performed using a 1.5 MHz transducer with a 5 mm diameter, mounted on a carriage with a rotating arm. The carriage was placed on a linear rail above the water tank, and adjusted to make the rotation axis for the arm coincide with the center of the pipe. The scanning radius of the transducer, R, was 58 mm. A schematic of the experimental setup is shown in Fig. 7.12(b).

The raw data was processed with the CPSM algorithm. Amplitude C-scans were made for both the raw and focused data sets, by detecting the maximum envelope value for all r less than the pipe radius. The pipe surface was excluded from the maximum search because this was found to produce a less cluttered image of the objects. The maxima positions were also used to create topography C-scans for both data sets. In positions where the amplitude C-scan was below -20 dB, there was no significant echo from the objects, and the topography

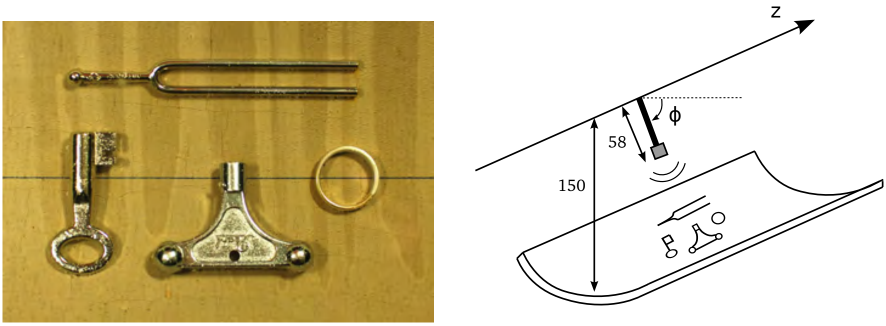

(a) (b)

Figure 7.12: Experimental setup with metal objects placed in a section of pipe. (a) The objects, clockwise from top: A turning fork, a ring, a drum tuning key, and a regular key. (b) Cylindrical scan geometry.

range was set equal to the pipe radius.

7.A.2 Results

The amplitude and topography C-scans are shown in Fig. 7.13. In order to make the units on both axes equal, the arc length on the pipe surface is plotted on the vertical axis, rather than the angular coordinate ϕ. The arc length is given by $s = \phi \cdot r_{\text{pipe}}$, where r_{pipe} denotes the inner radius of the pipe.

The raw amplitude C-scan in Fig. 7.13(a) clearly shows the lateral smearing effect caused by the wide transducer beam. For example, the sharp edges of the ring are imaged as a round, diffuse area. Note also the local maxima and minima in the image of the turning fork. This effect is probably caused by interference between reflections from the two arms. The raw topography C-scan in Fig. 7.13(b), suffers from the same smearing effect as Fig. 7.13(a), making interpretation of the shapes difficult.

In the amplitude C-scan for the focused image, shown in Fig. 7.13(c), the lateral resolution is significantly better than in Fig. 7.13(a). The shape of the ring is clearly defined, and the two arms of the tuning fork are well separated. Note, however, that some parts of the objects are hardly visible, for example parts of the key on the left, and the three end points of the drum tuning key. In these areas, the objects are curved or tilted relative to the cylindrical measurement plane, and thus the amount of energy reflected back towards the transducer is small.

Finally, Fig. 7.13(d) illustrates how focusing also improves the topography estimation, yielding an accurate image of the range to each object. Note for example that the edge of the drum tuning key, slightly elevated from the rest of the key, is clearly visible.

The results of the cylindrical scan can be combined into a single 3D surface image, in which the color and shape of the surface is given by the amplitude and topography C-scan, respectively. This mode of plotting enables an intuitive and simple interpretation of the 3D data. Surface images for the raw and focused data set are shown in Fig. 7.14.

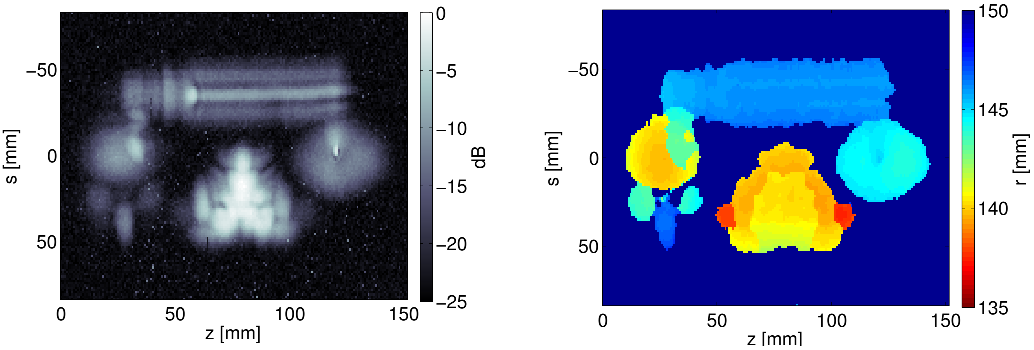

(a) Amplitude C-scan, raw data (b) Topography C-scan, raw data

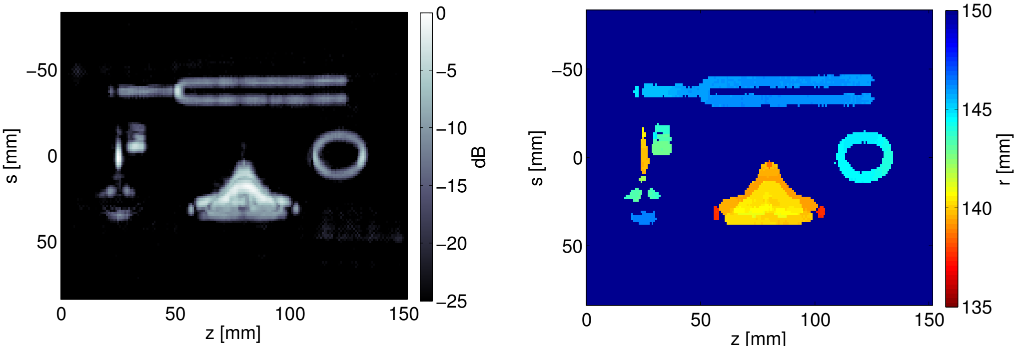

(c) Amplitude C-scan, image (d) Topography C-scan, image

Figure 7.13: Amplitude and topography C-scans of metal objects in pipe.

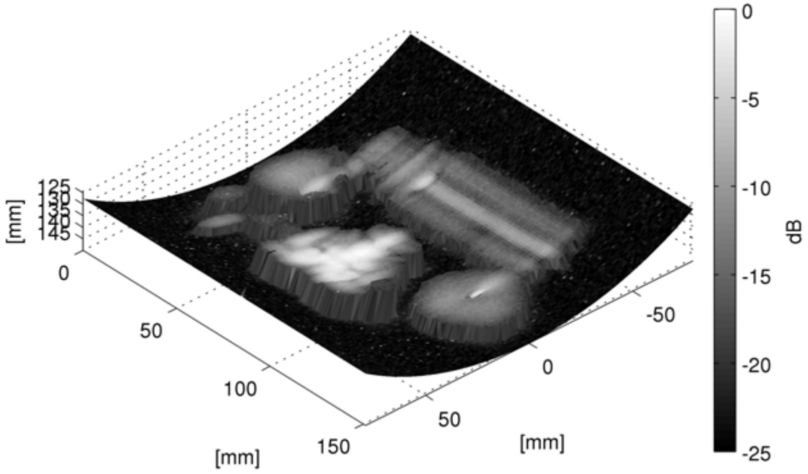

(a) Raw data surface plot

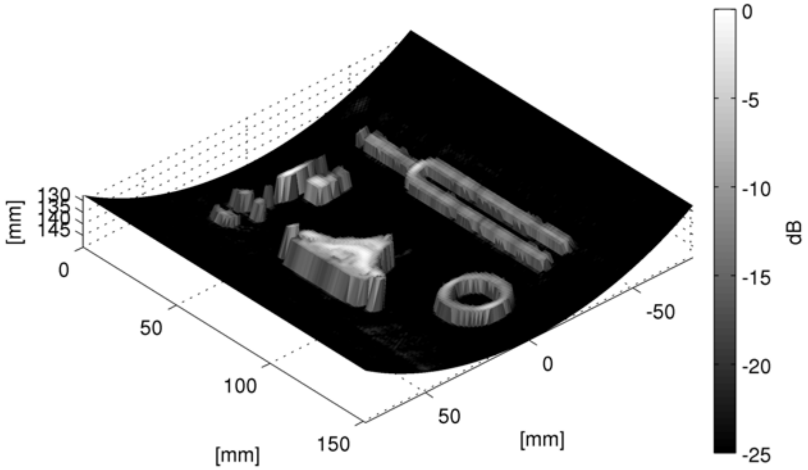

(b) Focused image surface plot

Figure 7.14: Surface plots for raw and focused images of metal objects in pipe. The objects are colored according to the backscattered amplitude (Figs. 7.13(a) and 7.13(c)), and shaped according to the estimated topography (Figs. 7.13(b) and 7.13(d))

Chapter 8

Multilayer imaging in cylindrical geometries

In Chapter 6, we described an algorithm for synthetic aperture imaging with cylindrical apertures, assuming a constant wave velocity. This assumption is valid for imaging in media where there are only small variations in the wave velocity, for example inside the the human body. The assumption is also valid for imaging of the inside topography of a pipe, as demonstrated in Chapter 7, since the liquid in the pipe is the only propagating medium. However, for accurate imaging of defects inside the pipe wall, or corrosion damage on the outside of the wall, the SAFT algorithm must treat the wall as a separate layer.

In this chapter we therefore expand the CPSM algorithm to the case of multiple concentric layers. The modification for multilayer imaging is similar to that of 2D linear scans described in Section 4.2. A ray-tracing model for two-layer simulations is presented, and the multilayer CPSM algorithm is demonstrated for both simulated and real data. It is shown that the single-layer CPSM algorithm yields images which are increasingly defocused as the range inside the second layer increases, while the multilayer algorithm maintains a high, approximately constant lateral resolution.

8.1 Theory

We assume here that the measurement geometry consists two or more concentric layers, as shown in Fig. 8.1. The transducer is scanned over a cylindrical surface given by a constant radius R_1, and the interfaces between the layers are labeled R_2, R_3, ... R_L, where L is the total number of layers. Similarly, the wave velocities of the layers are labeled c_1, c_2, ..., c_L.

The recorded pulse-echo wave field is denoted $p(t, \phi, z, R_1)$, and the corresponding Fourier transformed wave field is denoted $P_n(\omega, k_z, R_1)$. In

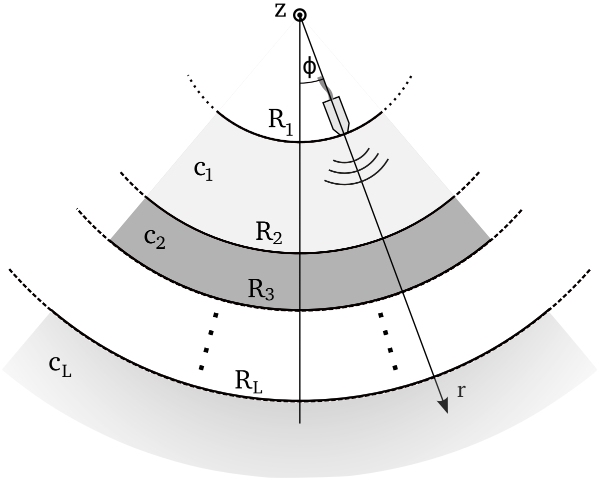

Figure 8.1: Illustration of geometry with concentric layers. The z axis is perpendicular to the page, pointing towards the reader.

Section 6.1.2 it was shown that the wave field can be extrapolated between two arbitrary ranges r_1 and r_2 by multiplication with the transfer function G,

$$P_n(\omega, k_z, r_2) = P_n(\omega, k_z, r_1) \cdot G(\omega, n, k_z, r_1, r_2, \hat{c}), \tag{8.1}$$

where G is given by

$$G(\omega, n, k_z, r_1, r_2, \hat{c}) = \frac{H_n^{(2)}(r_2\sqrt{(\omega/\hat{c})^2 - k_z^2})}{H_n^{(2)}(r_1\sqrt{(\omega/\hat{c})^2 - k_z^2})} \ . \tag{8.2}$$

From here on, we will simplify the notation of G by omitting the ω, n and k_z terms, writing $G(\omega, n, k_z, R_1, r, \hat{c})$ as $G(r_1, r_2, \hat{c})$.

We assume now that we want to extrapolate the wave field from R_1 to an arbitrary range r_l in layer l, where $l \in [1, 2, \ldots, L]$. The wave field must first be extrapolated through the preceding layers, up to the interface R_l, and then be extrapolated from R_l to r_l:

$$\begin{aligned} &P_n(\omega, k_z, r_l) = \\ &\quad P_n(\omega, k_z, R_1) \cdot \underbrace{\prod_{m=1}^{l-1} \Big[G(R_m, R_{m+1}, \hat{c}_m) \Big]}_{\text{Extrap. from } R_1 \text{ to } R_l} \cdot \underbrace{G(R_l, r_l, \hat{c}_l)}_{\text{Extrap. from } R_l \text{ to } r_l} \ . \end{aligned} \tag{8.3}$$

Using the expression in (8.3) to extrapolate the wave field, it is possible to perform imaging in the same way as for the single layer case, as described in Section 6.1.3. The imaging algorithm is summarized in Fig. 8.2. The recorded pulse-echo wave field is Fourier transformed to obtain $P_n(\omega, k_z, R_1)$, and then, for every layer l, it is extrapolated from R_1 to R_l by multiplication with $\prod_{m=1}^{l-1}\left[G(R_m, R_{m+1}, \hat{c}_m)\right]$. No such extrapolation is needed for the case $l = 1$, but to simplify the figure, this is not shown as a special case. For all ranges r_l within the layer, the wave field is then extrapolated from R_l to r_l, integrated over ω, and inverse Fourier transformed, yielding the focused image plane $i_p(\phi, z, r_l)$.

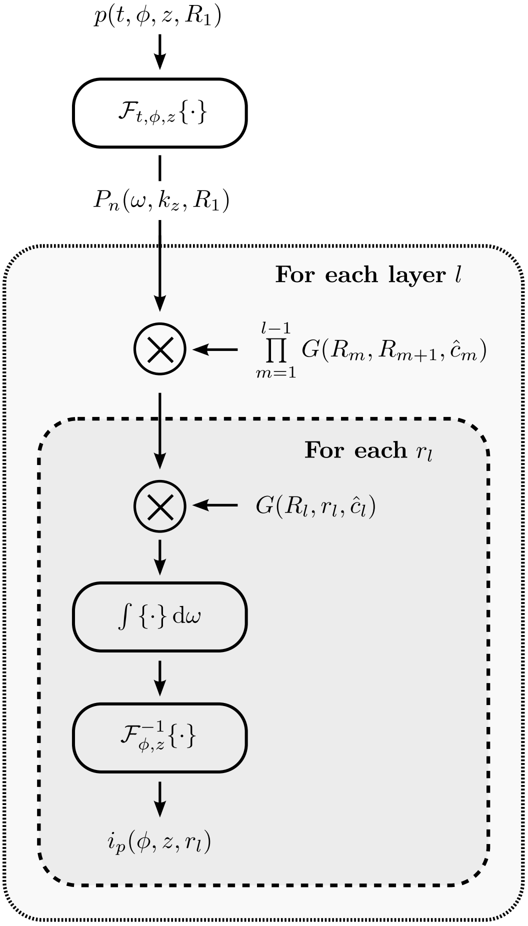

Figure 8.2: Flowchart for the multilayer CPSM algorithm. The pulse-echo wave field is Fourier transformed and extrapolated from R_1 to r_l, via multiplication with transfer functions for each layer. A focused image plane $i_p(\phi, z, r_l)$ is obtained by integration over ω and inverse Fourier transformation.

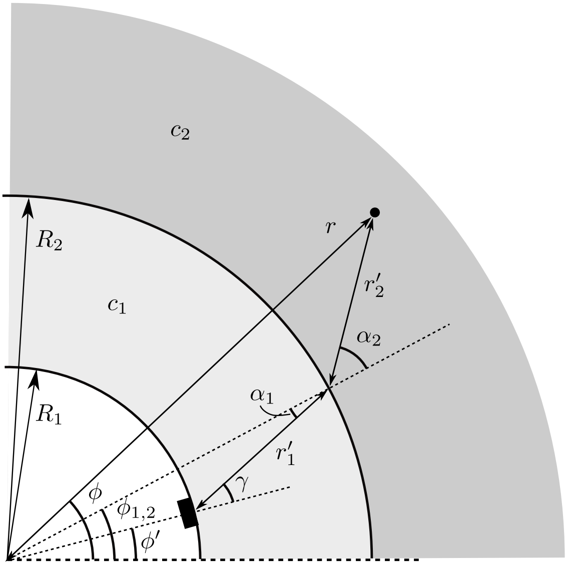

Figure 8.3: Geometry used in simulations of ultrasound scan in two concentric layers. The transmitted and back-scattered wave is refracted at the point $(R_2, \phi_{1,2})$ on the interface between the two layers.

8.2 Numerical simulation model

A numerical simulation model was developed to test the proposed algorithm. The model is presented for a two-layer structure only, but can be extended to an arbitrary number of layers following the same principles. The simulations are limited to two-dimensional, circular scans, as in Chapter 6.

8.2.1 Geometry

The two-layer geometry is shown in Fig. 8.3. The transducer position is given by coordinates (R_1, ϕ'), and we consider transmission of a wave between the transducer and a point scatterer in the second layer, given by coordinates (r, ϕ). The wave is refracted at the interface between the two layers, at a point given by $(R_2, \phi_{1,2})$. The distance from the transducer to the refraction point is denoted r'_1, and the distance from the refraction point to the point scatterer is denoted r'_2. The angle relative to the surface normal in layer 1 is denoted α_1, and the corresponding angle in layer 2 is denoted α_2.

The path between the transducer and the scatterer can be computed numerically using Fermat's principle, which states that the path taken by a wave between two points is the path that can be traversed in the least time. Such ray tracing is exact only at the limit of infinitely small wavelength, but accurate enough to be applied in simulations of seismic and ultrasonic measurements in inhomogeneous media [Margrave, 2003; Shlivinski and Langenberg, 2007]. The propagation paths in each medium are given by the law of cosines;

$$r_1' = R_1^2 + R_2^2 - 2R_1R_2 \cdot \cos(\phi_{1,2} - \phi'), \tag{8.4}$$

$$r_2' = r^2 + R_2^2 - 2rR_2 \cdot \cos(\phi - \phi_{1,2}), \tag{8.5}$$

and the total propagation time is

$$t = \frac{r_1'}{c_1} + \frac{r_2'}{c_2}. \tag{8.6}$$

When the point of refraction, $\phi_{1,2}$, is known, all other variables are also known. We therefore apply Fermat's principle to (8.6) to find $\phi_{1,2}$:

$$\phi_{1,2} = \underset{\phi_{1,2}}{\arg\min} \Big[t(\phi_{1,2}) \Big]. \tag{8.7}$$

8.2.2 Transmission through interfaces

In a pulse-echo measurement of a point in layer 2, the ultrasonic wave passes twice through the interface between layer 1 and 2. Due to the difference in acoustic impedance, only part of the wave is transmitted from one layer to the next. In general, the transmission factor between the layers is a function of both the layer impedances and the angles α_1 and α_2, with large angles yielding low transmission factors [Brekhovskikh and Godin, 1990].

However, most ultrasonic transducers have relatively narrow beams, and thus the transmission factor is approximately uniform within the beam. Ignoring the angle dependence, the transmission through the interface effectively scales all backscattered echoes from the second layer with a constant factor. In the simulations described here, we are mainly interested in the relative amplitudes within each layer, and the scaling effect of the interface is therefore not included.

8.2.3 Transducer directivity

It is assumed that the transducer is circular and uniformly excited, and as discussed in Section 2.4.3, this yields the pulse-echo directivity function

$$D_{C,PE}(\omega, \gamma) = \mathrm{jinc}^2 \left(\frac{\omega D \sin\gamma}{2c_1} \right), \tag{8.8}$$

where γ is the angle between the transducer normal and the propagation direction in layer 1. The relationship between γ and $\phi_{1,2}$ is given by the law of sines:

$$\gamma = \sin^{-1} \left(\frac{R_2}{r_1'} \cdot \sin(\phi_{1,2} - \phi') \right). \tag{8.9}$$

8.2.4 Complete model

The signal received from the point scatterer is modelled as

$$s(t,\phi') = \frac{1}{(r_1' + r_2')^2} \cdot \mathcal{F}_t^{-1}\left\{S_0(\omega) \cdot e^{i\omega \cdot 2t} \cdot D_{C,PE}(\omega,\gamma)\right\} \tag{8.10}$$

where $S_0(\omega)$ denotes the Fourier transform of the original pulse transmitted by the transducer. The factor $\frac{1}{(r_1'+r_2')^2}$ accounts for the two-way geometrical spreading in each layer. The pulse is delayed by a phase shift of $\omega \cdot 2t$, where t is given by (8.6), and scaled by the pulse-echo transducer directivity $D_{C,PE}(\omega,\gamma)$.

8.3 Simulation results

A transducer model with 2.5 mm diameter and 2.25 MHz center frequency was used, emitting a Gaussian modulated sinusoidal pulse with 60 % relative bandwidth. The simulated geometry consisted of water and steel layers, with wave velocities set to 1500 and 5500 m/s and densities set to 1000 and 7700 kg/m^3, respectively. The transducer was scanned at $R_1 = 100$ mm, and the interface between the layers was placed at $R_2 = 200$ mm. Three point scatterers were placed in the water layer, and five were placed in the steel layer, all evenly spaced within the range interval $r \in [175{,}245]$ mm. The raw data of the simulated scan is plotted in Fig. 8.4(a), with a dashed line indicating the interface between the two layers. Note that because the wave velocity is higher in steel than in water, the scatterer responses appear closer to each other in the steel layer.

To illustrate the difference between the single- and multilayer CPSM algorithm, the raw data was processed with both algorithms, and the results are shown in Figs. 8.4(b) and 8.4(c). For the single-layer algorithm, the wave velocity of water, 1500 m/s, was used for the entire image. Fig. 8.4(b) shows that this yields a focused image of the scatterers in the water layer, while the scatterers in the steel layer become increasingly unfocused as the range increases. However, when the multilayer algorithm is applied, the scatterers are focused equally well in both layers, as seen in Fig. 8.4(c). Note that since the wavelength is longer in the steel layer compared to the water layer, the scatterers appear larger in the range direction in the steel layer.

The -6 dB width of the point scatterers in both images were measured, and the results are shown in Fig. 8.5. The plot clearly shows how the multilayer processing yields an approximately constant angular resolution, while the resolution in the single-layer processing decreases in the steel layer. However, close to the interface the single-layer processing still yields a high resolution.

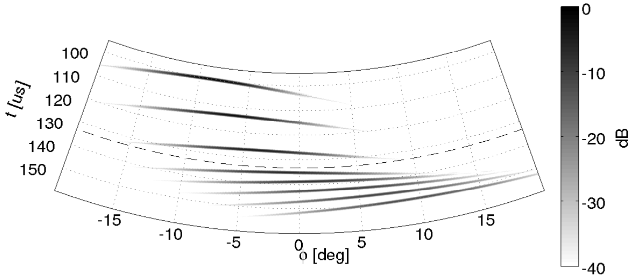

(a) Raw data

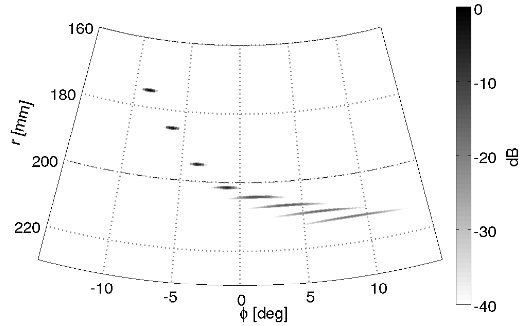

(b) Image focused with single-layer CPSM, assuming water in the entire imaged region

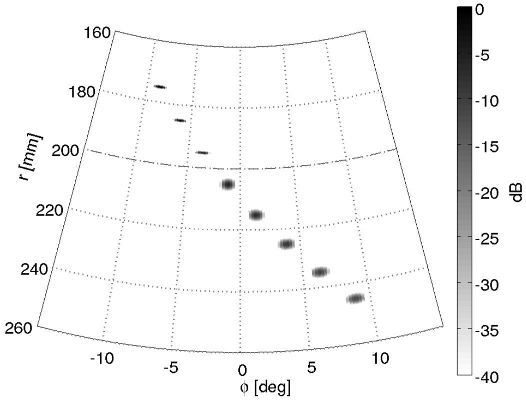

(c) Image focused with multilayer CPSM

Figure 8.4: Raw data and focused images from a simulation with scatterers in water and steel layers. The interface between the layers, located at $R_2 = 200$ mm, is indicated with a dashed line.

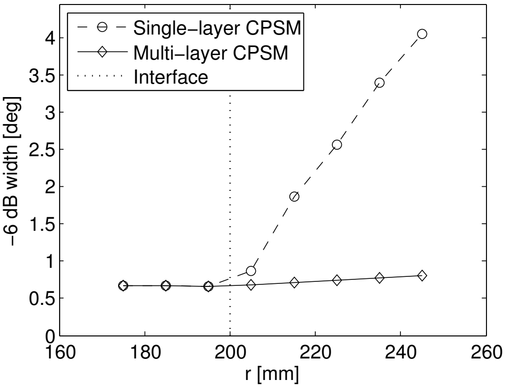

Figure 8.5: -6 dB width of focused point responses in simulated experiment with point-like scatterers in concentric water and steel layers.

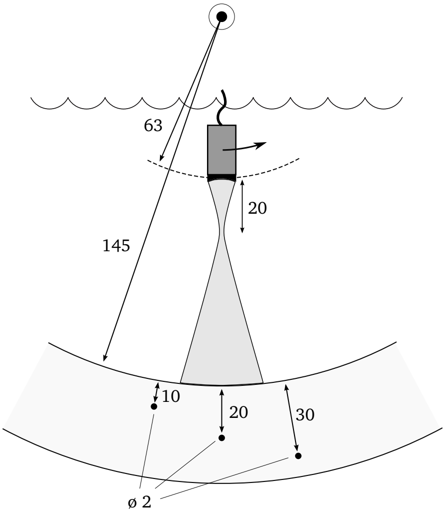

Figure 8.6: Experimental setup for scan of plastic pipe with three side-drilled holes.

8.4 Point scatterer experiment

An experiment was performed to test the multilayer CPSM algorithm on real data. The experimental setup is shown in Fig. 8.6. A 2.25 MHz focused transducer with 12.7 mm diameter and 20 mm focal length was used, scanned at a radius of 63 mm. The focal point of the transducer was treated as a virtual source, as described in Chapter 7. Three holes of 2 mm diameter were drilled into the side of a plastic pipe with 145 mm inner diameter, and the transducer was scanned perpendicularly to the holes.

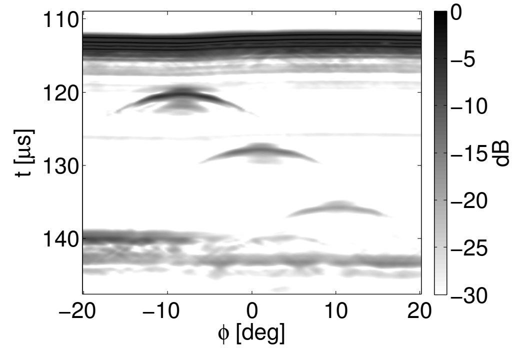

(a) Raw data

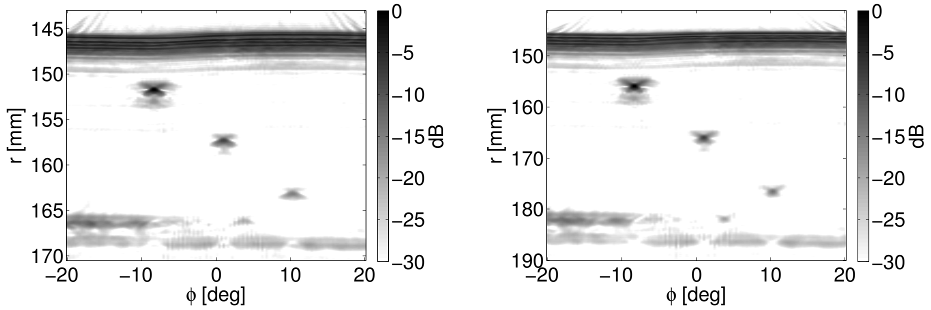

(b) Focused image, single-layer CPSM

(c) Focused image, multi-layer CPSM

Figure 8.7: Raw data and focused images from experiment with side-drilled holes in plastic pipe.

The raw data from the scan was processed with both the single- and multilayer CPSM algorithm, assuming wave velocities in water and plastic of 1480 and 2450 m/s, respectively. The results are shown in Fig. 8.7.

The responses from the scatterers are similar to those seen in the virtual source experiment in Section 7.2.2, in that there are artifacts surrounding the main focused point, making the response similar to an “X”. The two focused images are quite similar, but the image produced by single-layer processing shows some signs of defocusing as the range increases. This effect is seen more clearly in Fig. 8.7, in which the detailed point spread functions for each scatterer are shown. Note that for the deepest scatterer, the -6 dB width for the single-layer processing is approximately double that of the multilayer processing.

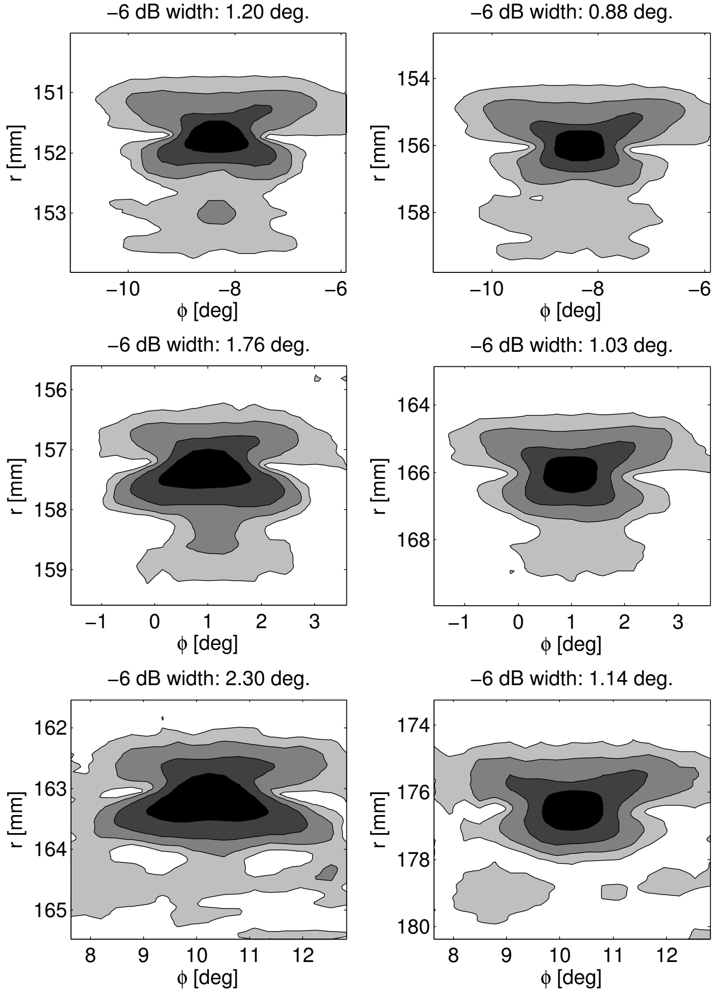

Figure 8.8: Point spread functions from single- and multilayer processing of scan of plastic pipe with side-drilled holes. Left column: Single-layer processing. Right column: Two-layer processing. Rows, top to bottom: Scatterers, ordered by increasing range. The interval between each contour value is 6 dB.

8.5 Discussion

In the derivation of the multilayer CPSM algorithm we assumed that the layers are all concentric, and that the measurement surface is perfectly centered relative to the layers. However, in practical pipe inspection, the measurement surface can become de-centered, as discussed in the introduction to Chapter 7. This problem can possibly be alleviated by extrapolating the wave field to a virtual measurement surface which is centered in the pipe, using (6.6). Such preprocessing is would be similar to the tilt compensation method described in Appendix 4.B.

The simulation and the experiment presented in Section 8.3 and 8.4 both demonstrated that with single-layer processing, the lateral resolution in the second layer decreases with increasing range, while the multilayer algorithm maintains a high resolution. However, for small depths inside the second layer, the difference between the two is relatively small. Also, the difference in resolution between single- and multilayer processing was smaller in the experiment than in the simulation. This is probably because the difference in wave velocity between the two layers was also smaller in the experiment. These results suggest that for thin pipe walls or structures with wave velocities close to that of water, single-layer processing may in some cases be sufficient. Single-layer processing also would not require compensation of measurement surface de-centering, as discussed above.

8.6 Summary

In this chapter, we have extended the CPSM algorithm to the case of multiple concentric layers, enabling pipeline inspection with full volumetric imaging. A simulation model for circular scans of two-layered geometries was presented, and the single-layer and multilayer CPSM algorithms were compared for both simulated and experimental scans of two-layered geometries. The results demonstrated that the images produced by the single-layer CPSM algorithm become defocused in the second layer, while the multilayer algorithm maintains a high lateral resolution in both layers. However, single-layer processing may be sufficient for inspection of pipes with thin walls.

Chapter 9

Conclusions

In this thesis, we have described several algorithms for synthetic aperture ultrasound imaging of multilayered media and cylindrical structures. The development of these algorithms was motivated by the need for accurate methods for non-destructive testing of pipelines, in particular water distribution pipelines.

We have formulated algorithms for two-dimensional imaging in horizontally layered media, in both the time domain and the Fourier domain. For time-domain algorithms, determination of focusing delays is complicated due to the refraction of waves at interfaces. We have shown that an approximate expression for these delays can be derived based on the root-mean-square wave velocity in the layered media, and have used this approximation to develop an algorithm termed Multi-Layer Delay-And-Sum (MLDAS). We have also described two Fourier-domain algorithms for multilayer imaging, called Phase Shift Migration (PSM) and Multi-Layer Omega-K (MULOK). Both algorithms are based on the concept of wave field extrapolation, which implicitly takes the effect of refraction into account. The PSM algorithm performs focusing by iteratively extrapolating the wave field into the imaged region, and it can therefore handle arbitrary variations in wave velocity. However, within each layer the wave field can be focused efficiently through Stolt migration, performed as a resampling of the Fourier-domain wave field. The MULOK algorithm exploits this, and combines PSM and Stolt migration into an efficient algorithm for multilayer imaging.

By applying the multilayer algorithms to simulated data sets, we have shown that the processing times of the Fourier-domain algorithms are generally lower than those of the MLDAS algorithm, in many cases orders of magnitude lower. However, the processing time of the PSM algorithm grows quickly as the depth range of the ultrasonic image increases, and the MULOK processing time is substantially lower for large-range data sets.

In raw ultrasonic data, the lateral resolution decreases as the distance from the transducer increases, due to the divergence of the ultrasonic beam. However, by applying synthetic aperture focusing in post-processing the lateral resolution can be increased significantly. For ultrasonic scans performed along a line or over a flat plane, the lateral resolution after focusing is approximately half the transducer diameter, independent of the distance to the transducer. In this thesis, we have shown that this resolution limit is also valid in the multilayer case, provided that the transducer beam is relatively narrow. For wide beams, transmission of the beam through multiple layers may be limited by the critical angles of the layer interfaces, resulting in decreased resolution.

In most descriptions of synthetic aperture algorithms in the ultrasound literature, it is assumed that the measurements are performed along a straight line or over a flat plane. However, when inspecting pipelines or other cylindrical structures from the inside, a cylindrical measurement surface is better suited. In this thesis, we have derived a new Fourier-domain synthetic aperture algorithm for cylindrical scans, termed Cylindrical Phase Shift Migration (CPSM). The algorithm is based directly on the solutions to the scalar wave equation in cylindrical coordinates, and in this sense the algorithm is exact. We have compared the algorithm to a similar, previously published algorithm, and shown that CPSM is superior for scans performed with wide-beam transducers.

We have studied the lateral resolution achieved by the CPSM algorithm both theoretically and experimentally. The lateral resolution along the axis of the cylindrical measurement surface is approximately equal to half the transducer diameter in the entire focused image, as for a linear scan. However, the angular resolution was shown to be equal to $D/(2R)$, where R denotes the radius of the measurement surface. This yields a spatial resolution along the angular axis which decreases with the distance from the transducer. At large distances, there is a significant difference in resolution between the two lateral axes.

We have also shown that the CPSM algorithm can be applied to scans performed with focused transducers, by treating the focal point of the transducer as a small virtual source. In an experiment with a severely corroded pipe, we compared the estimated topography for two cases; one scan where the pipe wall was in the transducer focal zone, and another where the transducer was several focal lengths away from the pipe, focused with CPSM in post-processing. The results showed that the quality of the topography estimate was approximately the same in both cases. This demonstrates that CPSM can be used to significantly extend the range of focused transducers in pipe inspection applications.

Finally, we have shown that the CPSM algorithm can be extended for synthetic aperture focusing in multiple concentric layers. This combination of multilayer focusing and focusing in cylindrical coordinates enables high-resolution volumetric imaging in pipelines and similar structures. In practice, this can improve the ability of ultrasonic pipe inspection systems to detect and size defects, for example outside corrosion damage. Note, however, that the algorithm is based on the assumption that the layer interfaces are smooth and concentric, and that focusing performance will be lower in pipes with irregular interfaces. We have also shown, through an experiment with artificial pitting corrosion, that accurate determination of pitting shapes is difficult due to specular reflections at oblique surfaces. The practical applicability of the algorithm can only be determined through large-scale implementation and testing in real pipelines.

9.1 Thesis contributions

The novel contributions in this thesis to the research area of non-destructive testing using synthetic aperture ultrasound are, in order of appearance:

- The application of RMS velocity for time-domain synthetic aperture ultrasound imaging in multilayered media, first presented in [Skjelvareid and Birkelund, 2010] and described here in Section 4.1.
- The combination of the phase shift migration and Stolt migration algorithms for efficient Fourier-domain synthetic aperture imaging in multilayered media, first presented in [Skjelvareid et al., 2011c], and described here in Section 4.2.1.
- The derivation of a Fourier-domain remapping method for tilt compensation in multilayer scans, first presented in [Olofsson et al., 2010] and described in Section 4.B.
- The introduction of an exact algorithm for Fourier-domain synthetic aperture imaging using cylindrical apertures, first presented in [Skjelvareid et al., 2012b] and described in Section 6.1.
- The derivation of a simple expression for the achievable lateral resolution in synthetic aperture imaging using cylindrical apertures, first presented in [Skjelvareid et al., 2012b], and described in Section 6.1.4.
- Providing new insights into the practical use of synthetic aperture ultrasound, for non-destructive testing in general and pipeline inspection in particular. The experiments first presented in [Skjelvareid et al., 2011a] and [Skjelvareid et al., 2012a] and described in Chapter 5 and 7 demonstrate some of the possibilities and limitations of three-dimensional synthetic aperture ultrasound.
- Expansion of synthetic aperture imaging using cylindrical apertures to the case of multilayered media, presented here in Chapter 8.

9.2 Suggested future work

Although synthetic aperture ultrasound has been actively researched for decades, there are still a large number of possibilities to be investigated. It is also, as we have seen examples of in this thesis, much to be gained from research conducted in the fields of seismic exploration and synthetic aperture radar and sonar. Here we list some suggestions for future research which extend the work in this thesis:

- The imaging systems treated in this thesis have been limited to monostatic systems. However, use of transducer arrays has become the standard in medical ultrasound imaging, and are also coming into use for non-destructive testing [Drinkwater and Wilcox, 2006]. The use of arrays simplifies the ultrasonic scanning process by removing the need to mechanically move the transducer, which can be a great advantage in demanding environments like pipelines. Arrays also enable imaging schemes involving multiple transmitters and receivers, which can yield a higher signal-to-noise ratio than monostatic systems [Chiao and Thomas, 1994; Holmes et al., 2005]. Adapting the algorithms presented in this thesis to a general array imaging framework could both improve their performance and widen their area of application.

- The multilayer algorithms presented in Chapter 4 require that the layers are horizontal, or, with the addition of the tilt compensation described in 4.B, that they are planar. Similarly, the algorithm described in 8 requires that the layers are concentric. In practice, however, the interfaces between different layers may be irregular, and to make multilayer synthetic aperture imaging more generally applicable, it should be extended to two- or three-dimensional wave velocity models. This topic has been researched extensively in the field of seismic exploration, [Gazdag and Sguazzero, 1984; Stoffa et al., 1990; Margrave and Ferguson, 1999; Margrave, 2003], and some of the suggested solutions may also be applicable to ultrasound imaging.

- In this thesis, we have included only longitudinal waves in the theoretical treatment of wave fields. However, solid media can also propagate shear waves, as discussed in Section 2.3. Extending the multilayer algorithms to include shear waves would therefore make them more generally applicable to solid media.

- The experiments performed in this thesis have given several insights into the possibilities and limitations of synthetic aperture ultrasound, especially with application to multilayered media and pipe geometries. However, ultimately the experiments are limited in their range of transducer parameters, the imaging geometry applied, and the types of defects tested. Further experiments and large-scale testing could give a more thorough understanding of when synthetic aperture focusing should be applied.

Bibliography

Andresen, H., Nikolov, S. I., and Jensen, J. A. (2011). Synthetic aperture focusing for a single-element transducer undergoing helical motion. *IEEE Trans. Ultrason., Ferroelectr., Freq. Control*, *58*, 935–943.

ASNT (2007). *Nondestructive Testing Handbook - Volume 7: Ultrasonic Testing*, vol. 7. American Society for Nondestructive Testing, third ed.

Beuker, T., Palmer, J., and Quack, M. (2009). In-line inspection using combined technologies – magnetic flux leakage and ultrasonic testing and their advantages. In *4th Pipeline Technology Conference*.
`http://www.pipeline-conference.com/abstracts/line-inspection-using-combined-technologies-magnetic-flux-leakage-and-ultrasonic-testing`

Birchall, M., Sevciuc, N., and Madureira, C. (2007). Internal ultrasonic pipe and tube inspection - IRIS. In *IV Conferencia Panamericana de END*.
`http://www.ndt.net/article/panndt2007/papers/149.pdf`

Bouget, J.-Y. (2010). Camera calibration toolbox for Matlab.
`http://www.vision.caltech.edu/bouguetj/calib_doc/`

Brekhovskikh, L., and Godin, O. (1990). *Acoustics of Layered Media I: Plane and Quasi-Plane Waves*. Springer Series on Wave Phenomena. Springer-Verlag.

Burch, S. F., and Burton, J. T. (1984). Ultrasonic synthetic aperture focusing using planar pulse-echo transducers. *Ultrasonics*, *22*(6), 270–274.

Busse, L. J. (1992). Three-dimensional imaging using a frequency-domain synthetic aperture focusing technique. In *IEEE Trans. Ultrason., Ferroelectr., Freq. Control*, vol. 39.

Cafforio, C., Prati, C., and Rocca, E. (1991). SAR data focusing using seismic migration techniques. *IEEE Transactions on Aerospace and Electronic Systems*, *27*, 194–207.

Callow, H. J. (2003). *Signal Processing for Synthetic Aperture Sonar Image Enhancement*. Ph.D. thesis, University of Canterbury, Christchurch, New Zealand.

Carvalho, A., Rebello, J., Souza, M., Sagrilo, L., and Soares, S. (2008). Reliability of non-destructive test techniques in the inspection of pipelines used in the oil industry. *International Journal of Pressure Vessels and Piping*, *85*(11), 1–7.

Chiao, R. Y., and Thomas, L. J. (1994). Analytic evaluation of sampled aperture ultrasonic imaging techniques for NDE. *IEEE Trans. Ultrason., Ferroelectr., Freq. Control*, *41*(4), 484–493.

Claerbout, J. F. (1985). *Imaging the Earth's Interior*. Blackwell Scientific Publications.
`http://sepwww.stanford.edu/data/media/public/sep/prof/iei2/`

Claerbout, J. F. (2010). *Basic Earth Imaging*. Stanford University.
`http://sepwww.stanford.edu/sep/prof/bei11.2010.pdf`

Corke, P. (2011a). Machine vision toolbox for Matlab.
`http://www.petercorke.com/Machine_Vision_Toolbox.html`

Corke, P. (2011b). *Robotics, Vision and Control - Fundamental Algorithms in Matlab*. Springer-Verlag Berlin / Heidelberg.

Cumming, I. G., and Wong, F. H. (2004). *Digital Signal Processing of Synthetic Aperture Radar Data: Algorithms and Implementation*. Artech House.

Demma, A., Alleyne, D., and Pavlakovic, B. (2005). Testing of buried pipelines using guided waves. In *3rd Middle East Nondestructive Testing Conference & Exhibition*.
`http://www.ndt.net/article/mendt2005/pdf/33.pdf`

Djelouah, H., Baboux, J., and Perdrix, M. (1991). Theoretical and experimental study of the field radiated by ultrasonic focussed transducers. *Ultrasonics*, *29*(3), 188 – 200.

Doctor, S., Hall, T., and Reid, L. (1986). SAFT - the evolution of a signal processing technology for ultrasonic testing. *NDT International*, *19*(3), 163–167.

Doctor, S., Schuster, G., Reid, L., and Hall, T. (1996). Real-Time 3D SAFT-UT System Evaluation and Validation, NUREG/CR-6344 PNNL-10571. Tech. rep., Pacific Northwest National Laboratory.

Drinkwater, B. W., and Wilcox, P. D. (2006). Ultrasonic arrays for non-destructive evaluation: A review. *NDT&E International*, *39*(7), 525–541.

Duran, O., Althoefer, K., and Seneviratne, L. (2002). State of the art in sensor technologies for sewer inspection. *Sensors Journal, IEEE*, *2*(2), 73 –81.

EEA (2009). Water resources across europe — confronting water scarcity and drought. (2).
`http://www.eea.europa.eu/publications/water-resources-across-europe/at_download/file`

Eiswirth, M., Heske, C., Hotzl, H., Schneider, T., and Burn, L. S. (2000). Pipe defect characterisation by multi-sensor systems. In *Proc. 18th Int. Conf. No-Dig, Perth, Australia*.

Ensminger, D., and Bond, L. J. (2012). *Ultrasonics: Fundamentals, Technologies, and Applications*. CRC Press.

Fink, M. (1997). Time reversed acoustics. *Physics Today*, (pp. 34–40).

Fleury, G., Froelich, B., Guey, J.-L., Liang, K., and Schoeb, P. (2006). Cylindrical ultrasonic array for borehole applications. In *IEEE 2006 Ultrasonics Symposium. Proceedings.*, (pp. 38 –41).

Frazier, C. H., and O'Brien Jr., W. D. (1998). Synthetic aperture techniques with a virtual source element. *IEEE Trans. Ultrason., Ferroelectr., Freq. Control*, *45*(1), 196–207.

Fuchs, H. V., and Reihle, R. (1991). Ten years of experience with leak detection by acoustic signal analysis. *Applied Acoustics*, *33*, 1–19.

Gammell, P. (1981). Improved ultrasonic detection using the analytic signal magnitude. *Ultrasonics*, *19*(2), 73–76.

Gardner, J., and Collin, R. E. (2000). An accurate closed-form approximate representation for the Hankel function of the second kind. *IEEE Trans. Antennas Propag.*, *48*(10), 1699–1700.

Gazdag, J. (1978). Wave equation migration with the phase-shift method. *Geophysics*, *43*(7), 1342–1351.

Gazdag, J., and Sguazzero, P. (1984). Migration of seismic data by phase shift plus interpolation. *Geophysics*, *49*(2), 124–131.

Goodman, J. W. (1996). *Introduction to Fourier Optics*. McGraw-Hill, second ed.

Gough, P. T., and Hawkins, D. W. (1997). Imaging algorithms for a strip-map synthetic aperture sonar: Minimizing the effects of aperture errors and aperture undersampling. *IEEE Journal of Oceanic Engineering*, *22*(1), 27–39.

Gough, P. T., and Hawkins, D. W. (1998). Unified framework for modern synthetic aperture imaging algorithms. *International journal of imaging systems and technology*, *8*(4), 343–358.

Gu, K., Wang, J., and Li, J. (2004). Migration based sar imaging for ground penetrating radar systems. In *IEE Proceedings - Radar, Sonar and Navigation*, vol. 151.

Hansen, R. E. (2011). *Sonar systems*, chap. Introduction to Synthetic Aperture Sonar, (pp. 3–28). InTech.
`http://www.intechopen.com/books/sonar-systems/introduction-to-synthetic-aperture-sonar`

Haun, M. A., Jones, D. L., and Jr., W. D. O. (2002). Efficient three-dimensional imaging from a small cylindrical aperture. *IEEE Trans. Ultrason., Ferroelectr., Freq. Control*, *49*(7), 861–870.

Hayes, M. P., and Gough, P. (2004). Synthetic aperture sonar: A maturing discipline. In *Proceedings of the Seventh European Conference on Underwater Acoustics*.

Hayes, M. P., and Gough, P. T. (1992). Broad-band synthetic aperture sonar. *IEEE Journal of Oceanic Engineering*, *17*(1), 80–94.

Hayman, A., Parent, P., Cheung, P., and Verges, P. (1998). Improved borehole imaging by ultrasonics. *SPE Production & Facilities*, *13*(1), 5–13.

Holmes, C., Drinkwater, B. W., and Wilcox, P. D. (2005). Post-processing of the full matrix of ultrasonic transmit-receive array data for non-destructive evaluation. *NDT&E International*, *38*(8), 701–711.

Hunaidi, O. (2012). Acoustic leak detection survey strategies for water distribution pipes. *Construction Technology Update*, *79*, 1–5.

Hunter, A. J., Drinkwater, B. W., and Wilcox, P. D. (2008). The wavenumber algorithm for full-matrix imaging using an ultrasonic array. *IEEE Trans. Ultrason., Ferroelectr., Freq. Control*, *55*(11), 2450–2462.

Jensen, J. A., Nikolov, S. I., Gammelmark, K. L., and Pedersen, M. H. (2006). Synthetic aperture ultrasound imaging. *Ultrasonics*, *44*, e5–e15.

Johnson, J., and Barna, B. (1983). The effects of surface mapping corrections with synthetic-aperture focusing techniques on ultrasonic imaging. *IEEE Transactions on Sonics and Ultrasonics*, *30*(5), 283–294.

Karaman, M., Li, P.-C., and O'Donnell, M. (1995). Synthetic aperture imaging for small scale systems. *IEEE Trans. Ultrason., Ferroelectr., Freq. Control*, *42*(3), 429–442.

Kim, Y. C., Gonzalez, R., and Berryhill, J. R. (1989). Recursive wavenumber-frequency migration. *Geophysics*, *54*(3), 319–329.

Kino, G., Corl, D., Bennett, S., and Peterson, K. (1980). Real time synthetic aperture imaging system. In *1980 Ultrasonics Symposium. Proceedings.*, (pp. 722 – 731).

Kinsler, L. E., Frey, A. R., Coppers, A. B., and Sanders, J. V. (1999). *Fundamentals of Acoustics*. John Wiley and Sons, Inc., fourth ed.

Kloosterman, E. (2009). Condition assessment of metallic water mains by internal pipe inspection. In *4th Pipeline Technology Conference*. `http://www.pipeline-conference.com/abstracts/condition-assessment-metallic-water-mains-internal-pipe-inspection`

Koutsakos, E., Woodward, T., and Russell, D. E. (1997). Using a non-destructive technique for evaluating water mains conditions. In *BHR group conference series: 3rd International Conference on Water Pipeline Systems*, 93 - 105.

Kraus, H. (1983). Generalized synthetic aperture, focused transducer, pulse-echo, ultrasonic scan data processing for non-destructive inspection. *Ultrasonics*, *21*(1), 11 – 18.

Kriesz, H. (1979). Radiographic NDT - a review. *NDT International*, *12*(6), 270–273.

Lanari, R. (1995). A new method for the compensation of the SAR range cell migration based on the chirp z-transform. *IEEE Transactions on Geoscience and Remote Sensing*, *33*(5), 1296–1299.

Langenberg, K., Berger, M., Kreutter, T., Mayer, K., and Schmitz, V. (1986). Synthetic aperture focusing technique signal processing. *NDT International*, *19*(3), 177–189.

Levanda, R., and Leshem, A. (2010). Synthetic aperture radio telescopes. *IEEE Signal Processing Magazine*, (pp. 14–29).

Lingvall, F., and Olofsson, T. (2007). On time-domain model-based ultrasonic array imaging. *IEEE Trans. Ultrason., Ferroelectr., Freq. Control*, *54*(8), 1623–1633.

Lingvall, F., Olofsson, T., and Stepinski, T. (2003). Synthetic aperture imaging using sources with finite aperture: Deconvolution of the spatial impulse response. *Journal of the Acoustical Society of America*, *114*(1), 225–234.

Lohr, K. R., Rose, J. L., Lohr, K. R., and Rose, J. L. (2003). Ultrasonic guided wave and acoustic impact methods for pipe fouling detection. *Journal of Food Engineering*, *56*(4), 315 – 324.

Lopez-Sanchez, A. L., Kim, H.-J., Schmerr Jr., L. W., and Sedov, A. (2005). Measurement models and scattering models for predicting the ultrasonic pulse-echo response from side-drilled holes. *Journal of Nondestructive Evaluation*, *24*(3), 83–96.

Lowe, M., Alleyne, D., and Cawley, P. (1998). Defect detection in pipes using guided waves. *Ultrasonics*, *36*, 147–154.

Margrave, G. F., and Ferguson, R. J. (1999). Wavefield extrapolation by nonstationary phase shift. *Geophysics*, *64*(4), 1067–1078.

Margrave, G. M. (2003). *Numerical Methods in Exploration Seismology - with algorithms in Matlab*. University of Calgary.
`http://www.crewes.org/ResearchLinks/FreeSoftware/NumMeth.pdf`

Martinez, O., Parrilla, M., Izquierdo, M. A. G., and Ullate, L. G. (1999). Application of digital signal processing techniques to synthetic aperture focusing technique images. *Sensors and Actuators*, *76*, 448–456.

Mayer, K., Marklein, R., Langenberg, K., and Kreutter, T. (1990). Three-dimensional imaging system based on Fourier transform synthetic aperture focusing technique. *Ultrasonics*, *28*, 241–255.

McNoleg, O. (1996). The integration of GIS, remote sensing, expert systems and adaptive co-kriging for environmental habitat modeling of the highland haggis using object-oriented, fuzzy-logic and neural-network techniques. *Computers & Geosciences*, *22*(5), 585–588.

Misaridis, T., and Jensen, J. (2005). Use of modulated excitation signals in medical ultrasound. Part I: Basic concepts and expected benefits. *IEEE Trans. Ultrason., Ferroelectr., Freq. Control*, *52*(2), 177 –191.

Müller, W., Kreutter, T., Thumser, D., and Schmitz, V. (1991). Ultrasonic turbine shaft inspection using the synthetic aperture focussing technique (SAFT). *Nuclear Engineering and Design*, *130*(1), 339–346.

Nagai, K. (1985). A new synthetic-aperture focusing method for ultrasonic B-scan imaging by the Fourier transform. *IEEE Trans. Sonics Ultrason.*, *SU-32*, 531–536.

Norwegian Research Council (2012). The Industrial Ph.D. Scheme. Accessed June 30. 2012.
`http://www.forskningsradet.no/naeringsphd`

O'Donnell, M., Eberle, M., Stephens, D., Litzza, J., San Vicente, K., and Shapo, B. (1997). Synthetic phased arrays for intraluminal imaging of coronary arteries. *IEEE Trans. Ultrason., Ferroelectr., Freq. Control*, *44*(3), 714 –721.

O'Donnell, M., and Thomas, L. (1992). Efficient synthetic aperture imaging from a circular aperture with possible application to catheter-based imaging. *IEEE Trans. Ultrason., Ferroelectr., Freq. Control*, *39*(3), 366 –380.

Okamoto Jr., J., Adamowski, J. C., Tsuzuki, M. S., Buiochi, F., and Camerini, C. S. (1999). Autonomous system for oil pipelines inspection. *Mechatronics*, *9*, 731–743.

Olofsson, T. (2010). Phase shift migration for imaging layered objects and objects immersed in water. *IEEE Trans. Ultrason., Ferroelectr., Freq. Control*, *57*(11), 2522–2530.

Olofsson, T., Skjelvareid, M. H., and Barkefors, A. (2010). Ultrasonic imaging of immersed objects using migration techniques. In *European Conference on Synthetic Aperture Radar (EUSAR)*, (pp. 442–445).

Olympus Corp. (2012). Ultrasonic transducers technical notes. `http://www.olympus-ims.com/en/.downloads/download/?file=285213010&fl=en_US`

O'Neil, H. T. (1949). Theory of focusing radiators. *Journal of the Acoustical Society of America*, *21*(5), 516–526.

Passmann, C., and Ermert, H. (1996). A 100-MHz ultrasound imaging system for dermatologic and ophthalmologic diagnostics. *IEEE Trans. Ultrason., Ferroelectr., Freq. Control*, *43*(4), 545 –552.

Pörtzgen, N., Gisolf, D., and Blacquière, G. (2007). Inverse wave field extrapolation: A different NDI approach to imaging defects. *IEEE Trans. Ultrason., Ferroelectr., Freq. Control*, *54*(1), 118–127.

Raj, B., Jayakumar, T., and Thavasimuthu, M. (2002). *Practical Non-Destructive Testing*. Woodhead Publishing Ltd.

Rajani, B., and Kleiner, Y. (2004). Non-destructive inspection techniques to determine structural distress indicators in water mains. In *Evaluation and Control of Water Loss in Urban Water Networks*, (pp. 1–20). Valencia, Spain.

Ratcliffe, J. A. (1956). Some aspects on diffraction theory and their application to the ionosphere. *Reports on Progress in Physics*, *19*, 188–267.

Reber, K., Beller, M., Willems, H., and Barbian, O. A. (2002). A new generation of ultrasonic in-line inspection tools for detecting, sizing and locating metal loss and cracks in transmission pipelines. In *2002 IEEE Ultrasonics Symposium. Proceedings.*, vol. 1, (pp. 665 – 671).

Roman, H. T., and Pellegrino, B. A. (1993). Pipe crawling inspection robots: An overview. *IEEE Transactions on Energy Conversion*, *8*(3), 576–583.

Schmerr, L. W., and Song, S.-J. (2007). *Ultrasonic Nondestructive Evaluation Systems: Models and Measurements*. Springer.

Schneider, W. A. (1984). The common depth point stack. *Proceedings of the IEEE*, *72*(10), 1238–1254.

Schultz, P. S. (1984). Seismic velocity estimation. *Proceedings of the IEEE*, *72*(10), 1330–1339.

Shlivinski, A., and Langenberg, K. (2007). Defect imaging with elastic waves in inhomogeneous–anisotropic materials with composite geometries. *Ultrasonics*, *46*(1), 89 – 104.

Skjelvareid, M. H., and Birkelund, Y. (2010). Ultrasound imaging using multilayer synthetic aperture focusing. In *ASME 2010 Pressure Vessels and Piping Conference*, vol. 5, (pp. 379–387).

Skjelvareid, M. H., Birkelund, Y., and Larsen, Y. (2012a). Internal pipeline inspection using virtual source synthetic aperture ultrasound imaging. Submitted to *NDT&E International* May 2012, currently in review.

Skjelvareid, M. H., Birkelund, Y., and Larsen, Y. (2012b). Synthetic aperture focusing of outwardly directed cylindrical ultrasound scans. Submitted to *IEEE Trans. Ultrason., Ferroelectr., Freq. Control* January 2012, accepted for publication July 2012.

Skjelvareid, M. H., Birkelund, Y., Olofsson, T., and Larsen, Y. (2011a). Ultrasonic imaging of pitting using multilayer synthetic aperture focusing. In *2011 IEEE Ultrasonics Symposium. Proceedings.*, (pp. 2042–2024).

Skjelvareid, M. H., Olofsson, T., and Birkelund, Y. (2011b). Three-dimensional ultrasonic imaging in multilayered media. In *International Congress on Ultrasonics 2011, AIP Conference Proceedings*, vol. 1433, (pp. 169–172).

Skjelvareid, M. H., Olofsson, T., Birkelund, Y., and Larsen, Y. (2011c). Synthetic aperture focusing of ultrasonic data from multilayered media using an omega-k algorithm. *IEEE Trans. Ultrason., Ferroelectr., Freq. Control*, *58*(5), 1037–1048.

Statistics Norway (2010). Kostra: Municipal water supply. Accessed May 20. 2012.
`http://www.ssb.no/english/subjects/01/04/20/vann_kostra_en/`

Stepinski, T. (2007). An implementation of synthetic aperture focusing technique in frequency domain. *IEEE Trans. Ultrason., Ferroelectr., Freq. Control*, *54*(7), 1399–1408.

Stoffa, P. L., Fokkema, J. T., de Luna Freire, R. M., and Kessinger, W. P. (1990). Split-step Fourier migration. *Geophysics*, *55*(4), 410–421.

Stolt, R. H. (1978). Migration by Fourier transform. *Geophysics*, *43*(1), 23–48.

Tomiyasu, K. (1978). Tutorial review of synthetic-aperture radar (SAR) with applications to imaging of the ocean surface. *Proceedings of the IEEE*, *66*(5), 563–583.

Ulander, L. M. H., Hellsten, H., and Stenström, G. (2003). Synthetic-aperture radar processing using fast factorized back-projection. *IEEE Trans. Aerosp. Electron. Syst.*, *39*(3), 760–776.

Velichko, A., and Wilcox, P. D. (2010). An analytical comparison of ultrasonic array imaging algorithms. *Journal of the Acoustical Society of America*, *127*(4), 2377–2384.

Vray, D., Haas, C., Rastello, T., Krueger, M., Brusseau, E., Schroeder, K., Gimenez, G., and Ermert, H. (2001). Synthetic aperture-based beam compression for intravascular ultrasound imaging. *IEEE Trans. Ultrason., Ferroelectr., Freq. Control*, *48*(1), 189 –201.

Wennerström, E., and Stepinski, T. (2007). Model-based correction of diffraction effects of the virtual source element. *IEEE Trans. Ultrason., Ferroelectr., Freq. Control*, *54*(8), 1614 –1622.

Williams, E. G. (1999). *Fourier Acoustics: Sound Radiation and Nearfield Acoustical Holography*. Academic Press.

Wood, L. C., and Treitel, S. (1975). Seismic signal processing. *Proceedings of the IEEE*, *63*(4), 649–661.

Ylitalo, J. T., and Ermert, H. (1994). Ultrasound synthetic aperture imaging: Monostatic approach. *IEEE Trans. Ultrason., Ferroelectr., Freq. Control*, *41*(3), 333 –339.

ISBN 978-82-8236-066-1